Technische Universität München
TUM School of Natural Sciences

Integrated modeling of energetic particle-driven Alfvén eigenmodes in Tokamak fusion plasmas

Virgil - Alin Popa

Vollständiger Abdruck der von der TUM School of Natural Sciences der Technischen Universität München zur Erlangung eines

Doktors der Naturwissenschaften (Dr. rer. nat.)

genehmigten Dissertation.

Vorsitz: Prof. Dr. Patrick Rinke

Prüfende der Dissertation:

1. Priv.-Doz. Dr. Philipp Lauber
2. Prof. Dr. Mirko Salewski

Die Dissertation wurde am 27.02.2025 bei der Technischen Universität München eingereicht und durch die TUM School of Natural Sciences am 30.04.2025 angenommen.

SCHOOL OF NATURAL SCIENCES

TECHNISCHE UNIVERSITÄT MÜNCHEN

Integrated modeling of energetic particle-driven Alfvén eigenmodes in Tokamak fusion plasmas

Author:	Virgil - Alin Popa
Supervisor:	Priv.-Doz. Dr. Ph. Lauber
Advisor:	Priv.-Doz. Dr. Ph. Lauber
Submission Date:	27.02.2025

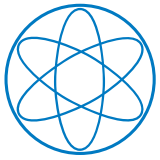

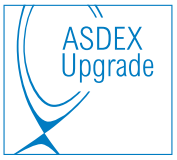

Abstract

Energetic fusion α-particles and fast ions from neutral beam injection must remain well-confined in order to sufficiently heat the background plasma and to avoid highly energetic loads on the first wall. However, these EPs can drive Alfvén eigenmodes (AEs) that in turn perturb the confinement of these EPs leading to redistribution and losses, thereby degrading the overall plasma heating efficiency and reactor performance. However, modeling EP-driven AEs over a full plasma pulse (hundreds of seconds in ITER) is challenging: high-fidelity global gyrokinetic simulations capture the physics but are prohibitively slow for long timescales, whereas reduced fluid or hybrid models run faster at the cost of kinetic fidelity. This trade-off motivates a workflow that balances computational speed and physics accuracy by including kinetic modeling of EP effects. Burning plasma experiments such as ITER require an automated, time-dependent workflow to study energetic particle (EP) stability and Alfvén eigenmodes (AEs) throughout a discharge. The developed approach performs linear stability analyses on successive time slices of a scenario, mapping out AE stability evolution and thus facilitates the investigation of associated EP transport across all phases of a burning plasma discharge. The workflow was implemented within the Integrated Modelling & Analysis Suite (IMAS) data framework in compliance with FAIR principles (Findable, Accessible, Interoperable, Reusable). All simulation inputs and outputs are stored in standardized IMAS data structures, making them easily accessible to different codes. This FAIR-compliant approach ensures that results are reproducible and shareable, enabling seamless integration of experimental diagnostics and simulation data across devices (e.g. JET, ITER, DEMO). By adhering to data standardization, analyses from multiple tokamaks and scenario codes can be directly compared, enhancing collaboration and enabling cross-device consistency in EP stability studies. Using the EP-Stability-WF workflow, several ITER 15 MA DT scenarios (from ASTRA, DINA-JINTRAC, and METIS simulations) were analyzed alongside a JET DT experimental discharge for validation. The automated stability scans identified Toroidal Alfvén Eigenmodes (TAEs) throughout these scenarios, tracking their frequencies and growth/damping rates as the plasma evolved. At present, nominal parameters remained stable throughout the discharge. Phases with the least damped spectra (end of ramp-up) can be identified and further investigated, taking into account different density peaking and/or q-profiles (sawtooth models). In the JET case, the predicted TAE frequencies' temporal evolution agreed with Mirnov coil measurements, capturing the observed frequency general trends and shifts during

sawtooth cycles. These analyses quantified how TAE growth rates depend on different equilibrium profiles and various EPs. Furthermore, coupling the linear stability output into the ATEP transport model demonstrated that the workflow is prepared to analyse how unstable AEs can redistribute EPs, linking the computed AE activity to changes in EP confinement. Improved physics fidelity is planned by incorporating more realistic EP distribution functions, including finite orbit width for trapped particles, and benchmarking the linear predictions against nonlinear global gyrokinetic simulations to develop saturation rules. The coupling between EP stability analysis and bulk plasma transport solvers can be started based on the presented framework, enabling self-consistent feedback of AE-driven EP transport on core plasma profiles.

Zusammenfassung

Energetische Fusions-α-Teilchen und schnelle Ionen aus der Injektion neutraler Strahlen müssen gut eingeschlossen bleiben, um das Hintergrundplasma ausreichend zu heizen und hochenergetische Belastungen der ersten Wand zu vermeiden. Diese EPs können jedoch Alfvén-Eigenmoden (AEs) antreiben, die wiederum den Einschluss dieser EPs stören und zu Umverteilung und Verlusten führen, wodurch die Gesamteffizienz der Plasmaheizung und die Reaktorleistung beeinträchtigt werden. Die Modellierung von EP-getriebenen AEs über einen vollen Plasmapuls (Hunderte von Sekunden in ITER) ist jedoch eine Herausforderung: Globale gyrokinetische Simulationen mit hoher Genauigkeit erfassen die Physik, sind aber für lange Zeiträume unerschwinglich langsam, während reduzierte Fluid- oder Hybridmodelle auf Kosten der kinetischen Genauigkeit schneller laufen. Dieser Kompromiss motiviert einen Arbeitsablauf, der ein Gleichgewicht zwischen Rechengeschwindigkeit und physikalischer Genauigkeit herstellt, indem die kinetische Modellierung von EP-Effekten einbezogen wird. Brennende Plasmaexperimente wie ITER erfordern einen automatisierten, zeitabhängigen Arbeitsablauf zur Untersuchung der Stabilität energetischer Teilchen (EP) und Alfvén-Eigenmoden (AEs) während einer Entladung. Der entwickelte Ansatz führt lineare Stabilitätsanalysen für aufeinanderfolgende Zeitabschnitte eines Szenarios durch, bildet die Entwicklung der AE-Stabilität ab und erleichtert so die Untersuchung des damit verbundenen EP-Transports über alle Phasen einer brennenden Plasmaentladung. Der Arbeitsablauf wurde innerhalb des Datenrahmens der Integrated Modelling & Analysis Suite (IMAS) unter Einhaltung der FAIR-Prinzipien (Findable, Accessible, Interoperable, Reusable) implementiert. Alle Simulationsinputs und -outputs werden in standardisierten IMAS-Datenstrukturen gespeichert, wodurch sie für verschiedene Codes leicht zugänglich sind. Dieser FAIR-konforme Ansatz stellt sicher, dass die Ergebnisse reproduzierbar sind und gemeinsam genutzt werden können, was eine nahtlose Integration von experimentellen Diagnosen und Simulationsdaten über verschiedene Geräte hinweg ermöglicht (z. B. JET, ITER, DEMO). Durch die Einhaltung der Datenstandardisierung können Analysen von mehreren Tokamaks und Szenario-Codes direkt verglichen werden, was die Zusammenarbeit verbessert und eine geräteübergreifende Konsistenz bei EP-Stabilitätsstudien ermöglicht. Unter Verwendung des EP-Stabilitäts-WF-Workflows wurden mehrere ITER 15 MA DT-Szenarien (aus ASTRA-, DINA-JINTRAC- und METIS-Simulationen) zusammen mit einer experimentellen JET DT-Entladung zur Validierung analysiert. Die automatisierten Stabilitätsscans identifizierten Toroidal Alfvén Eigenmoden (TAEs) in diesen Szenarien und

verfolgten ihre Frequenzen und Wachstums-/Dämpfungsraten während der Entwicklung des Plasmas. Derzeit sind die nominalen Parameter während der gesamten Entladung stabil. Die Phasen mit den am wenigsten gedämpften Spektren (Ende des Hochlaufs) können identifiziert und weiter untersucht werden, wobei verschiedene Dichtespitzen und/oder q-Profile (Sägezahnmodelle) berücksichtigt werden. Im Fall von JET stimmte die vorhergesagte zeitliche Entwicklung der TAE-Frequenzen mit den Messungen der Mirnov-Spule überein, wobei die beobachteten allgemeinen Frequenztrends und -verschiebungen während der Sägezahnzyklen erfasst wurden. Mit diesen Analysen wurde quantifiziert, wie die TAE-Wachstumsraten von verschiedenen Gleichgewichtsprofilen und verschiedenen EPs abhängen. Darüber hinaus zeigte die Kopplung der linearen Stabilitätsausgabe mit dem ATEP-Transportmodell, dass der Arbeitsablauf darauf vorbereitet ist, zu analysieren, wie instabile AEs die EPs umverteilen können, und die berechnete AE-Aktivität mit Änderungen des EP-Einschlusses zu verknüpfen. Es ist geplant, die physikalische Genauigkeit zu verbessern, indem realistischere EP-Verteilungsfunktionen, einschließlich endlicher Umlaufbahnbreite für eingeschlossene Teilchen, einbezogen werden und die linearen Vorhersagen mit nichtlinearen globalen gyrokinetischen Simulationen verglichen werden, um Sättigungsregeln zu entwickeln. Die Kopplung zwischen EP-Stabilitätsanalyse und Bulk-Plasma-Transport-Solvern kann auf der Grundlage des vorgestellten Rahmens begonnen werden, was eine selbstkonsistente Rückkopplung des AE-getriebenen EP-Transports auf Kernplasmaprofile ermöglicht.

Contents

1 Introduction, Motivation and Objectives

Magnetic fusion energy (MFE) research has been one of the leading research goals of humankind since the mid-20th century. A crucial stage of this research was achieved once the construction of ITER (originally the International Thermonuclear Experimental Reactor) started[1]. In the machine mentioned above, the physics of burning plasmas will be investigated based on the deuterium-tritium (D-T) fusion reactions:

$$^2D + ^3T \longrightarrow ^4He + ^1n \tag{1.1}$$

One reaction of this type produces a helium ion (also known as an α particle) with 3.52 MeV and a neutron with 14.06 MeV for a total of 17.58 MeV energy released from the mass deficit.

The repulsive Coulomb force between the nuclei quickly overrides nuclear attraction at atomic or molecular distances. Therefore, the kinetic energy of the reactants needs to be considerable because quantum tunneling becomes effective only after a large part of the Coulomb barrier has been penetrated already. As a result, the fusion cross-sections are negligibly small for kinetic energies of less than a few kilo-electron volts (keV).Fusion reaction rates are proportional to both the product of the ion densities and the probability that two ions possess sufficient relative energy to overcome the Coulomb barrier and fuse. As Coulomb collisions are much more likely (100 times) than fusions collisions, plasmas with high thermal energies need to be created such that enough fusion collisions in the Maxwell tail can occur. It can be shown that termperatures $\approx 10 - 30$ keV yield big enough cross sections $< v \cdot \sigma >$ for obtaining large enough fusion powers. Therefore, maintaining a high overall ion density in thermal equilibrium is essential, as it ensures that, even if only a minor proportion of ions are at fusion relevant energies, the absolute number of high-energy collisions remains sufficient to sustain the fusion process. The temperature range for which thermonuclear fusion creates enough fusion power is between $10 - 30$ keV [2].

There are variants to the deuterium-tritium (D-T) reaction, such as the ones presented in Table 1.1. Although aneutronic fusion processes such as: deuterium-deuterium (D-D) and deuterium-helium-3 (D-He^3) fusion are theoretically appealing because of

their reduced neutron production (which may mitigate radioactive waste concerns and alleviate engineering challenges associated with neutron-induced material degradation), they are fundamentally constrained by substantially lower fusion cross-sections compared to the deuterium-tritium (D-T) reaction. As such, for equivalent plasma densities and confinement times, the resultant fusion power yield is markedly lower, necessitating more extreme plasma conditions to achieve comparable energy outputs.

Reactants	**Products**
D - D	T (1 MeV) + p (3 MeV)
D - D	He^3 (0.8 MeV) + n (2.5 MeV)
D - T	He^4 (3.5 MeV) + n (14 MeV)
D - He^3	He^4 (3.7 MeV) + p (14.7 MeV)

Table 1.1: Fusion reactions with relatively large cross-sections.

In fusion reactors based on magnetic confinement, α particles slow down under ideal conditions due to Coulomb collisions with the thermal plasma, a process that is called thermalization. This ensures continuous heating in order to keep the required temperatures for the D-T fusion reaction. For this reason, we have to ensure that the α particles have sufficiently good confinement. Unfortunately, due to various transport processes (to be described later), the confinement is far from ideal, and the particle transport properties on timescale τ_p (particle confinement time) and of plasma energy timescale τ_E must be considered. If we neglect the difference between the two times, the required $n\tau$ to break even and ignition is shown in Fig.1.1.

Breakeven occurs when the fusion energy produced is equal to that used in heating the plasma. This is called the Lawson criterion [3], and the absolute lower limit for the product $n\tau_E$ at $T \simeq 20$ keV is:

$$n\tau_E \gtrapprox 1 \cdot 10^{14} cm^{-3} s \tag{1.2}$$

In toroidally symmetric magnetic fusion devices (tokamaks) such as ITER, the geometry of the confining equilibrium magnetic field B_0 properly ensures the confinement of charged-particle orbits, including fusion α particles. A raw schematic of a tokamak can be seen in Fig1.2. A large magnetic field in the toroidal direction and a smaller poloidal field describe the axisymmetric toroidal device. Large external field coils produce the toroidal field, and a strong toroidal current in the plasma generates the poloidal field. A transformer with the central solenoid as primary and plasma as the secondary winding mainly induces the toroidal current mentioned before. Due to collisional and neoclassical processes the transport is sufficiently small to confine

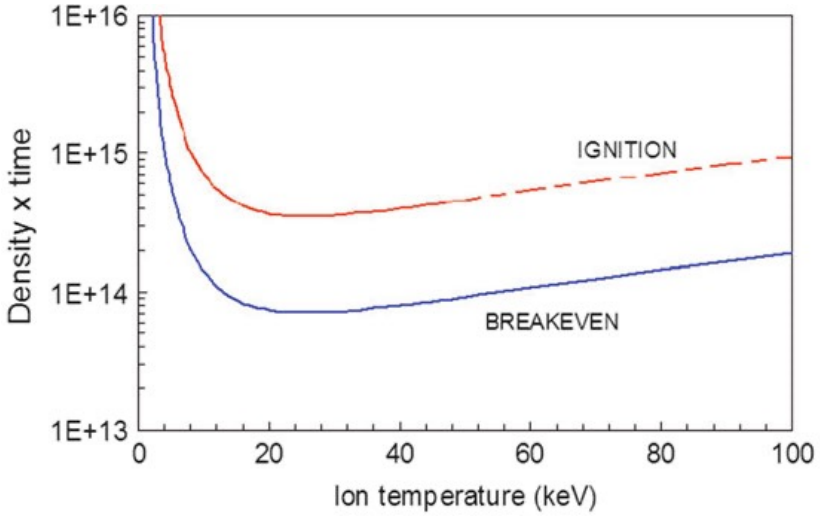

Figure 1.1: The $n\tau$ product for D-T fusion in units of cm^{-3} s, vs. KT_i [4]

α's during their slowing down process. However, concerns arise when the transport is dominated by collective fluctuations driven unstable by α particles via wave-particle resonances. The before-mentioned instabilities may be breaking the toroidal symmetry, leading to increased α-particle radial transport and loss [5].

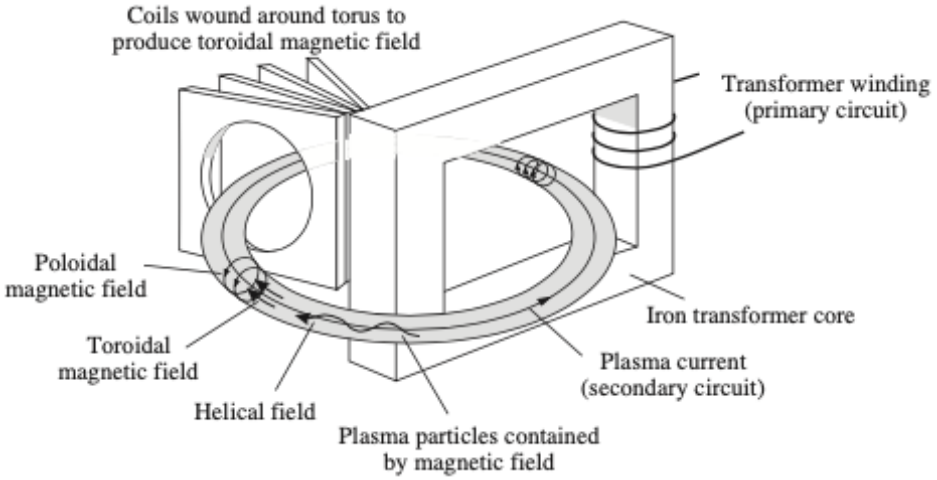

Figure 1.2: Schematic drawing of a tokamak.[6]

These instabilities can be weakly damped Alfvén waves, which resonate with α (supra-thermal) particles[7]. For a typical reactor parameter (density $n \sim 10^{20} m^{-3}$, magnetic field $B \sim 6T$) so-called Toroidal Alfvén Eigenmodes (TAE)[8] with phase velocities of the order of the α-particle velocity before thermalization are expected to

be the most unstable type of perturbations.[6] Because α-particles have an isotropic velocity space distribution function, the velocity gradient stabilizes, and no collective fluctuations are excited around the cyclotron frequency. However, it can be shown that the spatial (radial) gradient can very efficiently provide energy since TAEs tap energy from the radial gradient. Thus, the TAEs' energy grows and flatten the local EPs (αs) gradients (via inverse Landau damping).

An energetic particle will have a larger gyroradius than a thermal particle. This is given by:

$$|q_i| = \frac{|v_{\perp i}|}{\omega_i} \quad \text{with} \quad \omega_i = \frac{Z_i e B}{m_i} \tag{1.3}$$

where q_i is the gyroradius for a particle of species i with mass m_i and charge $Z_i e$ in a magnetic field B. In Fig.1.3, it can be seen that the gyroradius of helium ion is still small compared to the minor radius of the plasma (2m -ITER) but can become an important factor when compared to the length scales of the MHD modes, e.g. TAEs.[9] The geometry of the tokamak breaks the rotational geometry of the poloidal coordinate

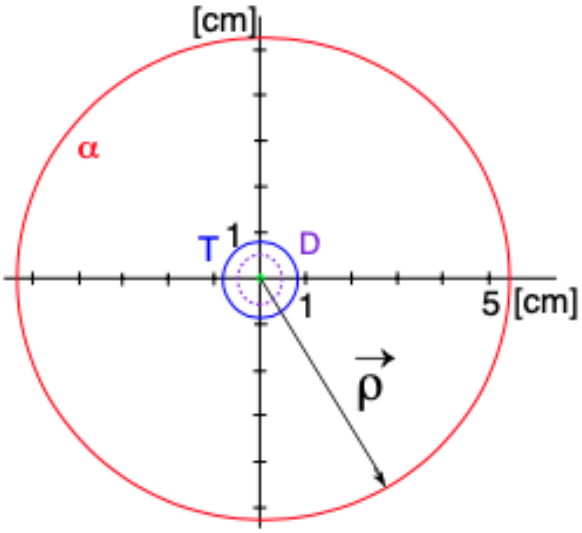

Figure 1.3: Gyroradii (ITER - $B \sim 5T$) for electrons (0.1mm), deuterium (0.6cm), tritium (0.8cm) and helium (5.3cm) ions.[9]

(compared to the cylindrical case) and thus adds more innate frequencies to the system, where an effective transfer of energy between the particles and the plasma waves can occur[9].

Fluid models cannot capture the relevant effects in energetic particle physics because kinetic resonances are an essential ingredient (Vlasov equation). Due to the Alfvén frequencies being much smaller than cyclotron frequency, we can neglect the gyro-motion timescales, i.e. $\frac{\omega_{Alfvén}}{\omega_{ci}} << 1$ is ordered out of the system of equations. The relevant

perturbations have a spatial structure comparable to the Larmor radius and the drift orbit width of the fast ions. The gyrokinetic equations have been constructed to address this physics. It contains a gyro phase-averaged kinetic equation (particles are treated as drifting charged rings, disregarding the particle's motion on the ring) that allows for sharp spatial variation of field perturbations on the scale of the ion gyro-radius.

All previous analyses show that many different AEs with toroidal mode numbers n and poloidal mode numbers m can be partially unstable. Due to the sensitivity of the Toroidal Alfvén Eigenmodes (TAE) properties to the different profiles, an automated way of analysis is required, which leads to various α - particle transport models.

1.1 Motivation and Objectives

Modern fusion research relies on advanced numerical simulations and experimental data analysis to understand energetic particle behavior and plasma instabilities physics on present experiments and predictions towards future burning plasmas.

As discussed before, Energetic Particles (EPs) generated by fusion reactions and by external heating methods such as Neutral Beam Injection (NBI) must be well confined in present and future fusion devices like JET, ITER, or DEMO. However, the EPs' resonant and non-resonant interaction with electromagnetic perturbations can lead to EP transport, which affects the heating efficiency and, thus, the overall performance of the burning plasma, representing an aspect of concern for future reactors. Previous analyses show that to be able to determine the stability limits of weakly damped Alfvénic perturbations and to model the related transport, a non-linear, global, kinetic treatment is necessary [10, 11]. Toroidal Alfvén Eigenmode (TAE) stability exhibits an exponential sensitivity to the underlying plasma profiles—such as density, temperature, and current distributions. Even slight deviations in these equilibrium profiles can lead to pronounced changes in the linear growth rates of TAEs. By employing short time-scale modeling, researchers can decouple the linear instability phase from subsequent nonlinear saturation processes, thereby isolating the fundamental instability mechanisms. Notably, experimental observations from ASDEX Upgrade (AUG) corroborate this sensitivity; transient perturbations in the equilibrium have been shown to trigger rapid destabilization of TAEs, emphasizing the critical importance of precise profile control for achieving robust plasma performance in fusion devices [12]. To study a complete scenario including ramp-up, flat-top and ramp-down that for e.g. at ITER is foreseen to last $>$ 500 seconds, one needs to find a compromise between computational fidelity and speed. Comprehensive codes with high fidelity (e.g. ORB5, - global electromagnetic gyrokinetic particle-in-cell code [13, 14], GTC [15] or GENE [16]) can be used only for relatively short timescales (several ms), due to their extensive computational cost.

Non-linear (gyro-) fluid models [17] can cover longer timescales, but besides the lack of kinetic effects, the deep non-linear evolution still poses some unresolved challenges. Also, direct coupling schemes of high-fidelity simulations and transport codes are presently developed [18], which are also extremely costly and still not complete concerning all relevant physics. Therefore, robust reduced models for the analysis of stability and transport are needed as an additional tool. Currently, the following implementations based on different physics models are available: the critical gradient model [19], the kick model [20], the 'resonance broadening quasi-linear model' (RBQ) [21], and the phase space zonal structure model (PSZS) [22]. Although they are intended to be faster than comprehensive codes, significant effort is still required to identify the fundamental components (such as linear mode features including frequency, damping/growth rate, mode structure, and associated saturation rules) for the reduced models. In addition, to perform multiple linear computations at different time slices of a given scenario (ramp-up, flat-top and ramp-down) a high degree of automatization is required.

In this work, the first automated, time-dependent IMAS (Integrated Modelling & Analysis Suite [23] - partially based on earlier developments [24]) workflow (EP-Stability-WF) is presented and used to provide insight into the stability of Toroidal Alfvén Eigenmodes(TAEs) in different phases of various scenarios. It is based on the equilibrium codes CHEASE [25] and HELENA [26] and different hierarchical models of the linear gyrokinetic eigenvalue code LIGKA [27] that are connected via a centralized IMAS database. A complex workflow (EP-Stability-WF [28]) was created to connect the different stages of the analysis with the database to ensure the reproducibility and consistent interpretation of the different analysis steps. In addition, comprehensive insight in local and global AE physics was necessary to connect the different numerical models in a meaningful way and to leverage the low-fidelity results as input for more expensive global calculations. With this tool, both time-dependent predictive scenario simulations and experimental data can be analyzed. Moreover the workflow provides linear gyrokinetic mode information (frequency, damping/growth rate, radial structure) to the phase-space resolved energetic particle (EP) transport model (ATEP) [29]. To ensure reproducibility, efficiency, and collaboration, the FAIR [30](Findable, Accessible, Interoperable, and Reusable) principles are becoming increasingly important in plasma physics. In this context, FAIR data practices were also one of the motivations of this thesis ,enhancing the workflow used in this dissertation by improving the accessibility and integration of experimental and simulated data. The IMAS (Integrated Modelling and Analysis Suite) framework, which supports standardized data structures and code interoperability, is key in facilitating numerical studies of energetic particle stability, integrated modelling, and Alfvén eigenmodes. Using IMAS-based workflows makes it possible to analyze certain instabilities (e.g. Toroidal Alfvén Eigenmodes (TAEs)) across different plasma scenarios while ensuring compatibility with experimental results from

devices such as JET and ITER. The numerical tools employed in this thesis benefit from a structured, FAIR-compliant approach to data handling, allowing seamless integration of simulation results with experimental diagnostics. This not only improves the efficiency of the workflow but also ensures that findings can be systematically compared and reproduced within the broader fusion research community. By aligning with FAIR principles, this work contributes to developing more reliable and predictive models for energetic particle confinement and stability in future reactors.

To demonstrate the capabilities of this workflow, several ITER scenarios for Deuterium Tritium plasmas are analyzed: a time-independent scenario generated by the ASTRA [31] transport code, a time-dependant predictive scenario generated by the METIS [32, 33] transport code, and finally the newest ITER baseline scenario with 5.30 [T], 15 [MA] Deuterium Tritium plasma given by the DINA [34] - JINTRAC [35] transport workflow which combines a free boundary equilibrium evolution code with the 1.5D core/2D SOL code. Here time-dependent means that an automated linear stability analysis is performed for different time points of a simulated ITER scenario. These time points are sufficiently separated in time (typically 0.5s - 5s), i.e. it is assumed that the equilibrium evolution time is much slower than the Alfvén time scales connected to the linear and non-linear TAE physics.

The Joint European Torus (JET) has been until very recently the world's largest tokamak facility and has been instrumental in advancing fusion research. Located in Culham, UK, JET has been operational since 1983 and holds the world record for fusion power production. Its unique capabilities, particularly after the installation of the ITER-like wall in 2011, make it an ideal test bed for validating physics models and predictions relevant to ITER. In this work, we also analyze JET experimental data using the EP-Stability-WF workflow to validate our numerical tools against real tokamak measurements. This represents the first time that a global gyrokinetic code is used to analyze JET data in a time-dependent manner, thus demonstrating the capabilities of the code in a multi-fast species scenario (Hydrogen, Deuterium, Tritium and Helium). In addition, the EP-Stability WF has been already used to model experiments and scenario predictions at ASDEX Upgrade, JT-60SA, VNS, DEMO [Ph. Lauber private communication], TCV [36].

The thesis is organized as follows: section 3 contains a technical description of the models and numerical tools, section 4 gives an overview of the scenarios and parameters chosen for the computation. The presentation of the results (5) is split into three subsections: the evolution of damped TAEs without EPs, what happens to them when EPs are added, convergence tests to ensure numerical efficiency and code limitations, and finally the application of the EP-Stability-WF to JET data where the code is also coupled to the ATEP transport code. In the end, section 6 presents the conclusions and outlook of the thesis.

2 Theory

This chapter provides an overview over the theoretical framework for analyzing the stability of energetic particles in tokamaks. Particle dynamics in magnetic fields, wave-particle interactions, modeling techniques, and the role of Alfvén eigenmodes in magnetic confinement devices like JET or ITER are covered.

2.1 Framework

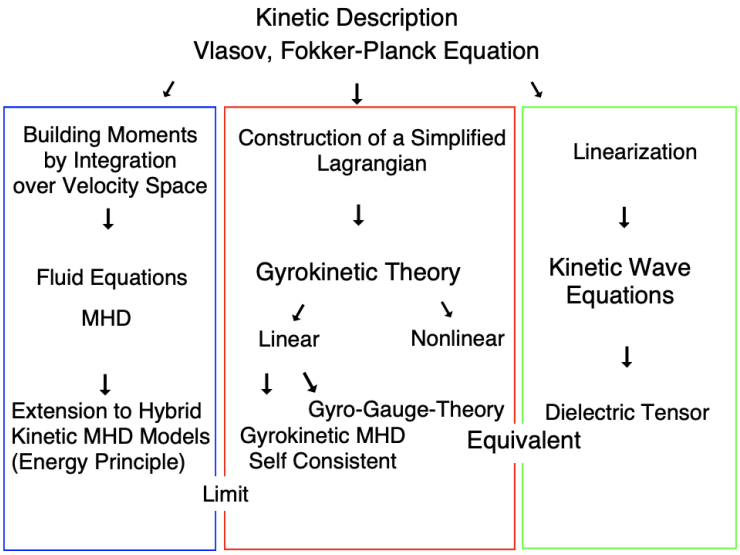

Figure 2.1: Overview of the branches of kinetic plasma description.[9]

Different theoretical frameworks can be used to study energetic particle stability in a tokamak; three can be seen in Fig. 2.1. As mentioned above, kinetic equations are needed for α-physics. Theoretically, the whole Maxwell - Vlasov system of equations must be solved in the toroidal geometry. This is very difficult and not practicable due to the complexity of the problem. The system can be simplified in three ways: using the Kinetic Wave Equations, MHD - hybrid models (treating background as a fluid and EPs kinetic), or the framework of Gyrokinetic Theory.

This work used LIGKA code, which is based on the Gyrokinetic framework. This model consists of three equations: the quasi-neutrality equation (QN), the gyrokinetic moment equation (GKM), and the gyrokinetic equation (GKE) itself. Electrostatic and electromagnetic potentials, as well as the perturbed distribution functions, are the unknowns in the system of equations[9]. Before describing the model equations in detail, a few basic concepts need to be introduced first to offer a better understanding of the model.

2.1.1 Requirements for the gyrokinetic solver

All linear and most non-linear models assume as initial condition an equilibrium state. This comprises an magnetic equilibrium given by radial force balance and radial profiles for fluid moments such as n,Ti,Te, etc.

As input, the equilibrium quantities (such as B, j, P) and the profiles of all species (T,n,F_{EP}) are needed where the kinetic profiles are required to add up to the total MHD equilibrium pressure. In this case taken from an MHD equilibrium solver and inputs generated by the transport code METIS or ASTRA or as measured in the experiment.

A 2d equilibrium code solves the Grad-Shafranov equation for the magnetic field and the poloidal current profile.

$$\nabla \cdot \frac{1}{R^2} \nabla \psi = \frac{j_\phi}{R} = -p'(\psi) - \frac{1}{R^2} T T'(\psi) \tag{2.1}$$

The toroidal plasma current density is represented by j_ϕ, while R denotes the major radius of the torus. The prime symbol indicates differentiation with respect to ψ. The equilibrium properties, whether in a tokamak, reversed field pinch, or other configurations, are governed by the two free functions $p'(\psi)$ and $TT'(\psi)$. Adding appropriate boundary conditions determines the poloidal cross section of the plasma either at the last closed flux surface (used in this work) or in an open field line region.More information on the equilibrium codes can be found in section 3.

2.1.2 Particle motion in a magnetic field

In the core of a tokamak we have a fully ionized gas trapped by strong magnetic fields, as described by the solution of the the Grad-Shafranov equation above. Lorentz force is the most important force when it comes to the description of particle orbits in a magnetic field. It is perpendicular to the velocity of the particle and the magnetic field. By neglecting for now the small but fluctuating electric field component we have:

$$\mathbf{F} = q\mathbf{v} \times \mathbf{B} \tag{2.2}$$

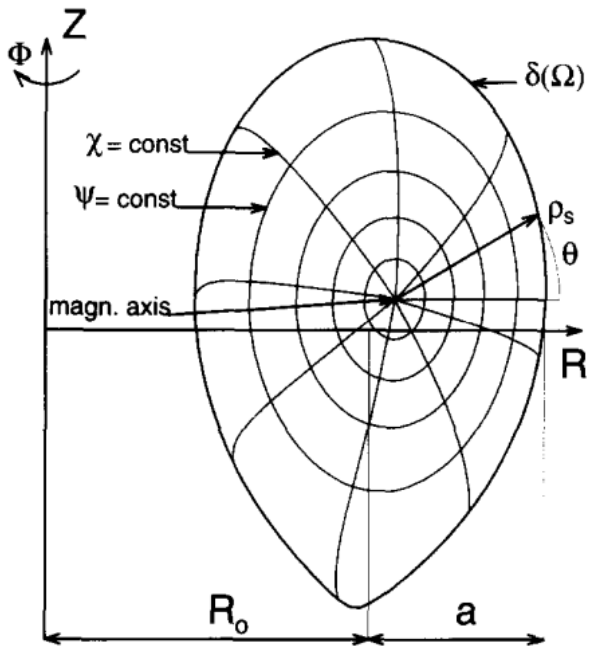

Figure 2.2: Taken from [25].Cylindrical coordinates R, Z,θ in toroidal geometry.

According to the equation, we can see that when taking into account only the perpendicular motion, the particle gyrates around a magnetic field line. Gyrofrequency (ω_c) is the frequency associated with such a motion of the particle. The radius associated with this gyration is the Larmor radius (ρ_L):

$$\omega_c = \frac{\mid q \mid B}{m} \qquad \rho_L = \frac{v_\perp}{\omega_c} \tag{2.3}$$

where q is the charge of the particle, B the magnetic field strength, m the mass of the particle and $v_\perp$ is the component of the particle's velocity perpendicular to the magnetic field. By taking into account the parallel velocity, we observe that the particle moves freely, along the magnetic field lines. This results in a helical motion of the particle perpendicular to **B** (magnetic field). Any additional forces perpendicular to **B** lead to drifts. Drifts are the deviations of the particle motion due to different forces from the helical motion. In guiding center theory, the full equations of motion for a charged particle in a magnetic field are averaged over the rapid cyclotron (gyromotion) dynamics. This transformation into guiding center coordinates yields an expression for the slow drift velocity of the particle's guiding center. In particular, when an external force **F** acts on the particle, the resultant drift velocity is given by:

$$\mathbf{v}_{drift} = \frac{\mathbf{F} \times \mathbf{B}}{qB^2} \tag{2.4}$$

we can notice that if $\mathbf{F}$ will depend on charge q, v_{drift} will not. Otherwise the velocity depends on the charge and will have opposite drifts directions for electrons and ions. In a tokamak, important drifts are: ∇B for which $\mathbf{F} = -\frac{mv_\perp^2}{2B}\nabla B$ and curvature drifts which has $\mathbf{F} = \frac{mv_\parallel^2}{R_c^2}R_c$.

2.1.3 Orbit coordinates and orbit space

An important point here is the adiabatic invariant μ, which is proportional to the perpendicular velocity $v_\perp$ and proportional to $\frac{1}{B}$.

$$\mu = \frac{mv_\perp^2}{2B} \tag{2.5}$$

This invariant is very important because it causes a fraction of the particles that follow the magnetic field lines to be trapped (mirrored). As a particle moves from a weak-field region to a strong-field region, it sees an increasing $\mathbf{B}$, and therefore $v_\perp$ must increase in order to keep μ constant. Since the total energy of the particle must be conserved, $v_\parallel$ must decrease. If $\mathbf{B}$ is high enough $v_\parallel$ becomes zero and the particle is "reflected" back to the weak-field region. This effect works on both ions and electrons and it is called magnetic mirror trapping.

The motion of charged particles in a tokamak is governed by the Lorentz force, which determines their trajectory in a six-dimensional phase space consisting of three spatial and three velocity coordinates. However, under specific assumptions, this phase space can be reduced to three essential coordinates, commonly referred to as orbit coordinates. The connection between symmetries and constants of motion in Lagrangian dynamics plays a crucial role in this reduction. According to Noether's theorem, if one can identify a continuous symmetry of the system, expressed as the invariance of the Lagrangian under a coordinate transformation, then a corresponding conserved quantity can be derived. For example, the toroidal symmetry inherent in tokamak geometry implies that the Lagrangian is invariant under rotations about the toroidal axis, leading directly to the conservation of toroidal canonical momentum. Such conserved quantities not only further constrain the particle trajectories but also facilitate the reduction of the phase space dimensionality, allowing the dynamics to be effectively described using a smaller set of orbit coordinates.

The primary assumptions that enable this dimensional reduction are:

1. **Toroidal Symmetry** - The toroidal geometry of the tokamak allows for the

elimination of one spatial coordinate.

2. **Magnetic Field Approximation** - In a strong guide field, the magnetic field is sufficiently dominant and nearly uniform over the particle's Larmor radius, so that its variation during one cyclotron orbit is minimal. This uniformity permits the averaging over the fast gyromotion, thereby decoupling it from the slower guiding center dynamics and effectively reducing the dimensionality of the velocity space by one.

3. **Unperturbed Motion** - If the ion motion remains unaltered as it revisits the same poloidal location, an additional spatial dimension can be eliminated.

A widely used set of orbit coordinates is given by the constants of motion (COM):

$$(E, \mu, P_\phi; \sigma) \tag{2.6}$$

where:

- E is the particle energy,
- $\mu = \frac{mv_\perp^2}{2B}$ is the magnetic moment,
- $P_\phi = q\psi + mv_\parallel RB_\phi/B$ is the toroidal canonical angular momentum, parallel velocity $v_{||}$ is defined as the projection of a particle's velocity v onto the direction of the magnetic field B. It is a signed quantity: it is positive if the particle moves in the same direction as the magnetic field and negative if it moves in the opposite direction.
- σ is an auxiliary parameter used to distinguish between orbits with identical COM values and different parallel velocity sign with repsect to the B field.

An alternative, physically intuitive set of orbit coordinates is:

$$(E, p_m, R_m) \tag{2.7}$$

where:

- p_m represents the pitch angle at the maximum major radius position R_m,
- R_m is the radial position at which the orbit reaches its furthest excursion from the magnetic axis.

This coordinate system is well-bounded, providing a clear distinction between different orbit types in a tokamak. Orbit space is a three-dimensional phase space spanned by the coordinates (E, p_m, R_m), where each point corresponds to a specific fast-ion trajectory. The structure of this space is determined by the magnetic equilibrium of the tokamak and exhibits distinct topological regions corresponding to different orbit classes.

The six fundamental orbit types in a tokamak are:

1. **Co-Passing Orbits** - Orbits that fully encircle the magnetic axis with a consistently positive pitch ($p > 0$).

2. **Counter-Passing Orbits** - Similar to co-passing but with a consistently negative pitch ($p < 0$).

3. **Trapped Orbits** - Orbits that do not complete a full toroidal circuit and periodically reverse their parallel velocity direction (p changes sign).

4. **Potato Orbits** - High-energy trapped orbits that expand significantly in radial extent.

5. **Stagnation Orbits** - Non-circulating orbits with strictly positive pitch ($p > 0$), remaining close to a single flux surface.

6. **Counter-Stagnation Orbits** - Similar to stagnation orbits but with a strictly negative pitch ($p < 0$).

Additionally, lost orbit regions exist where particles collide with the tokamak wall or enter the divertor region. The evolution of such regions is energy-dependent:

- At **low energies**, lost orbits appear at the low-field side (LFS) for ions lacking sufficient energy to remain confined.

- At **higher energies**, counter-passing ions drift into the divertor or outer walls, increasing particle losses.

A key feature of orbit space is the variation of orbit types with energy. At low energies, most orbits are co-passing, counter-passing, or trapped. As energy increases, stagnation, potato, and counter-stagnation orbits become more prevalent, affecting the transport and confinement of fast ions in high-performance fusion plasmas. An example of such orbits is shown in Fig. 2.3.

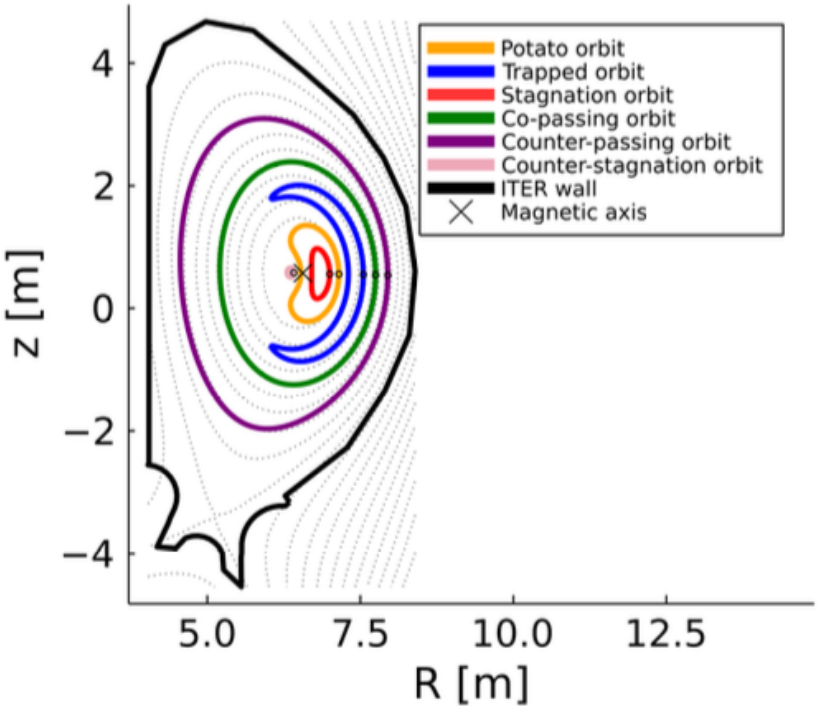

Figure 2.3: An illustration of the six distinct fast-ion orbit types in a standard tokamak magnetic equilibrium is presented. Each orbit corresponds to a 3.5 MeV α-particle trajectory, with variations in the initial pitch $(v_\parallel/v)$ and starting position (R, z), leading to different orbital paths. Magnetic flux surfaces are represented by dotted lines for reference, while the magnetic axis (plasma center) is marked with a black cross. The orbits are computed using the planned ITER magnetic test equilibrium with $B_0 = 5$ T. This figure is taken from [37].

2.1.4 EP distribution function

The EP distribution function describes the number of fast ions at a given spatial coordinate x, velocity v, and time t. In a fully three-dimensional representation, the function depends on three spatial and three velocity coordinates. The distribution funtction describes how the different orbits are populated. Therefore, the same coordinate representations as above are possible.

Furthermore, the velocity coordinates can also be reduced under certain conditions, as explained above. If the relative variation of the magnetic field is sufficiently small and changes slowly, the velocity space can be described using only two coordinates instead of three.

For instance, in the Advanced Transport model for Energetic Particles (ATEP) [29], the transport equation is cast as a continuity equation for the energetic particle distribution function F_z in the phase space of constants of motion, namely (P_ϕ, E, Λ).

Here, P_ϕ denotes the canonical toroidal momentum, E represents the energy, and Λ is defined as $\Lambda = \frac{\mu B_0}{E}$. An example of a distribution function for fast hydrogen particles is shown in Fig.2.4.

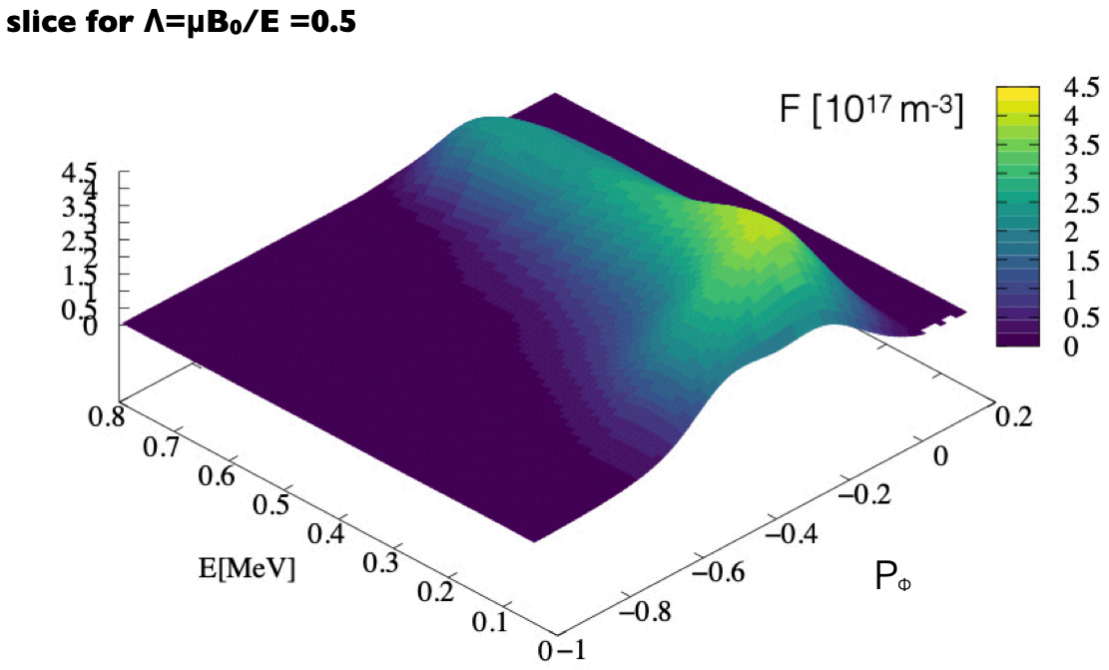

Figure 2.4: Adapted from [29]. Distribution function of energetic hydrogen particles, #100015/1, in ITER's off-off-axis beam configuration.

2.1.5 Wave - particle resonant interaction

Some energetic particles possess velocities that are comparable to the phase velocity of certain magnetohydrodynamic (MHD) wave modes such as the Toroidal Alfvén Eigenmode (TAE). When the particle velocity matches the phase velocity of MHD waves such as the shear or compressional Alfvén waves, it can lead to resonant interactions. This can lead to a transfer of energy from the particles to the wave, which in turn can transport the fast particles away from the core of the plasma. As such, particles can be accelerated or decelerated as a result of their interaction with a wave. What is called Landau damping [38] (LD) is a known result of this interaction. We will talk about this process in a one-dimensional electrostatic system. Waves have the propagation velocity $v_{phase} = \frac{\omega}{k}$. If a particle moves with $v = v_{phase}$, it will not be accelerated or decelerated by the wave. If $v < v_{phase}$ the particle gains energy from the wave

because of the electric field force felt by the particle from the potential of the wave $E(x) = -\nabla\phi(x)$. And finally, if $v > v_{phase}$ we have a transfer of energy from the particle to the wave. The net energy transfer strongly depends on the gradient of the distribution function locally around v_{phase}.

Usually we deal with a Maxwellian distribution in which the gradient of the distribution is negative for all the positive values of v. From Fig.2.5 we can see that in a Maxwellian distribution there are more slow particles than fast ones, so the overall effect will dampen the wave. On the other hand if the distribution is not Maxwellian,

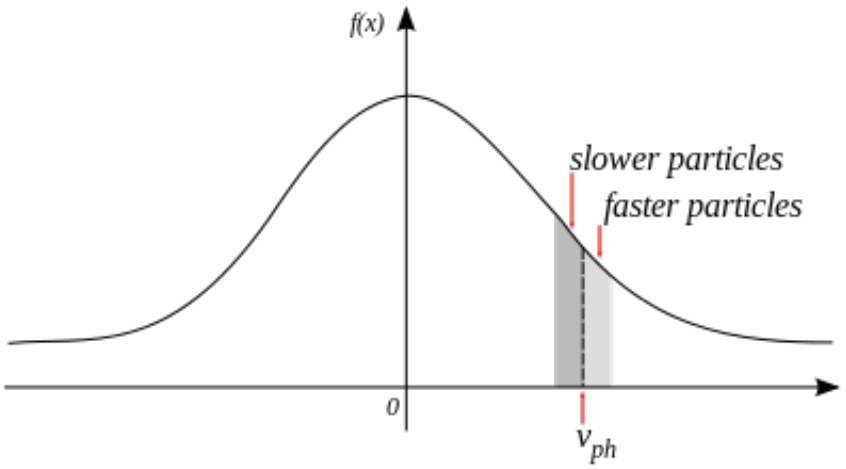

Figure 2.5: Maxwellian distribution in an ideal plasma.[39]

as seen in the bump-on-tail distribution in the Figure 2.6, it can be unstable over a range of wave-numbers. Those waves with phase velocity in positive gradient region would lead to resonant drive of the perturbation and thus lead to a linearly unstable system. In the case of an α - particle distribution, there is no bump-on-tail type of the free available energy of the system, but a radial energetic particle gradient that can act as a source of drive. In contrast to the classical bump-on-tail scenario, the α-particle distribution features a radial gradient in energetic particles, which supplies a source of free energy capable of driving instabilities. This radial drive mechanism is naturally embedded in the kinetic description of the plasma, where the collisionless, non-relativistic Vlasov equation governs the microscopic dynamics of a fully-ionized, confined plasma.

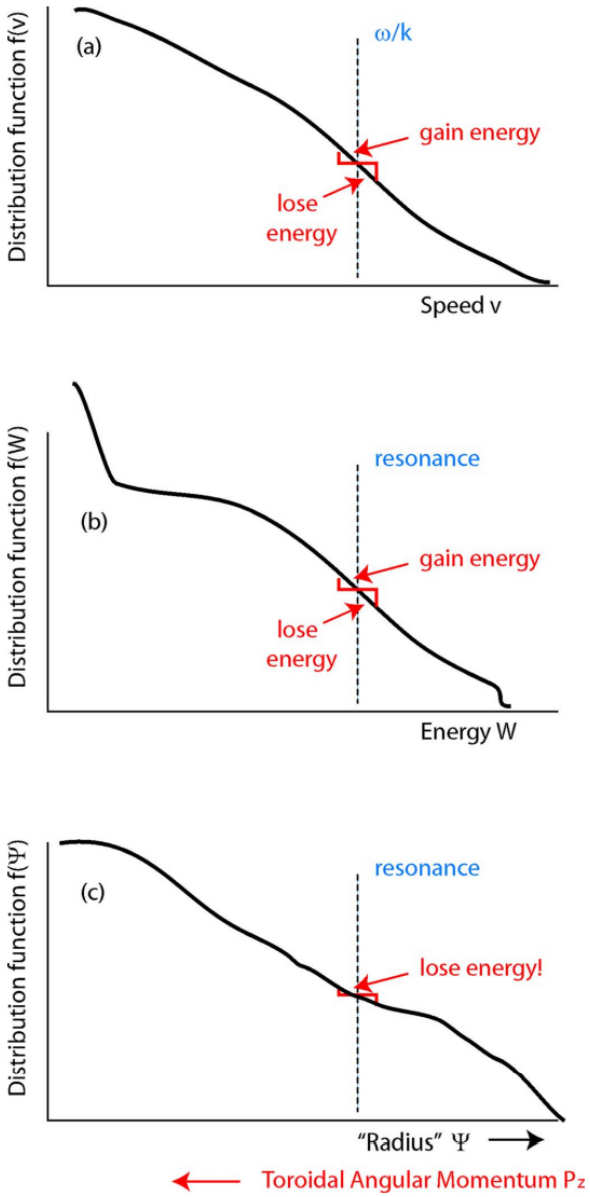

Figure 2.6: This Figure is adapted from [40] Illustration of how the EP drive or damping depends on the slope of the distribution function: Top: Classic Landau damping: When the distribution function decreases monotonically, more particles extract energy from the wave than supply it, leading to wave damping. Middle: Energy distribution: Because the energy distribution is generally monotonically decreasing, the wave is damped. Bottom: Peaked distribution: Typically, the distribution function peaks on axis. Since the toroidal angular momentum P_ζ varies with radius in the opposite way to the flux function, a peaked distribution produces a positive gradient in $\frac{\partial f}{\partial P_\zeta}$, thereby transferring net energy to the wave.

2.1.6 Kinetic approach for collective plasma behaviour

The kinetic theory of a plasma describes the state of a plasma given by its microscopic interactions and the motion of its constituents. By considering a fully-ionized, confined plasma we assume that its behaviour can be described by the collisionless non-relativistic Vlasov equation [41]. In this formulation, the electric E and magnetic B fields represent the macroscopic, ensemble-averaged mean fields. These averaged fields include both the steady, background components responsible for plasma confinement and the perturbed fields arising from collective effects, such as plasma modes and instabilities.

$$\frac{\partial f_s}{\partial t} + \mathbf{v} \cdot \nabla f_s + \frac{q_s}{m_s}(\mathbf{E} + \mathbf{v} \times \mathbf{B}) \cdot \frac{\partial f_s}{\partial \mathbf{v}} = 0 \tag{2.8}$$

This equation describes the evolution of the six-dimensional distribution function phase space of a plasma species s where the right hand side can have a collision operator or sources/sinks added if required. In hot fusion plasmas, the typical non-linear timescale is short compared to the collisional timescale, meaning that the collision operator can be neglected.

In order for the description of the system to be complete, Vlasov equation needs to be coupled to the Maxwell equations which describe electromagnetic fields:

$$\nabla \times \mathbf{B} = \mu_0(\mathbf{J} + \epsilon_0 \frac{\partial \mathbf{E}}{\partial t}) \tag{2.9}$$

$$\nabla \times \mathbf{E} = -\frac{\partial \mathbf{B}}{\partial t} \tag{2.10}$$

$$\nabla \cdot \mathbf{E} = \frac{\rho}{\epsilon_0} \tag{2.11}$$

$$\nabla \cdot \mathbf{B} = 0 \tag{2.12}$$

where ρ is the charge density in the plasma, $\mathbf{J}$ is the current density and ϵ_0 and μ_0 are the permitivity and permeability of free space. The above equations are also six-dimensional and impractical to solve for fusion plasmas.

2.1.7 Gyrokinetic Theory

Because of the complexity of the full Vlasov - Maxwell system, a theoretical framework with reduced dimensionality is needed. One of these alternative methods is represented by Gyrokinetic Theory. It takes the Vlasov - Maxwell system of equations in the presence of a magnetic field and transforms the variables in which, by ordering, the gyro-phase is ignored. First, one transforms from particle coordinates (**x**,**v**,t) to guiding-center

coordinates ($\mathbf{X}$,$v_\parallel$,$\mathbf{v}_\perp$,φ,t). These coordinates are related by:

$$\mathbf{x} = \mathbf{X} + \frac{mc}{q\mathbf{B}}\hat{b} \times \mathbf{v} \tag{2.13}$$

$$\mathbf{v}_\perp = v_\perp(\hat{e}_1 cos\varphi - \hat{e}_2 sin\varphi) \tag{2.14}$$

$$\hat{e}_1 \times \hat{e}_2 = \hat{b} \tag{2.15}$$

This transformation allows removal of fast gyration from the system and reduction of the dimensionality of phase space from six-dimensional to five-dimensional. This leads to equations in terms of guiding-center i.e. averaging the particle motion around the gyro-motion. Now perturbations are introduced in the system: by taking into account that they are comparable to the ion ρ_i we can further transform to so-called gyro-centers. Because of this we can think of particles as moving charge rings instead of point charges. This process yields the gyrokinetic model[42]. According to reference[43] firstly, we take the linear gyrokinetic quasi-neutrality condition (QNE):

$$0 = \sum_s e_s \int d^2v\{J_0 f\}_s + m_i\nabla_\perp \cdot \frac{n_i\nabla_\perp\delta\phi}{B^2} + \frac{3P_{i\perp}}{4B^2} + \nabla_\perp^4\delta\phi \tag{2.16}$$

in which f is the perturbed distribution function, the first term is a sum over all species (ions, fast ions, f, and J_0) and the polarisation terms (expanded up to 4th order in $k_\perp\ \varrho_i$), which only applies to ions. Next, the linear gyrokinetic momentum equation (GKM) which is the force balance equation:

$$\begin{aligned} -\frac{\partial}{\partial t}\frac{e}{m}\nabla_\perp\frac{n_0}{B^2}\nabla_\perp\phi + \nabla A_\parallel \times \mathbf{b}\cdot\nabla(\frac{\nabla\times\mathbf{B}}{B}) + (\mathbf{B}\cdot\nabla)\frac{(\nabla\times\nabla\times\mathbf{A})\cdot\mathbf{B}}{B^2} \\ = -\sum_a e_a\int\frac{4\pi}{c}\mathbf{v}_d\cdot\nabla J_0 f_a d^3\mathbf{v} + \frac{c}{v_{A0}^2}\frac{3v_{th,a}^2}{4\Omega_a^2}\nabla_\perp^4\frac{\partial\phi(x)}{\partial t} \\ + \mathbf{B}\cdot\nabla(\frac{4\pi e_a^2 n_{a0}v_{th,a}^2}{2Bm_a c^2\Omega_a^2}\nabla_\perp^2 A_\parallel) + \mathbf{b}\times\nabla(\frac{2\pi e_a n_{0a}v_{th,a}^2}{B\Omega_a})\cdot\nabla\nabla^2\phi \end{aligned} \tag{2.17}$$

in which on the LHS we have the inertia term, the parallel equilibrium current term followed by the field line tension and on the RHS the pressure term with the higher order Larmor radius corrections. By separating the perturbed part from the equilibrium part we can write the linear gyrokinetic equation (GKE):

$$\frac{\partial f_a}{\partial t} + (v_\parallel\mathbf{b} + \mathbf{v}_d)\cdot\nabla f_a = [\frac{\mathbf{b}\times\nabla f}{eB}\cdot\nabla - \frac{\partial f}{\partial E}\frac{\partial}{\partial t}] \quad J_0 \quad [\delta\phi - (1 - \frac{\mathbf{v}_d\cdot\nabla}{i\omega})\delta\psi] \tag{2.18}$$

with $\mathbf{v}_d = -\frac{\mathbf{b}}{eB} \times (mv_\parallel^2(\mathbf{b}\cdot\nabla)\mathbf{b} + \mu\nabla B)$ the drift velocity, ϕ the electrostatic potential, ψ the electromagnetic superpotential ($\partial_t \delta A_\parallel(\mathbf{x}) = -\mathbf{b}\cdot\nabla\delta\psi(\mathbf{x})$) and $J_0 = J_0(\rho k_\perp)$ the gyro-average operator.

In order to solve this system of equations one has to integrate over particle orbits, that leads to a non-linear eigenvalue problem. As a result one obtains eigen-frequencies, growth rate and global mode structure. Having the equilibrium and other information on the plasma, it is possible to solve the gyrokinetic equations both locally and globally. In general, global analysis is necessary, but local results are often useful and much faster to calculate, as will be demonstrated below when describing the EP-WF's methodology.

2.2 Toroidal Alfvén Eigenmodes (TAE)

Toroidal Alfvén Eigenmodes (TAE) are the prototype of all Alfvénic Eigenmodes (AE)[44]. They have a frequency inside the shear Alfvén continuum gap and their mode structure is given by the coupling of two counter-propagating regular shear Alfvén waves. TAEs can be excited through resonance by fast particles and fusion products because their parallel group velocity in toroidal devices is typically of the same order as parallel particle speed. These modes are dangerous for particle transport because the perpendicular group velocity can be neglected and thus, the resonant condition can be maintained effectively. However, recent studies indicate that the presence of TAEs may suppress small-scale turbulence either directly through a dilution effect or indirectly via coupling to zonal flows [45].

The shear Alfvén wave dispersion relation in a cylinder is:

$$\omega^2 = k_n^2 v_A^2 = (\frac{nq-m}{qR})^2 v_A^2 = (\frac{nq-m}{qR})^2 \frac{B^2}{n_i m_i \mu_0} \tag{2.19}$$

where the ions density, n_i - profile determine the solution with $\omega^2 \sim \frac{1}{n}$. In cylinder, the dashed lines from Fig.2.7 left side we can see that the solutions for different m, $m+1$ can cross. In a tokamak, the same figure shows that the crossing is replaced by gaps due to toroidal corrections of $\sum_m \omega^2 = k_m^2 v_A^2$.

The poloidal coupling is due to the periodicity of the magnetic field in poloidal direction. This leads to the existence of a gap between the two continua.

The two 'bands' correspond to a localization of the wave in either the 'good' curvature or the 'bad' one i.e. the low or high field side of the torus, respectively. The radial localization of the gap is determined by:

$$k_{\parallel m}(r_0) + k_{\parallel m+1}(r_0) = 0 \tag{2.20}$$

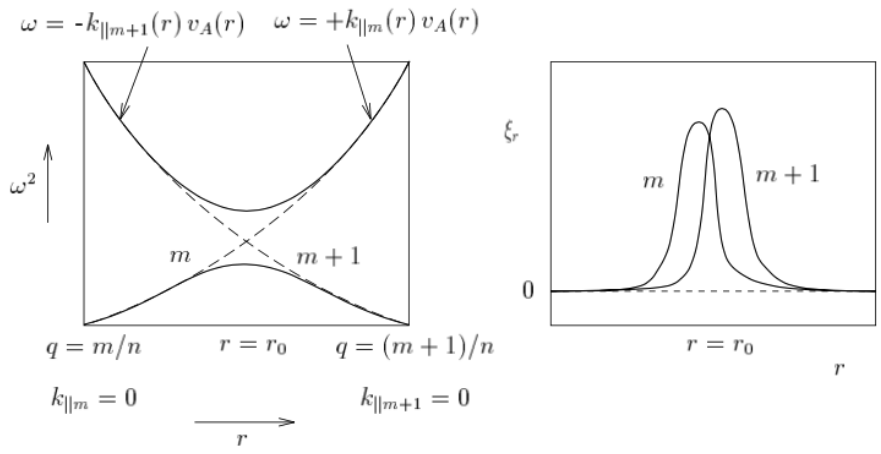

Figure 2.7: Coupling of poloidal harmonics in a torus and the corresponding TAE eigenfunctions.[6] In this thesis the notation used for TAE is (n, m) where n is the toroidal mode number and m is the poloidal mode number, but TAE has $m, m+1$ as main harmonics.

This is equivalent to the position where:

$$q(r_0) = \frac{m + \frac{1}{2}}{n} \tag{2.21}$$

with the width of the gap being described by:

$$\Delta\omega \sim \epsilon\omega_A \tag{2.22}$$

and mode width is given by:

$$\Delta_{AE} \sim \frac{r_0}{m} \tag{2.23}$$

Thus, investigating radially localized regions of TAEs gaps taking into consideration various toroidal (n) and poloidal (m) mode numbers requires a closer look at the $q(r)$ - profile. Analysis of equilibria for large ranges of n and m in is one of the first steps of this thesis. In Fig.2.8 we can see the $q(s_{TAE})$ of $m = n, n+1, n+2$ for different n.

2.2.1 Local solution inside the gap

Starting with the analytical model for TAEs, a TAE frequency including beta correction is available $\omega_{TAE} = v_A/2q_{TAE}R$ [46].

According to [47] the characteristic frequency of TAE in toroidal plasmas with

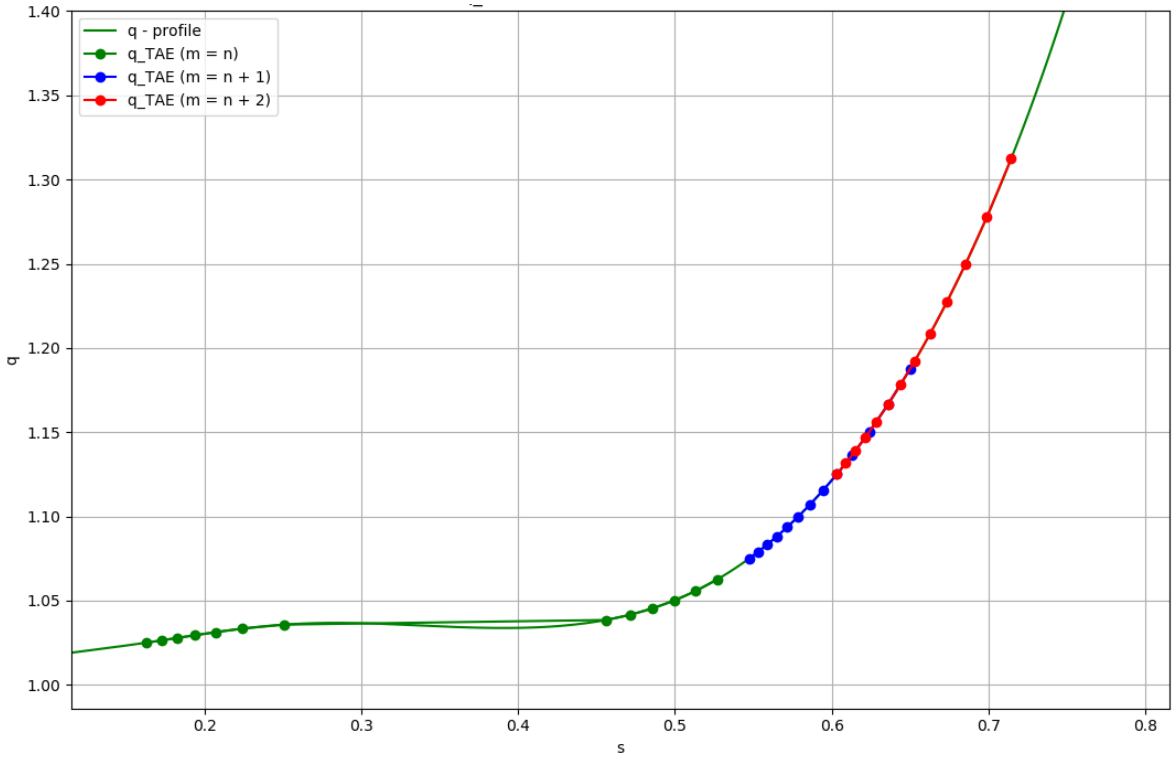

Figure 2.8: The safety factor (q - profile) and the rational surfaces $q(s_{TAE})$ of $m = n, n+1, n+2$ for different n

$q^2\bar{\beta} \ll 1$ is calculated using the formula:

$$\omega_{TAE} = \frac{1}{2q} \frac{\mid 2 - \sqrt{1 + \frac{3\epsilon_{g2}^2}{4}} \mid}{\sqrt{1 - \frac{\epsilon_{g2}^2}{4}}} \tag{2.24}$$

where $\bar{\beta} = \frac{\beta_s}{1+\beta_s}$ and $\beta_s = \frac{c_s^2}{v_A^2}$ for high q, which is characteristic for the core region of the tokamaks, and $\epsilon_{g2} = \frac{k^2-1}{k^2+1}$ describing higher order geometry effects (plasma elongation).

2.2.2 Damping mechanisms

In tokamak plasmas, TAEs are subject to several damping mechanisms arising from kinetic effects and resonant wave-particle interactions.

Continuum damping is a fundamental mechanism by which toroidal Alfvén eigenmodes (TAEs) lose energy in tokamak plasmas. It arises because the TAE frequency typically

lies near the continuous spectrum of shear Alfvén waves, whose local frequencies vary with radial position due to plasma inhomogeneity. In regions where the TAE frequency approaches the local continuum, the discrete mode can resonantly couple to these continuum modes, leading to efficient energy transfer. This resonant absorption results in rapid phase mixing, which effectively damps the global TAE and limits its amplitude and lifetime.

Radiative damping results from the coupling of the discrete TAE mode to kinetic shear Alfvén waves. As described in the last section, when the TAE frequency, ω, lies near the edge of this gap, energy can be radiated into continuum modes, thereby damping the TAE. Finite ion Larmor radius effects and equilibrium profile variations determine the effectiveness this damping mechanism.

Ion Landau damping occurs when ions with velocities near the parallel phase velocity of the wave,

$$v_{||} \approx \frac{\omega}{k_{||}},$$

resonate with the TAE. The resonant ions extract energy from the mode, leading to the damping. Given that the ion thermal speed is typically lower than that of electrons, the efficiency of ion Landau damping is highly sensitive to the ratio ω/v_{thi} and to the gradients of the ion distribution function.

Similarly, electron Landau damping involves the resonant interaction between electrons and the TAE. If the gradient of the electron distribution function is steep, significant damping may occur. Studies have demonstrated that this mechanism can strongly influence the stability of TAEs due to the higher thermal velocities of electrons[48].

In tokamaks, a substantial fraction of electrons are magnetically trapped by the magnetic mirror effect. These trapped electrons bounce between mirror points and are subject to collisional processes that relax their non-Maxwellian features. The collisional damping of these trapped electrons extracts energy from the TAE, especially in regimes of moderate collisionality and high trapped-particle fraction.

In order to obtain instability, the drive from fast particles, such as α - particles, has to overcome the sum of all damping.

2.2.3 From local to global solution

A Fourier expansion in the poloidal angle is employed to preserve the complete resonance structure, ensuring the approach remains valid even for low q values.By retaining the $m \pm 1$ sidebands and accounting for both geodesic curvature and the coupling to sound waves through an appropriate approximation of the propagator integrals (fast circulating particle approximation), a local dispersion relation valid for many types of AE can be derived [44, 49] as follows:

$$\omega^2\left(1-\frac{\omega_{*p}}{\omega}\right)-k_\parallel^2\omega_A^2R_0^2=2\frac{v_{thi}^2}{R_0^2}\Bigg(-\Big[H(x_{m-1})+H(x_{m+1})\Big] + \tau\left[\frac{N^m(x_{m-1})N^{m-1}(x_{m-1})}{D^{m-1}(x_{m-1})}+\frac{N^m(x_{m+1})N^{m+1}(x_{m+1})}{D^{m+1}(x_{m+1})}\right]\Bigg) \tag{2.25}$$

Here, the non-adiabatic part in the gyrokinetic moment equation is neglected, as well as polarisation in the quasi neutrality equation. Version of this equation where these effects, including FOW effects are consistely kept are availabe in [50, 51]

$$x_m=\frac{\omega}{k_{\parallel,m}v_{th}},\quad v_{thi}^2=\frac{2T_i}{m_i},\quad \omega_{p*}=\omega_{*n}+\omega_{*T}=\frac{T_i}{eB}k_\theta\left(\frac{\nabla n}{n}\right)(1+\eta)$$

$$\eta=\frac{\nabla T}{T}\Big/\frac{\nabla n}{n},\quad D(x_m)=\Big[1+\tilde{D}(x_{e,m})\Big]+\tau\Big[1+\tilde{D}(x_{i,m})\Big],$$

$$N^m(x_m)=\tilde{N}^m(x_{i,m})-\tilde{N}^m(x_{e,m}),$$

$$\tilde{D}(x)=(1-\frac{\omega_*}{\omega})xZ(x)-\frac{\omega_*}{\omega}\eta(x^2+xZ(x)(x^2-\frac{1}{2})),$$

$$2\tilde{N}^m(x)=(1-\frac{\omega_*}{\omega})\left[x^2+xZ(x)(x^2+\frac{1}{2})\right]-\frac{\omega_*}{\omega}\eta\left[x^4+\frac{x^2}{2}\right]+xZ(x)\left(\frac{1}{4}+x^4\right),$$

$$H(x_m)=\tilde{H}(x_{m,i})+\tau\tilde{H}(x_{m,e}),$$

$$\tilde{H}(x_m)=\frac{1}{2}\left[(1-\frac{\omega_*}{\omega})\tilde{F}(x_m)-\eta\frac{\omega_*}{\omega}\tilde{G}(x_m)\right],$$

$$2\tilde{F}(x)=xZ(x)\left(\frac{1}{2}+x^2+x^4\right),$$

$$2\tilde{G}(x)=xZ(x)\left(\frac{3}{4}+x^2+x^4+x^6\right)+2x^2+x^4+x^6,$$

$Z(x)$ represents the plasma dispersion function.

Some simplifications which are valid throughout the thesis are:

1. fast-circulating approximation is used, trapped particles are not included
2. isotropic Maxwellian distributions are used for all species
3. Finite-orbit-width (FOW) effects are not included consistently, but using a sim-

plifed Bessel operator $J_0 * (k_\perp \varrho_{orbit})$ where ϱ_{orbit} is orbit width of circulating effective thermal particle orbits.

3 Numerical Tools and Codes

In this chapter, we will discuss the workflow and the codes that are used throughout this paper to tackle different physics problems regarding AEs in general and Toroidal Alfvén Eigenmodes (TAEs) in particular inside a tokamak plasma. With the help of the workflow, we will be able to perform a linear stability analysis on different time slices of a simulated scenario or reconstructed experimental equilbiria. This will allow us to study the effect of different physical processes on the linear stability of TAEs and to compare the results with experimental data. The integrated workflow not only streamlines the linear stability analysis over an entire discharge, but also opens up new avenues for understanding complex plasma phenomena. In particular, it enables investigations into:

- **Compare MHD and gyrokinetic models within the same framework:** this includes combining kinetic resonance such as resonant EP drive and ion and electron Landau damping and radiative damping, Finite Larmor Radius (FLR) effects, diagmangetic corrections, and describe physics that goes beyond MHD models.
- **Non-Diffusive and Anomalous Transport:** Capturing phase-space zonal structures and resonant transport mechanisms that go beyond classical radial diffusion, thereby revealing novel features of EPs transport.

These studies contribute to a deeper understanding of energy transport, turbulence, and stability in fusion plasmas, effectively bridging the gap between theoretical models and experimental observations.

3.1 Numerical Tools

The aim of the workflow (WF) is to perform an automated linear stability analysis on different time slices of a simulated scenario or reconstructed experimental equilibrium. This is achieved by connecting various numerical tools with the data infrastructure (IMAS), facilitating the retrieval/saving of data from/to the database (DB) through a series of IDS files and fast configuration of numerical tools via XML files. As described

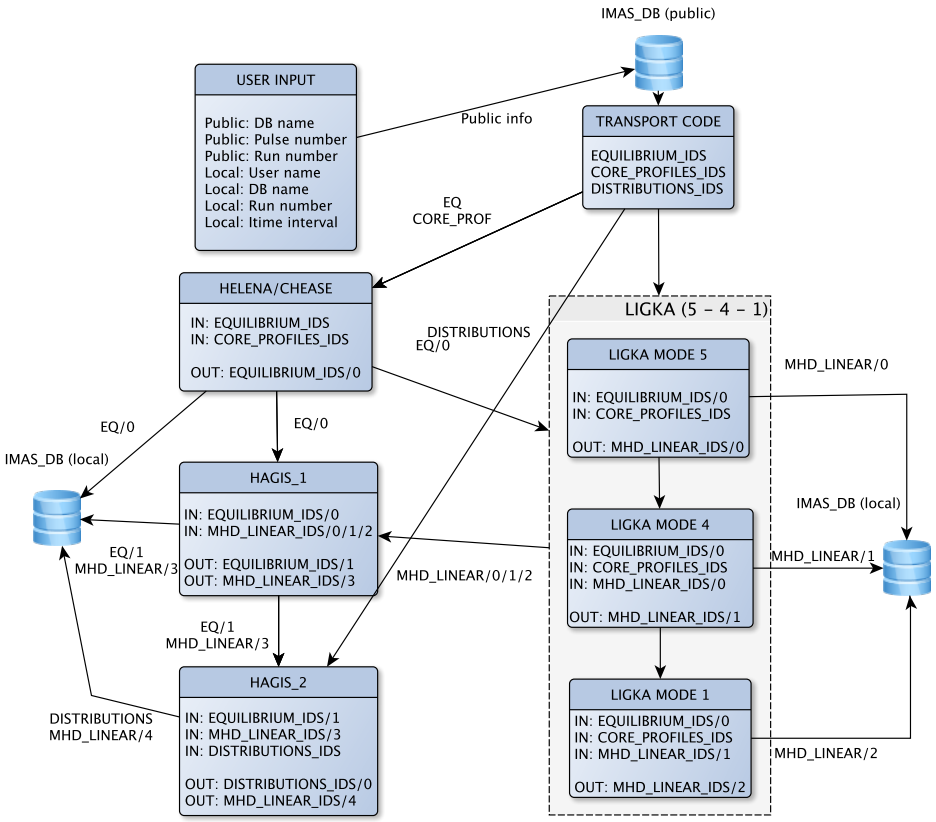

Figure 3.1: General layout of codes inside the IMAS-compliant EP-WF.

in ref. [23] IMAS relies on IDSs (integrated data structures) that combine a set of well-defined physical quantities into the complete description of a complex physical object such as an equilibrium or the linear stability information related to this equilibrium. Occurrences are the instances of the same IDS in the DB, these are generally used by the codes to store the results in a hierarchical manner. In Fig 3.1 one can see how the IDSs are being passed throughout the workflow between the codes and the DB. The inputs and outputs of each actor are well defined in terms of IDSs and the static configuration parameters that define the respective simulation are given in XML.

In addition to the non-GUI version (used by experimented/familiar users), in order to facilitate the interaction with the code and the underlying infrastructure, a graphical user interface (GUI) is also available (Fig. 3.2), this is made possible by the standardization of code-specific parameters in XML files.

The GUI is implemented in Python using tkinter and provides several key functionalities:

1. **Workflow Configuration**: The left panel allows setting core workflow param-

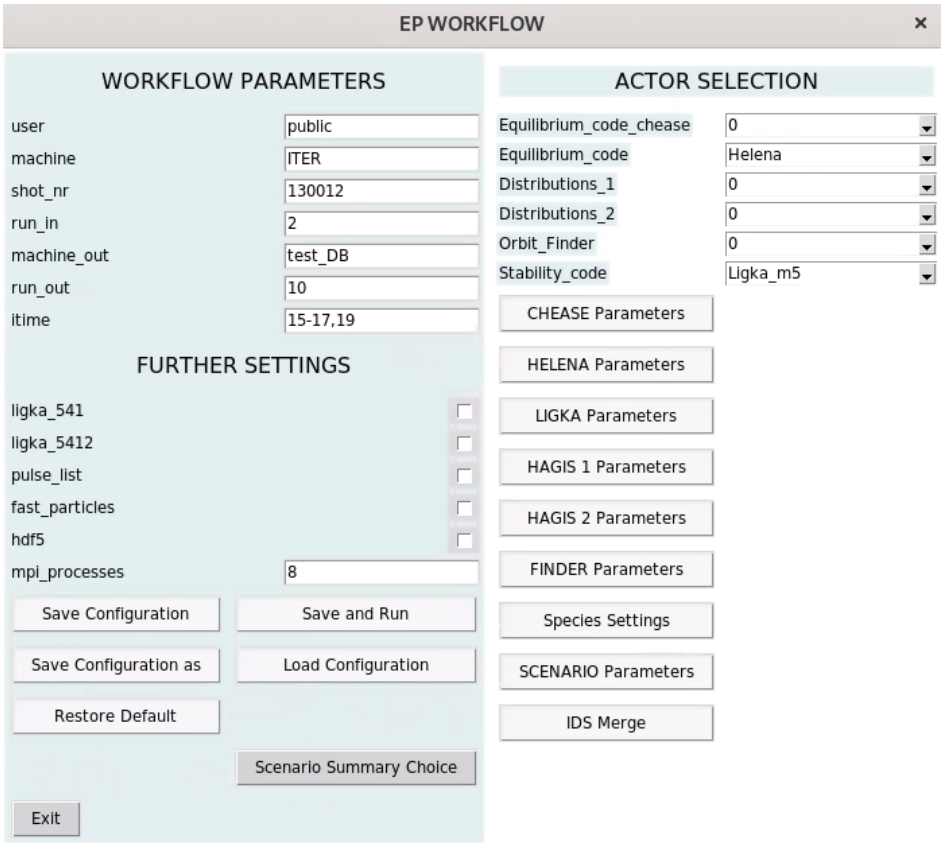

Figure 3.2: Graphical User Interface (GUI) of the IMAS-compliant EP-WF.

eters such as shot numbers, run identifiers, and execution options. Users can specify whether to use fast particles, enable HDF5 backend, or run specific LIGKA model combinations (e.g., models 5-4-1 or 5-4-1-2). Model numbers are directly linked to the LIGKA computational model hierarchy. For more details see 3.2.1.

2. **Actor Selection**: The right panel provides a hierarchical selection of physics actors to be included in the workflow, such as:
   - Equilibrium codes (CHEASE or HELENA)
   - Stability analysis code (LIGKA with various models)
   - Non-linear wave-particle interaction (HAGIS 1 and 2)
   - Orbit finding tools (FINDER), now called Orbit_Finder
3. **Parameter Configuration**: Each actor has its own parameter configuration window accessible through dedicated buttons. This allows fine-tuning of:

- CHEASE equilibrium calculation parameters
- HELENA coordinate transformation settings
- LIGKA model-specific parameters for stability analysis
- HAGIS settings for non-linear runs evolution
- Orbit_Finder parameters for orbit calculations

4. **Species Management**: A dedicated interface for configuring plasma species and their properties, including:
   - Thermal species density thresholds (including impurities)
   - Fast particle species settings
   - Automatic detection and configuration of species from core_profiles IDS
5. **Configuration Management**: The GUI provides functionality to:
   - Save and load workflow configurations
   - Restore default settings
   - Export configurations to XML files
   - Run the workflow with current settings

The GUI significantly simplifies the workflow setup by providing visual access to all configuration parameters while maintaining the flexibility of the underlying XML-based configuration system. It automatically handles the creation and modification of necessary XML files, manages IDS occurrences, and ensures proper parameter propagation between different workflow components.

A key feature is the automatic species handling - the GUI can analyze the core_profiles IDS to detect present species and configure LIGKA accordingly. This includes proper handling of thermal and fast particle populations, with density thresholds determining which species are included in the stability calculations. The interface also supports scenario modifications, allowing users to adjust density and temperature profiles for parameter scans.

Fig 3.1 explains how the individual actors are combined on a conceptual and technical level:

1. Take the equilibrium_ids from the transport code (given by ASTRA, METIS, DINA-JINTRAC or IDA(integrated data analysis) [52]) and pass it to HELENA or CHEASE [25] to perform high-resolution MHD equilibrium calculations. HELENA is used in the workflow as a coordinate transformation tool as LIGKA requires a certain representation of the equilibrium: straight field line coordinates, metric

tensor representation, and mapping to the R-Z grid. As output, they will produce another equilibrium_ids/0. From here on, with */0 meaning occurrence 0, one can have several instances of the same IDS in one workflow/database.

2. Together with equilibrium_ids/0, core_profiles_ids is being taken from the transport code or IDA and given as inputs for the simplest analyical model of LIGKA (model 5 see next section). Analytical estimates of TAE (and other AEs such as e.g. BAEs, EAEs, RSAEs, as explained later in the LIGKA model) are performed and then created as an output mhd_linear_ids/0 which in turn is saved in the local database.

3. Based on this result from the analytical model, the next model of LIGKA hierarchy can be run. The local model (model 4) returns a local estimate of the linear AE properties, i.e. it solves the local kinetic dispersion relation, using the approximations described in detail in the following papers [10, 43, 49]. As input, it uses equilibrium_ids/0, core_profiles_ids/0 and mhd_linear_ids/0 written previously by model 5 and creates a new occurrence of the mhd_linear_ids/1.

4. Finally, the standard (and refined) global solver can be started (models 1 and 2). As necessary input IDSs, we have equilibrium_ids/0, core_profiles_ids/0 and mhd_linear_ids/1 (output from model 4). Again, it creates a new occurrence of mhd_linear_ids/2 or mhd_linear_ids/6.

This workflow is not only driven by the need to analyze the stability problem with different levels of complexity and speed that is reflected by the different LIGKA models but also, each LIGKA model profits from the results of the previously run model: the local dispersion relation solver (model 4) needs a good starting guess for the complex contour integration in the frequency plane that is provided by the analytical estimate (model 5). The global solver (model 1/2) in turn uses model 4 results to set up an efficient 'antenna' scan based on the knowledge of the kinetic continuum structure. Consistent mapping of the results of each model into the DB allows us to construct a consistent hierarchy of results and eventually perform uncertainty quantification for each model. The modular setting and the usage of standard IMAS data structures also facilitates the usage of various other codes than LIGKA under the same umbrella in the future. LIGKA models could be replaced by other codes that perform different computations but arrive at the same physics result or, more specifically, a sufficiently populated data structure (mhd_linear) that can be used as input for the next model hierarchy (i.e the output of replacing code includes everything necessary to run the next LIGKA model).

In practice, the analytical (model 5) and local solvers (model 4) are used to obtain a fast overview of the scenario before attempting global, more expensive runs. The

global solver (model 1 and later 2) can then be used to validate - and in most cases - to improve the results obtained by the local runs.

The workflow's parallelization strategy is primarily focused on the computationally intensive global LIGKA models (1 and 2), which utilize parallel MUMPS solver for distributed memory computations. While direct parallelization across time slices would be desirable (under discussion), the hierarchical nature of the LIGKA models prevents this approach (without significant changes to the code) results from simpler models (5 and 4) are required as input for the global calculations at each time step. Instead, the parallelization is implemented at the linear solver level, where the large sparse matrices arising from the global models are distributed across multiple processes.

The workflow manages the parallel execution through a job scheduling system, ensuring proper resource allocation and load balancing across the available computational nodes. While the analytical (model 5) and local (model 4) calculations remain serial due to their relatively low computational cost, the parallel implementation of the global models has proven essential for maintaining reasonable times in various scenarios.

3.2 Codes

3.2.1 LIGKA

Central to the workflow, the LIGKA [27] actor operates by solving a set of linear gyrokinetic equations derived from the nonlinear gyrokinetic Lagrangian, which includes the quasi-neutrality equation, the gyrokinetic moment equation, and the perturbed distribution function equation (see chapter 2.1.7). The design of the model emphasizes the incorporation of finite Larmor radius (FLR) effects [51], ensuring that the dynamics of both circulating and trapped particles in the presence of MHD modes are accurately captured.

Workflow Overview:

1. **Model Initialization**: The LIGKA model begins by initializing the plasma equilibrium. This setup defines the magnetic and plasma parameters essential for the simulation, including magnetic field configuration, temperature, density profiles, and the pressure of fast ions. The model supports input from analytical profiles and numerical equilibria, enabling flexibility to study various plasma conditions.

2. **Fourier Decomposition and Finite Element Discretization**: The model uses Fourier decomposition for toroidal and poloidal components and finite element discretization in the radial direction. This setup allows LIGKA to resolve

the intricate spatial dependencies of the perturbations, particularly in toroidal geometry. By discretizing the problem, the model can solve for eigenvalues, which represent the growth or damping rates of the modes and their global mode structures.

3. **Orbit Integration with HAGIS**: One of the key features of LIGKA is its ability to handle orbit integration for fast particles. The HAGIS code is optionally employed to accurately describe the particle orbits, ensuring that both circulating and trapped particles are taken into account. This step can be crucial if analytical orbits width effects are not well approximated by the fast, circulating approximation adopted widely in the analytical literature [44, 49–51]. That means that for distribution functions that are dominated by trapped ions, this accurate numerical integration is needed to obtain accurate results, although overall trends (e.g. with β_{EP})are typically well recovered. In this work, for simplicity the fast circulaing partcle approximation was used in all local and global simulations as detailed distribution functions with trapped particles were not available in IDS format so far.

4. **Eigenvalue Problem Formulation and Solution**: The linear gyrokinetic equations are formulated as an eigenvalue problem, which is solved iteratively (inverse vector iteration) or with an numerical antenna ansatz [10]. The eigenvalues represent the mode growth rates or damping rates, indicating whether specific MHD modes are stable or unstable under the influence of fast particles.

5. **Verification and Validation**: Verification is an essential part of the workflow to ensure that the results align with theoretical predictions and experimental observations. Looking at the whole model hierarchy also provides insights into the range of applicability of the model and highlights any limitations under specific plasma conditions.

6. **Analysis and Interpretation**: Analyzing the dependence of the linear results (i.e. mode frequency, growth/damping rate, global mode structure) from the underlying equilibria, profiles and EP distributions delivers the basis for determining the related EP transport. Based on these linear quantities, e.g. using quasi-linear theory [21] or more general transport theories [22] the EP transport can be predicted.

By solving the linearized gyrokinetic equations, LIGKA outputs eigenvalues and eigenfunctions such as frequency, damping and mode structures (electrostatic and electromagnetic components, and derived from that also the parallel electric field). Models of LIGKA used in this work are:

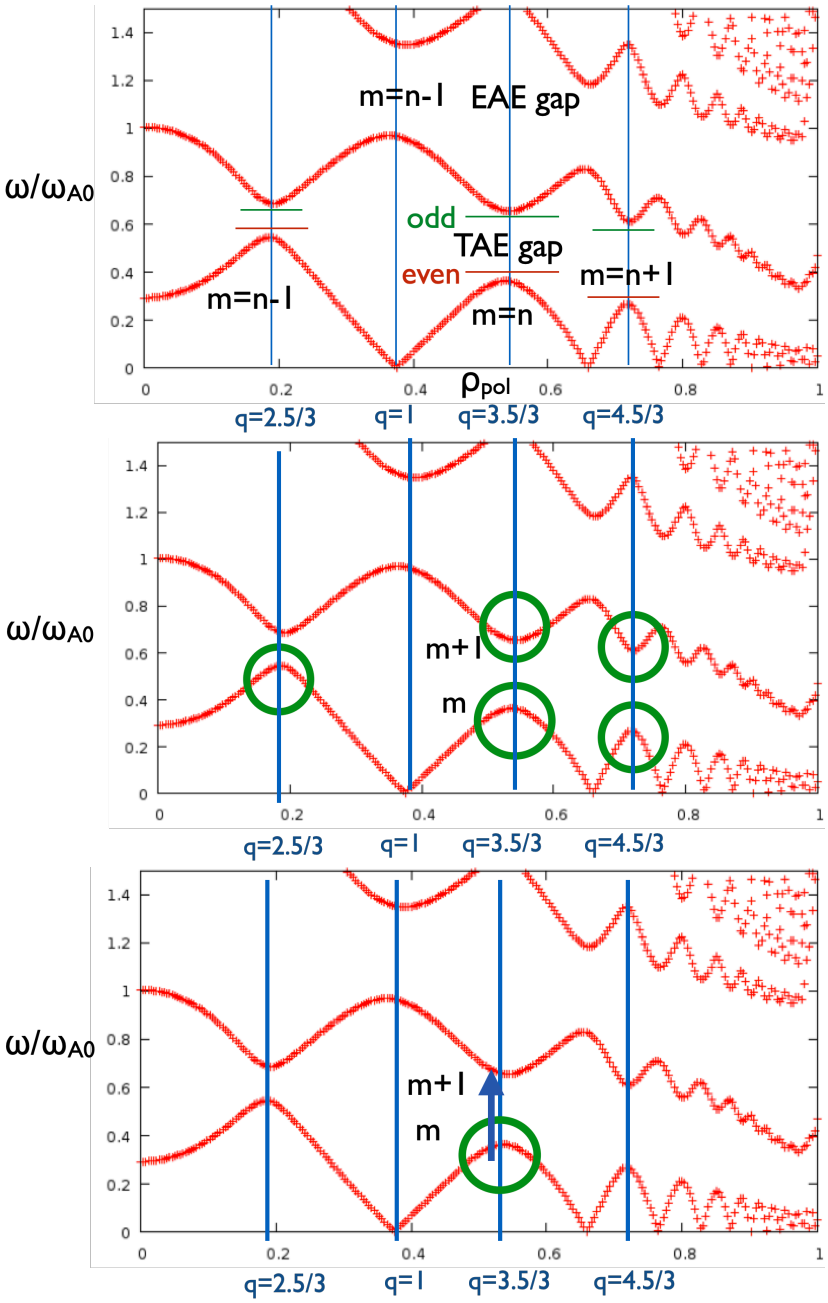

Figure 3.3: From top to bottom (model 5/4/1) model explanation. Model 5 (top) provides an analytical estimate of the AE properties, model 4 (middle) provides a local estimate of the AE properties by determining the complex frequency of the maximum or minimum of the continuum closest to the AE's rational surface, and model 1 (bottom) provides a global estimate of the AE properties by performing a frequency scan throughout the gap or close to the local extremum.

1. (1 second/mode) Model 5: local analytical estimates of various AEs properties: frequency, estimated mode structure, rational surface, radiative damping, next and previous gap information based on the analytical formulae of ref. [47, 53] (in the event that we are dealing with AEs related to gaps in the shear Alfvén continuum).

2. (10 seconds/mode) Model 4: based on model 5 results, the local analytical dispersion relation for one AE (n,m-pair) is calculated. The output is the complex frequency of the maximum or minimum of the continuum closest to the AE's rational surface (see Fig.3.3 (middle)), giving a good estimate for ion LD (Landau Damping) and local electron LD. This model determines the starting point for global calculations.

3. (2-5 minutes/mode) Model 1: based on the results of model 4 (or 3), a frequency scan is performed throughout the gap or close to the local extremum (BAE, RSAE) in order to find linear properties of AEs, i.e. the location of the global AE in the gap (see Fig.3.3(last)). The antenna version is based on a damped harmonic oscillator model which searches for the maximum in response and phase jump to determine frequency and damping. Sometimes, several AEs can be found in a gap. LIGKA stores them as separate modes. The runtime of the model depends critically on the radial resolution (nr) and the number of poloidal Fourier harmonics (m) needed, as the size of the matrix to be inverted at each step scales with $(nr \times m)^2$. The sparse matrix is solved with a parallel MUMPS [54] solver (distributed memory).

4. (2-5 minutes/mode) Model 2: performs finer steps in the frequency scan around the AE's frequency as determined by model 1. It is especially necessary when the damping / growth rates are marginal.

5. (1-10 minutes/mode) Model 6/3: reduced MHD/kinetic spectrum. The details of the kinetic dispersion relation, solution methods and benchmarks can be found in previous papers [43, 49].

In this thesis, we focus exclusively on TAEs, although also other types of AEs such as RSAEs (reversed shear AEs), BAEs (beta-induced AEs) and EAEs (ellipticity induces AEs) are implemented and were validated in elsewhere (Ph. Lauber unpublished 2024). This workflow is also equipped with interfaces to work with other numerical tools such as HAGIS [55] that can provide numerically calculated orbit integrals for all types of EPs (not used in this work for simplicity). Moreover, the work has been connected to the ATEP [29] code via IMAS/IDS interfaces and it serves as input for the transport code.

3.2.2 CHEASE

The CHEASE code is used to compute magnetohydrodynamic (MHD) equilibria for tokamak plasmas by solving the Grad-Shafranov equation, with applications in stability and wave propagation analysis. It employs a variational formulation and discretizes the equation using bicubic Hermite finite elements, which allow high-accuracy solutions with continuous first derivatives, essential for stability calculations. CHEASE is more flexible with respect to input profiles such as: current, q-profile, pressure, not just TT' and p'. Also it deals better with current hole equilibria. Note that due to different axis boundary conditions the results between HELENA and CHEASE may differ slightly.

CHEASE solves the Grad-Shafranov equation, a second-order nonlinear partial differential equation that describes the balance between plasma pressure, magnetic fields, and current density in a toroidal geometry. This formulation requires the definition of pressure and current profiles, which can be obtained either from analytical expressions or directly from experimental data. The code then discretizes the poloidal flux function using bicubic Hermite finite elements on a grid that is mapped to a rectangular coordinate system, a strategy that guarantees smooth gradients and an accurate representation of the magnetic flux surfaces—essential for resolving the detailed structure of the plasma equilibrium. Given the nonlinear nature of the Grad-Shafranov equation, CHEASE employs an iterative solution process using the Picard method, adjusting the magnetic flux and pressure profiles until the solution converges to a self-consistent equilibrium. Following convergence, the computed equilibrium is mapped and scaled into flux coordinates, a transformation that is necessary for compatibility with stability and wave propagation codes such as LIGKA and HAGIS. Additionally, CHEASE features an automatic adjustment of the pressure profile to meet stability criteria, generating equilibria that are marginally stable to ballooning modes or that exhibit specified bootstrap current profiles—an important capability for advanced tokamak scenarios where pressure-driven instabilities must be controlled. Finally, the equilibrium data, including safety factors, current density, and pressure gradients, is output in a format tailored for subsequent stability and transport analyses, ensuring that further studies accurately reflect the underlying plasma state.

In the workflow we first use CHEASE (more robust and flexible) and then HELENA as a high resolution coordinate transform tool from low resolution experimental/transport code equilibria.

3.2.3 HELENA

The HELENA code used within the workflow context of fusion plasma modeling, plays a critical role in generating accurate magnetohydrodynamic (MHD) equilibrium profiles,

which serve as foundational input for various stability and transport analyses, including those used in the LIGKA model. HELENA is specifically designed to solve the Grad-Shafranov equation for axisymmetric plasma configurations, enabling it to provide equilibrium solutions such as the magnetic field structure. In general 2d geometry by supplying the poloidal shape of the last closed flux surface.

Similar to CHEASE, the process begins by solving the Grad-Shafranov equation, which characterizes the equilibrium of a tokamak plasma by balancing magnetic pressure, plasma pressure, and the poloidal magnetic field within an axisymmetric geometry. This equation is derived from the plasma parameters, including the poloidal and toroidal magnetic fields and the radial pressure profile. To solve the equation numerically, HELENA employs a finite element method using isoparametric bicubic Hermite elements; this approach enables a highly accurate representation of the spatial variations in the magnetic flux surfaces, resulting in smooth and continuous equilibrium solutions. Because the Grad-Shafranov equation is inherently nonlinear, an iterative solver is used to adjust the magnetic flux and pressure distributions until a self-consistent equilibrium is achieved, thereby defining the magnetic surfaces that are critical for subsequent stability and kinetic analyses. Finally, the equilibrium data, such as magnetic flux surfaces and current density profiles produced by HELENA serve as essential inputs for various stability and transport analysis codes, including LIGKA.

With the introduction of CHEASE in the workflow, HELENA uses the converged CHEASE equilibrium data to recalculate the high resolution equilibria in straight field line coordinates needed by LIGKA.

3.2.4 HAGIS

The HAGIS code suite, consisting of HAGIS 1 and HAGIS 2, plays a pivotal role in analyzing the interaction between fast particles and Alfvén waves in tokamaks. It provides a framework for studying both linear and nonlinear dynamics of energetic particles under resonant wave-particle interactions, especially for AE type modes but also global MHD instabilities such as kinks, fishbones and neoclassical teraing modes [56]. HAGIS is also used as a tool to investigate the neoclassical transport of thermal ions close to the plasma edge [57]. Each version serves distinct purposes within a comprehensive workflow that supports various other codes like LIGKA or ATEP.

In the workflow, the HAGIS 1 code is used to transform equilibrium and LIKGA mode structures to Boozer coordinates, for then to be passed to the Orbit_Finder actor (described in the next subchapter), which calls HAGIS 2 iteratively.

HAGIS 1 starts by loading the MHD equilibrium, typically sourced from equilibrium codes like HELENA or CHEASE, defining the magnetic field configuration and plasma parameters. It also transforms the linear eigenfucntons as caluclated with LIGKA to

Boozer coondiates.

LIGKA-HAGIS can be run in different levels of complexity, i.e. it can be stopped in the linear phase, or by using a non-linear wave-particle interaction Lagrangian to calculate the non-linear relaxation of EP distributions.

Linear phase of HAGIS 2:

1. **Guiding Center Orbit Calculation**: Employs a guiding center approach to calculate particle orbits in the tokamak's magnetic field. This approach simplifies the computation by averaging over the rapid gyromotion of particles, allowing the code to focus on the drift orbits, which are typically sufficient for interactions with low frequency Alfvén waves.

2. **Linear Wave-Particle Interaction**: Using a perturbative method, HAGIS-2 calculates the linear response of the energetic particle population to MHD perturbations. The code assesses growth or damping rates of the modes by evaluating the resonant wave-particle interaction. It identifies the contribution of fast particles to the stability of Alfvén eigenmodes, essential for understanding whether certain plasma conditions can lead to TAE instabilities.

Nonlinear Evolution and Wave Saturation:

1. **Nonlinear Wave-Particle Interaction**: This allows the study of mode saturation effects caused by energetic particles. The code tracks the evolution of particle distributions in phase space, accounting for modifications induced by resonant interactions. This is done by evaluating the wave particle interaction Lagrangian [55].

2. **δf Method for Computational Efficiency**: Uses the δf method, which focuses on simulating changes in the fast particle distribution rather than the entire ensemble. This technique reduces computational load and improves accuracy, particularly for cases where only a small fraction of particles drive the instability.

3. **Self-Consistent Mode Evolution**: The feedback from particle dynamics on the Alfvén wave amplitude and phase is computed self-consistently. This captures mode saturation, frequency chirping, and other nonlinear effects that can lead to particle redistribution and even particle loss. By monitoring changes in wave amplitude, HAGIS-2 provides insights into energy transfer from particles to waves.

4. **Output for Diagnostic and Mitigation Studies**: Produces detailed data on wave evolution and fast particle redistribution, supporting studies on confinement and diagnostic strategies (e.g. a synthetic fast ion loss detector [58]). The output data can be used to design plasma scenarios that minimize energetic particle losses, which is crucial for sustaining ignition in future fusion reactors like ITER.

3.2.5 Orbit Finder

It is a multi-purpose wrapper for HAGIS2, i.e. calls HAGIS2 iteratively for various purposes:

1. calculating orbit information and linear propagator integrals along the orbits to be used on LIGKA (see above);
2. calculating EP fluxes in the presence of prescribed set of perturbations;
3. calculate energy transfer between particle and wave;
4. calculate orbit-averaged neocalssical collision coefficients [59] to be used in the ATEP-3D code.

3.2.6 ATEP

The Advanced Transport for Energetic Particles (ATEP)[29] code is a reduced model for simulating phase-space-resolved energetic particle (EP) transport in fusion plasmas. ATEP is designed to capture meso-scale EP dynamics beyond conventional diffusive transport approximations. It employs a first-principles-based framework utilizing nonlinear gyrokinetic equations, directly evolving EP fluxes in constants-of-motion (CoM) space rather than assuming a diffusive model a priori. The code integrates with the IMAS (Integrated Modelling and Analysis Suite) framework and leverages the EP-Stability workflow, utilizing existing gyrokinetic and transport codes such as HAGIS and LIGKA for phase-space flux calculations.

ATEP models EP transport using a continuity equation in CoM space (P_ϕ, E, Λ), where P_ϕ is the canonical toroidal momentum, E the energy, and $\Lambda = \mu \frac{B_0}{E}$ the adiabatic invariant:

$$\frac{\partial F_z}{\partial t} = -\frac{\partial}{\partial P_\phi}\left(\langle dP_\phi/dt\rangle F_z\right) - \frac{\partial}{\partial E}\left(\langle dE/dt\rangle F_z\right). \tag{3.1}$$

Here, the fluxes $\langle dP_\phi/dt\rangle$ and $\langle dE/dt\rangle$ are obtained from HAGIS simulations (by using the Orbit-Finder as wrapper), which model interactions with Alfvén eigenmodes. Unlike conventional diffusion-based models, ATEP self-consistently evolves these fluxes without enforcing an artificial transport mechanism. In the constant-amplitude limit, the advection velocity fields $v_{P_\phi,E}$ are treated as externally prescribed inputs from experimental data, gyrokinetic simulations, or reduced models.

In its presently implemented quasi-linear limit transport formulation, ATEP includes an energy balance equation coupling wave amplitudes and EP distribution functions:

$$\frac{d}{dt}\left(E + \sum_k W_k\right) = -2\sum_k \gamma_{d,k} W_k, \tag{3.2}$$

where W_k denotes wave energy and $\gamma_{d,k}$ the damping rates derived from LIGKA stability analyses.

ATEP is embedded in the IMAS EP-Stability workflow and is fully compatible with its IDS-based data structure, allowing seamless integration with transport solvers and experimental data. The implementation consists of the following steps:

1. **Grid Generation**: A structured CoM-space grid is generated using the **Orbit-Finder** tool, which maps trapped, passing, and stagnation orbits.

2. **Transport Coefficient Calculation**: Using HAGIS, the orbit-averaged transport fluxes $\langle dP_\phi/dt \rangle$ and $\langle dE/dt \rangle$ are computed for a range of perturbation amplitudes.

3. **Interpolation and Projection**: A multi-dimensional spline interpolation reconstructs the transport fields on a uniform CoM grid.

4. **Transport Solver**: The transport equation is numerically solved using Lax-Wendroff and Crank-Nicholson schemes, ensuring numerical stability over long ITER-relevant timescales.

ATEP has been applied to study neutral beam-driven EP transport in ITER pre-fusion plasmas with Toroidal Alfvén Eigenmodes (TAEs). The transport model successfully reproduces radial diffusion profiles, capturing the interplay between EP distribution gradients and wave-particle interactions. The model is currently being extended to include collisions and neoclassical transport, paving the way for a comprehensive 3D EP transport framework [29].

Unlike standard transport solvers based on radial diffusion coefficients, ATEP directly models non-diffusive transport phenomena, including phase-space zonal structures and resonant transport mechanisms. In this respect, it shares similarities with the HAGIS model but extends its scope by incorporating fully self-consistent flux evolution. The integration with LIGKA ensures consistency with linear stability calculations, while compatibility with IMAS IDS structures allows for automated scenario analysis, similar to CHEASE, HELENA, and LIGKA in the EP-Stability workflow.

In summary, the actors integrate into a workflow that spans from linear stability assessment to nonlinear wave evolution, offering a comprehensive toolkit for exploring the impact of energetic particle interactions with Alfvén waves. This dual-stage analysis provides essential data on mode stability and particle dynamics, guiding both theoretical understanding and experimental design in tokamak research.

3.3 From experimental data to simulation input

The EP stability workflow is built around several key functions that handle different aspects of the physics calculations and code execution. Here we examine the main functions that coordinate the workflow operation. Additionally, robust data provenance is embedded throughout the workflow, which is crucial because simulation data is often too complex for traditional scanning methods to fully capture the intricate physics scalings. By meticulously tracking data origins and transformations, the workflow not only ensures traceability and reproducibility but also provides the necessary context to interpret complex simulation outcomes reliably.

3.3.1 Workflow side functions

Workflow Control Function

The `workflow_EP` function serves as the main control function for the entire workflow. It handles:

- Loading and parsing of input parameters from XML configuration files
- Management of database connections and output directories
- Orchestration of actor execution sequences
- Support for batch processing multiple shots/runs

The function first imports parameters from the workflow XML files:

```
# Import workflow parameters from XML configuration files
param = parameters_workflow(
    current_config_folder + "/input_workflow_default.xml"
)
species_input = parameters_workflow(
    current_config_folder + "/actor_settings.xml"
)
scenario_params = parameters_workflow(
    current_config_folder + "/scenario.xml"
)
```

It then creates necessary output directories and handles either single or multiple pulse execution based on configuration.

Actor Management

The `actor_settings` function configures the execution parameters for each physics code actor. To do this, the function defines:

- Input/output IDS occurrences
- Actor wrapper functions
- Configuration file paths
- Actor execution flags

For example, for the LIGKA mode 5 actor:

```
# Configure LIGKA mode 5 actor parameters
actor_params["entrypoint_actor"] = False
actor_params["wrapper"] = ligka_actor_wf_wrapper
actor_params["config_file_name"] = "z_ligka.xml"

# Define input and output IDS configurations
input_ids = {
    "equilibrium": 0,
    "core_profiles": 0,
    "mhd_linear": 0,
    "distributions": 0,
    "distributions": 1,
}
output_ids = {"mhd_linear": 5}
```

Actor Execution

The `actor_call` function handles the execution of individual physics actors:

- Validates actor availability
- Manages input/output IDS connections
- Handles time slice iterations
- Coordinates MPI execution where needed

The function processes input IDS data:

```
# Get input equilibrium slice at specified time
equilibrium_in = input.get_slice(
    ids_name,
    time[itime],
    imas.imasdef.PREVIOUS_SAMPLE,
    occurrence=ids_occ,
)
```

And manages actor execution and output storage:

```
# Execute actor wrapper with input parameters
equilibrium_out, mhd_linear_out, core_profiles_out, \
    distributions_out = actor_params["wrapper"](
        equilibrium_in,
        core_profiles_in,
        mhd_linear_in,
        distributions_in_1,
        distributions_in_2,
        config_file,
        mpi_ranks=mpi_processes,
    )
```

Species Selection

The `select_species_by_density` function implements the physics-based selection of plasma species for stability calculations. This is done through:

- Analyzes core plasma profiles
- Applies density thresholds for species selection
- Handles both thermal and fast particle populations
- Supports hybrid species treatment (e.g. D-T)

Species are selected based on density thresholds:

```
# Check if species density exceeds threshold
if thermal_density_val >= density_cutoff.get(
    ligka_string, np.inf
) * total_ion_density:
    curr_str.append(ligka_string)
```

Scenario Modification

The `scenario_mod` function allows modification of plasma profiles based on scenario parameters by supporting:

- Density and temperature scaling
- D-T mixture ratio adjustment
- Profile shape modifications

For example, handling D-T scenarios:

```
# Modify D-T plasma profiles based on scenario parameters
if int(scenario_params["DT"]):
    if core_profiles_in.profiles_1d[0].ion[i].label == "D+":
        core_profiles_in.profiles_1d[0].ion[i].density *= \
            scenario_params["n_D"]
        core_profiles_in.profiles_1d[0].ion[i].temperature *= \
            scenario_params["T_D"]
```

These core functions work together to provide a flexible and physics-based workflow for EP stability analysis. The modular design allows for easy extension and modification of the workflow capabilities while maintaining robust handling of the underlying physics calculations. New actors are also easily added to the workflow by following the structure of the existing actors. For example the FALCON [60] can be used to determine the Alfvénicity parameter in the MHD limit also, which can replace the MHD spectrum model from LIGKA (model 6).

3.3.2 LIGKA side functions

Further tasks are needed to ensure consistency and reliability of the local and global solutions. Internal adjustments of LIGKA handle various tasks. Specific to the workflow and the discharges considered in this thesis, the following functions are relevant:

- In handling experimental discharges, as e,g. the JET dischrage discussed in chapter 5.4, given the large number of energetic particle species, quasineutrality has to be enforced by the code. This is done through keeping the electron densities fixed to the values present in the predictive scenario(METIS)/interpretative discharge(JET) profiles. Ion densities are then modified such that by adding EP species, thermal and EP ions fulfil quasi-neutrality, by reducing the density of the thermal species accordingly.

- Adjustments of numerical parameters are unavoidable for a code like LIGKA that comprises a large variety of hierarchical models, mode types and parameter ranges. Fine tuning of the computational models needed to be performed. Although all relevant parameters were tuned to match automatically the required ranges for a successful linear analysis, they can also be set manually to investigate unsuccessful runs or cases outside the usual regimes.

4 Scenario Description

For the purpose of demonstrating the capabilities of the newly developed workflow, three scenarios were chosen from the many available in the ITER-IMAS database. The scenarios analyzed in this paper are the baseline Deuterium-Tritium predictive ITER scenarios as generated by different transport codes. The transport data was obtained from running the ASTRA, METIS or DINA-JINTRAC workflows, transport packages that are available at ITER through the Integrated Modelling & Analysis Suite (IMAS). The workflow needs to be validated, next to AUG cases [not repported here Ph. Lauber private communication], a recent very successful JET discharge [61] is modelled. This has been used to validate the multi-species energetic particle part of the EP-WF that, being one of the new developments enabled a more riguorous and comprehensive physics interpretation of high-level physics results from JET in the view of ITER and DEMO. In ITER, it is essential to predict whether TAEs will be unstable, particularly during plasma ramp-up and ramp-down phases when conditions vary rapidly. Understanding both the drive mechanisms, such as those provided by fusion-born alpha particles and neutral beam injection (JET), and the damping processes is critical for accurate stability assessments. This analysis also aims to supply reliable linear input for energetic particle transport models, thereby enabling more precise predictions of fast-ion behavior and overall reactor performance.

In order to give a clear overview, this chapter is separated into four sub-chapters, each describing one scenario.

4.1 ITER 15 MA using ASTRA - 131025/34

This specific ASTRA-generated scenario is time-independent, i.e. only one time slice at 208s in the flat top phase has been exported into IMAS. ASTRA, similar to other transport codes, is a tokamak simulation tool based on 2D equilibria and a set of 1D diffusion equations for particle and heat transport [31]. For this particular scenario, a semi-empirical scaling law for the transport and a sawtooth mixing model were used. [62] In this scenario the plasma composition is a 50:50 Deuterium - Tritium mix.

The electron, deuterium and tritium profiles can be seen in Fig.4.1. Electrons have a temperature on the axis of $T_{e,0} \approx 23$ keV, and $T_{e,p} \approx 4$ keV at the top of the pedestal.

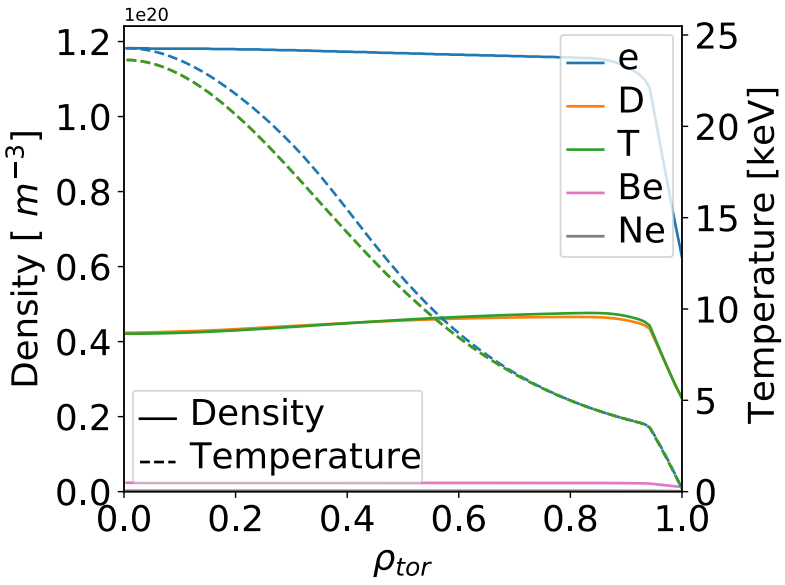

Figure 4.1: ASTRA scenario: density (solid) and temperature (dashed) for electrons (e), deuterium (D) and tritium (T) at $t = 208$s.

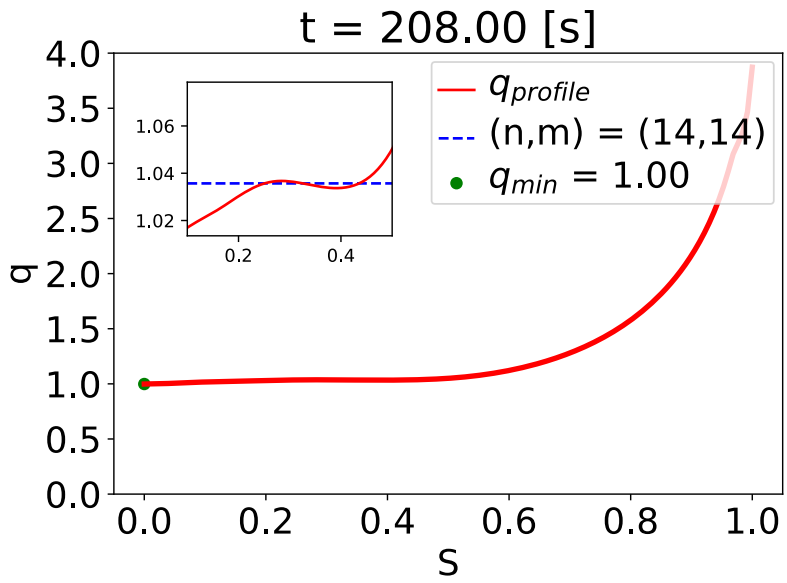

Figure 4.2: Safety factor profile at $t = 208$s. Zoom on the inner part of the tokamak (0.2 - 0.6) to observe that the q profile is not strictly monotonic. With a depiction of the minimum value of the profile (green). And the rational surface for $n = 14$, $m = (14, 15)$ TAE (blue).

For D and T, the on-axis temperature $T_{D/T,0} \approx 22$ keV with the temperatures at the pedestal the same as for electrons. We have an almost flat density profile for electrons with $n_{e,0} \approx 1.2 \times 10^{20}\ m^{-3}$. For the ion species considered in this scenario (D and T) the on-axis density is $n_{D/T,0} \approx 0.4 \times 10^{20}\ m^{-3}$. The profiles peak slightly in the pedestal region $n_{D/T,p} \approx 0.5 \times 10^{20}\ m^{-3}$ due to the presence of fast ions and helium ash in the core. However, since no information about the EP fractions of density and pressure is present in the output of the transport code, no fast particles were included in the analysis of this scenario. Instead, we will focus on the damping mechanisms.

In Fig. 4.2 the safety factor profile (with a zoom showing the values in the inner part of the tokamak and the minimum value of the profile) can be seen. $q_0 = 1.00$ in this case, meaning that in principle due to $q_{TAE} = (m + 0.5)/n$ all TAEs with $n \geq 1$ could be present. Also, the q-profile is not strictly increasing. This can lead to multiple TAE surfaces, as shown by the blue line that indicates $q_{TAE} = (14 + 0.5)/14 = 1.036$ for the (n,m) pair (14,14).

4.2 ITER 15 MA using DINA-JINTRAC - 134173/106

The second scenario taken into consideration is a time-dependent D-T scenario produced with the DINA-JINTRAC transport workflow. It assesses the entire scenario evolution from the early ramp-up phase (from X-point formation) until the late ramp-down phase (to X-point-limiter transition) by means of integrated simulations including core (1.5D), edge (2D), and SOL transport with time-dependent free-boundary plasma geometry and pedestal pressure determined by continuous self-consistent edge MHD stability analysis. Neoclassical transport is modeled with NCLASS [63] and turbulent transport is described by the L-mode version of the Bohm-gyroBohm model in L-mode [64] or by the GLF23 [65] model in H-mode [66].

In Fig.4.3 the fusion power peaks at 150s in the simulation and then slowly decays over the rest of the scenario. Unfortunately, at the time of writing this paper no fast particle information was available in the transport code output, and thus, no fast particles (EPs) were included in the analysis of this scenario.

In Fig.4.4 density and temperature for electrons and background ions are shown. The temperature profiles, with dashed lines, are as follows: $T_{e,0} \approx 26$ keV, $T_{e,p} \approx 6$ keV, $T_{D/T,0} \approx 16$ keV and $T_{D/T,p} \approx 5$ keV. The densities are: $n_{e,0} \approx 6.8 \times 10^{19}\ m^{-3}$ for electrons, $n_{D,0} \approx 3.2 \times 10^{19}\ m^{-3}$ for deuterium and $n_{T,0} \approx 2.8 \times 10^{19}\ m^{-3}$ for tritium.

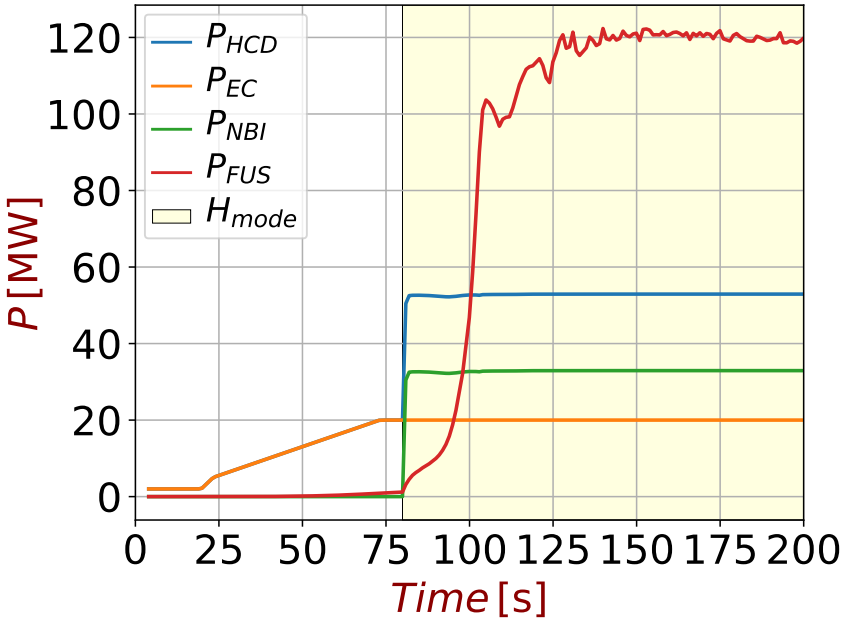

Figure 4.3: DINA-JINTRAC heating and fusion power evolution until 200s in the scenario.

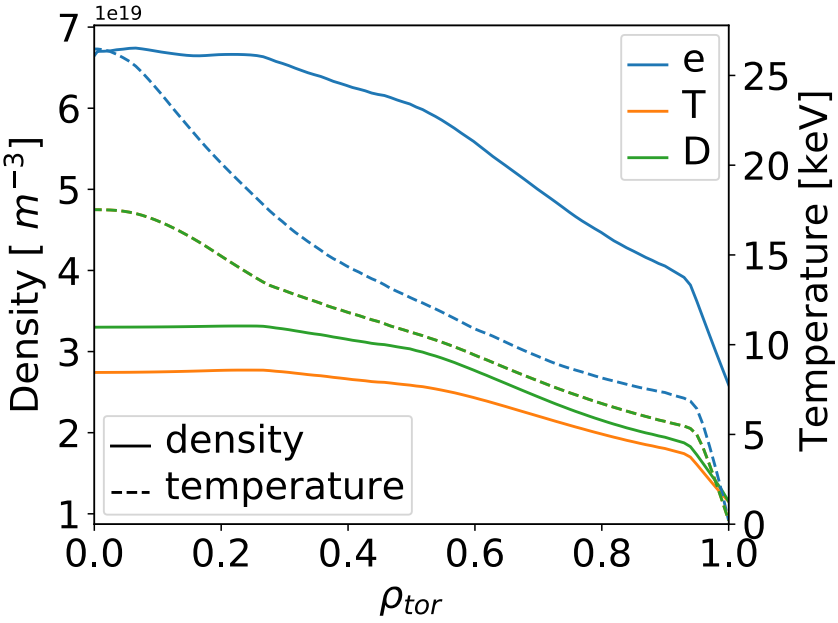

Figure 4.4: JINTRAC scenario density and temperature for electrons, deuterium and tritium at $t = 97.94$s.

4.3 ITER 15 MA using METIS - 130012/02

The third scenario is a time-dependent scenario generated by METIS. To achieve faster speeds (real-time and faster) the physics model in METIS is simplified with respect to the DINA-JINTRAC workflow. It combines 0D scaling-law normalized heat and particle transport modeled with 1D current diffusion modeling and 2D equilibria. The details are described in reference [32]. It is again a D-T plasma, the baseline ITER scenario for $Q = 10$, and thus, one of the most important scenarios for fusion at ITER.

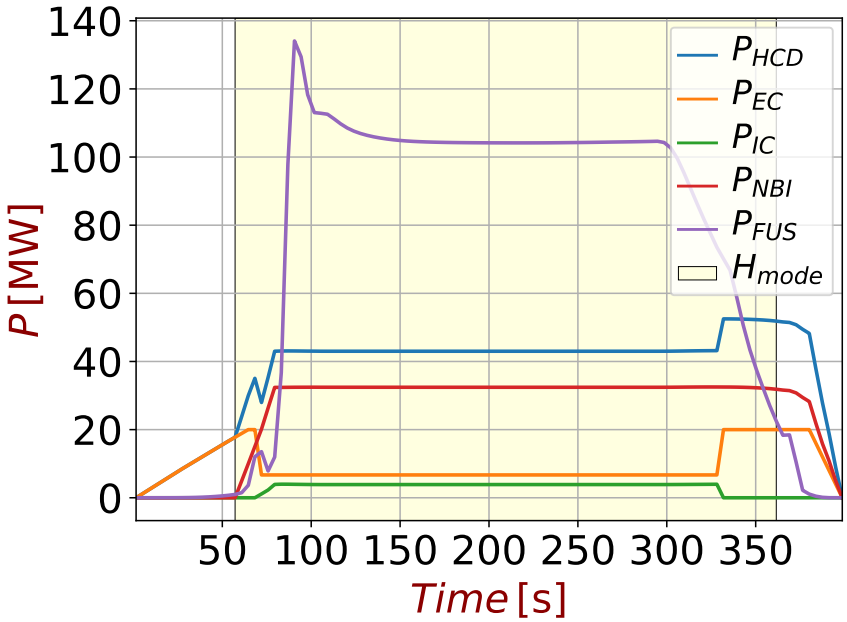

Figure 4.5: METIS scenario heating and fusion power evolution. Fusion Power peaks at 90s.

In Fig.4.5 the evolution of heating and fusion powers for the METIS scenario are shown. Of special interest for our study is the P_{FUS} (purple line). It peaks at approximately 90 s with $P_{FUS} \approx 130$ MW. This evolution allows us to test and validate the energetic particle part of the EP-WF.

Fig.4.6 shows, like before, the density and temperature profiles this time at $t \approx 90$s i.e. at the peak of P_{FUS}. For electrons, the temperatures on the axis and at the pedestal peak at $T_{e,0} \approx 27$ keV, and $T_{e,p} \approx 4$ keV. For background ions (D and T in this case) the temperature profile is the same with $T_{D/T,0} \approx 25$ keV at the axis, and the same as the electrons at the pedestal. The electron and background ions densities are mostly flat, peaking at $n_{e,0} \approx 1 \times 10^{20}\ m^{-3}$ for electrons and $n_{D/T,0} \approx 0.45 \times 10^{20}\ m^{-3}$ for background ions. In this scenario, we have alpha particles from the fusion

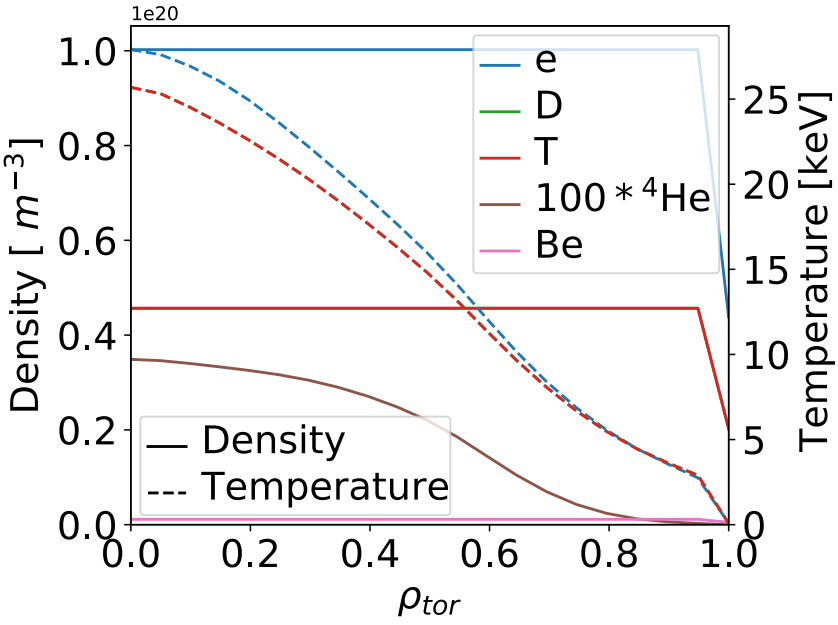

Figure 4.6: METIS scenario density and temperature for electrons, deuterium, tritium and alpha particles at $t = 90$s.

process. Their density is also shown in the same figure (100×), peaking on axis at $n_{He4,0} \approx 0.38 \times 10^{18}\ m^{-3}$.

In Fig.4.7 we have the safety profile at $t = 201.96$ s for this scenario and the minimum value of this profile is $q_{min} = 1.06$ depicted by a green dot in the figure. It should be noted that the q profiles in all ITER cases are constrained to stay close to $q = 1$ with a very flat shear. This is unfortunately not very realistic since either sawtooth crashes or flux-pumping effects may lead to a cycling relaxation of the central q-profile. This highlights again the importance of the workflow that will be able to deal with the equilibrium evolution. The JET case study will show the importance of this.

4.4 JET DT experiment - 99896/05

This case study focuses on the stability and confinement of deuterium-tritium (D-T) burning plasmas with minimal external torque, achieved mainly through ion cyclotron resonance frequency (ICRF) heating [61]. The scenario prioritizes not maximizing fusion power, but achieving a plasma state representative of future reactor conditions, with dominant electron heating, low toroidal rotation, and Alfvén wave instabilities present, which are critical for understanding the interactions expected in burning plasma

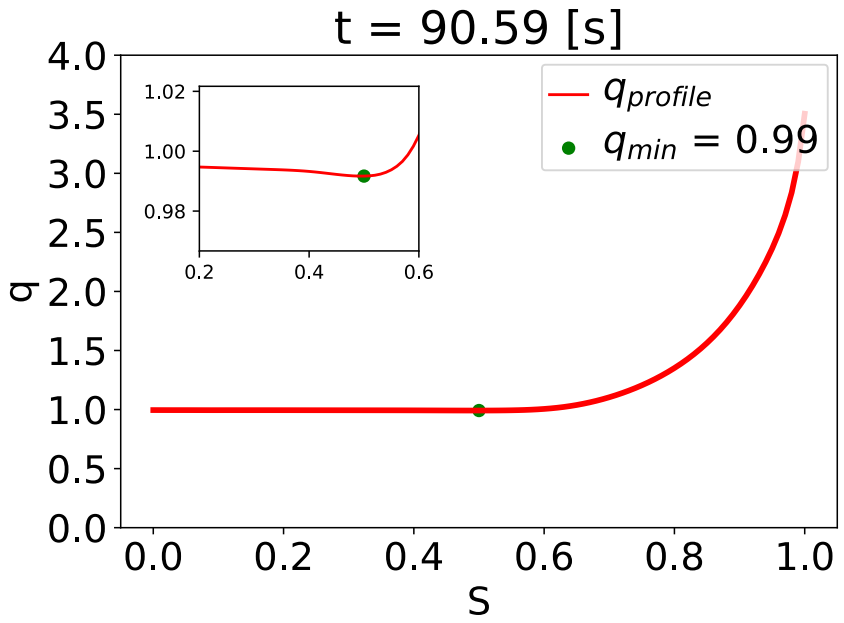

Figure 4.7: Safety factor profile at $t = 90.59$s. Zoom on the inner part of the tokamak. With a depiction of the minimum value of the profile.

reactors. Obviously, as both current and B field are much smaller than in ITER, various differences remain, in particular, those concerning the EP physics. The particle orbits of all EPs and the related relative EP pressures will lead to a different toroidal mode number spectrum as observed at JET. Compared with the ITER scenarios, the JET experimental data is more fine grained in terms of the time resolution of the data (0.02s between timepoints, compared to 3.712s). Despite the instabilities present in the discharge, it maintains a good confinement (see fig 4.12). No clear relation between Ti peaking and mode activity can be observed.

In discharge 99896, the plasma achieved a toroidal current (I_p) of 1.9 MA and a magnetic field (B_T) of 2.75 T. With a 50% D and 50% T fuel ratio, this setup reflects the anticipated configuration for future tokamak reactors optimized for fusion power output. As can be seen in Figure 4.8 the heating involved ICRF power (P_{ICRF}) of 4.5 MW and neutral beam injection (NBI) power (P_{NBI}) of 3.5 MW, divided between deuterium beam in the initial phase and tritium beam after 9 seconds. These parameters facilitated a regime where radiated power constituted about 60% of the total input, and fusion power peaked at 0.5 MW.

This plasma configuration reached a high confinement level indicated by $H_{98(y,2)} \approx 1$, matching the ITER baseline condition. This scenario maintained a low rotation state with a Mach number ($M = v_{tor}/c_s \approx 0.15$) at half radius, mirroring conditions

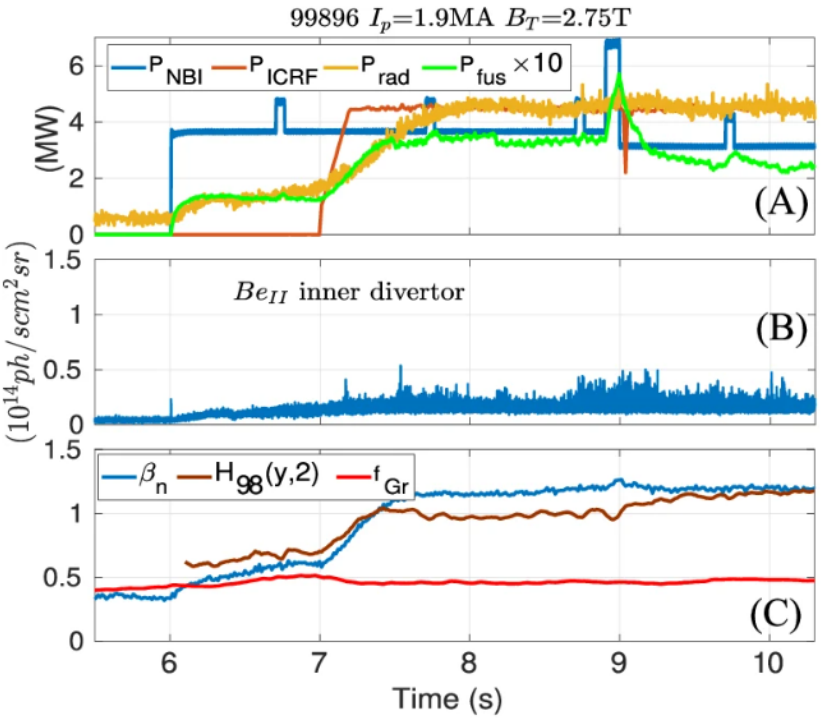

Figure 4.8: (Adapted from Figure 1 [61])Time evolution of discharge 99896. (A) shows the power of NBI, ICRF, radiated power and fusion power. (B) the time evolution of the edge fluctuations. (C) the time evolution of the ration between magnetic and thermal pressure.

expected in ITER D-T plasmas. Moreover, despite small edge fluctuations, significant electromagnetic perturbations were observed, including toroidal Alfvén eigenmodes (TAE), reversed-shear Alfvén eigenmodes (RSAE), and fishbone instabilities. These fluctuations, primarily driven by interactions between the energetic ions and Alfvénic modes, signal the presence of high-energy ions in the plasma. Magnetic perturbations detected through Mirnov coils further validated this behavior.

In Fig.4.9 the density, pressure and temperature profiles for the JET scenario at $t = 9.108$s are shown. It can be seen that the fast ion density is very low compared with the thermal density, that is why the density of the fast particles is multiplied by a factor of 10 before plotting. Time 9.108s is chosen because it is the time when the fast Tritium is also present in the plasma. Important to note is the highest gradient region for fast particle density and pressure, which is the region where the TAE is expected to grow. The peak of the gradient is at $\approx< 0.25$, and a finite gradient up to 0.5 ρ_{tor} is present. For the analysis of the TAE, we will focus on this region, and thus, we will use the workflow to determine what modes are present in this radial range.

As discussed above, the q profile is a very important parameter in determining

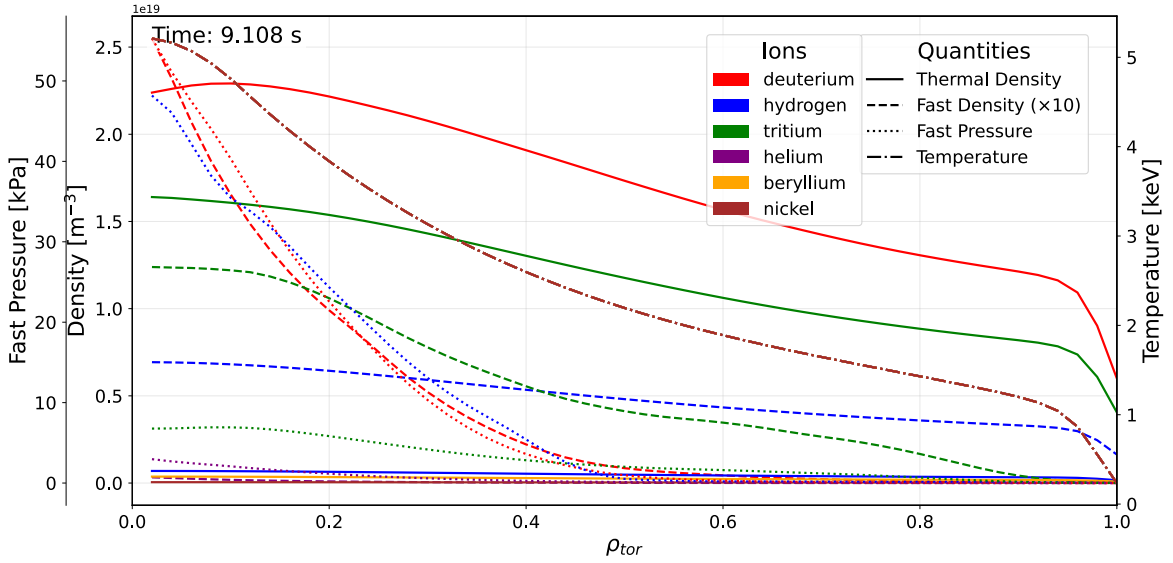

Figure 4.9: JET scenario density (fast and thermal), pressure (fast) and temperature for hydrogen, deuterium, tritium and alpha particles at $t = 9.108$s.

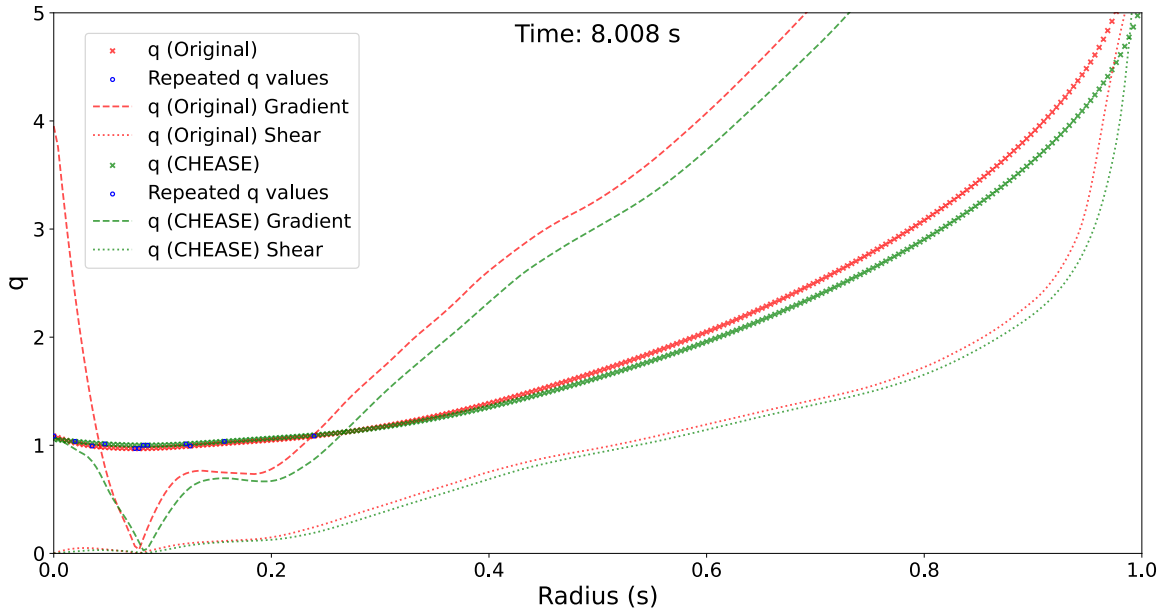

Figure 4.10: JET scenario safety profile (q-profile) at $t = 8.008$s. Also marked are the graients of the q-profile (original data,red and CHEASE, green). Marked with blue are the repeating q values before and after runnung HELENA i.e. transformation to straight field line coordinates.

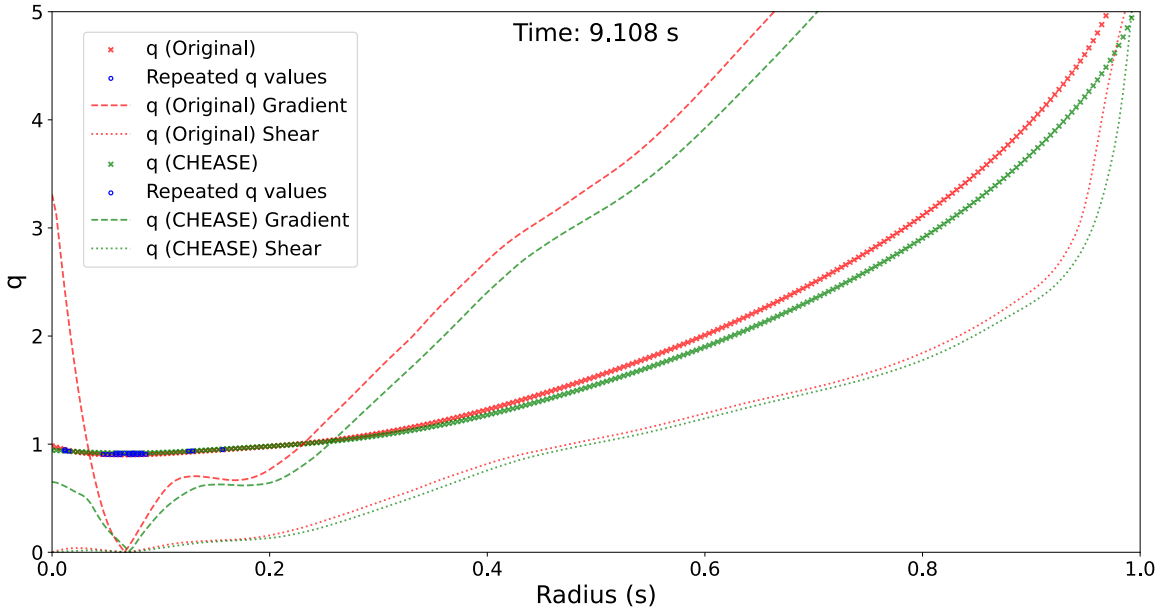

Figure 4.11: JET scenario safety profile (q-profile) at $t = 9.108$s. Also marked are the graients of the q-profile (original data,red and CHEASE, green). Marked with blue are the repeating q values before and after runnung HELENA i.e. transformation to straight field line coordinates.

the TAEs that are present. In Fig.4.11 the q-profile at $t = 9.108$s is shown. Also marked are the radial derivative and shear (rq'/q) of the q-profile (original data,red and CHEASE, green). Boundary conditions on axis give small changes between CHEASE and HELENA. The q-profile is not strictly monotonic and thus, multiple TAE surfaces are possible, especially in the region close to the core of the reactor (marked with blue). The q-profile at $t = 8.008$s is shown in Fig.4.10. Throughout the discharge, q-profile decreases. This is in contradiction to the fact that continuous small, core-localised sawtooth crashes are observed in the whole discharge indicating a more or less constant radial location of the $q = 1$ surface. The constraint on the $q = 1$ surface is not satisfied by the given equilibrium, and such, a 1 to 1 mapping between simulation and the experimental data cannot be expected. A comprehensive analysis of the TAEs in this shot is presented in the results chapter (5).

In figure 4.12 the core ion (Deuterium, red) and electron (blue) temperatures are overlaid with the magnetic data from the JET D-T experiment. The figure shows that the core ion temperature is very transient even during one sawtooth crash (8.3s-8.75s). The ion temperature already decreases before the crash at 8.75s. This shows that T_i peaking is not a universal feature of these discharges, but rather depends on a compex interplay of large scale MHD transients, EP transport and turbulence. The presence of

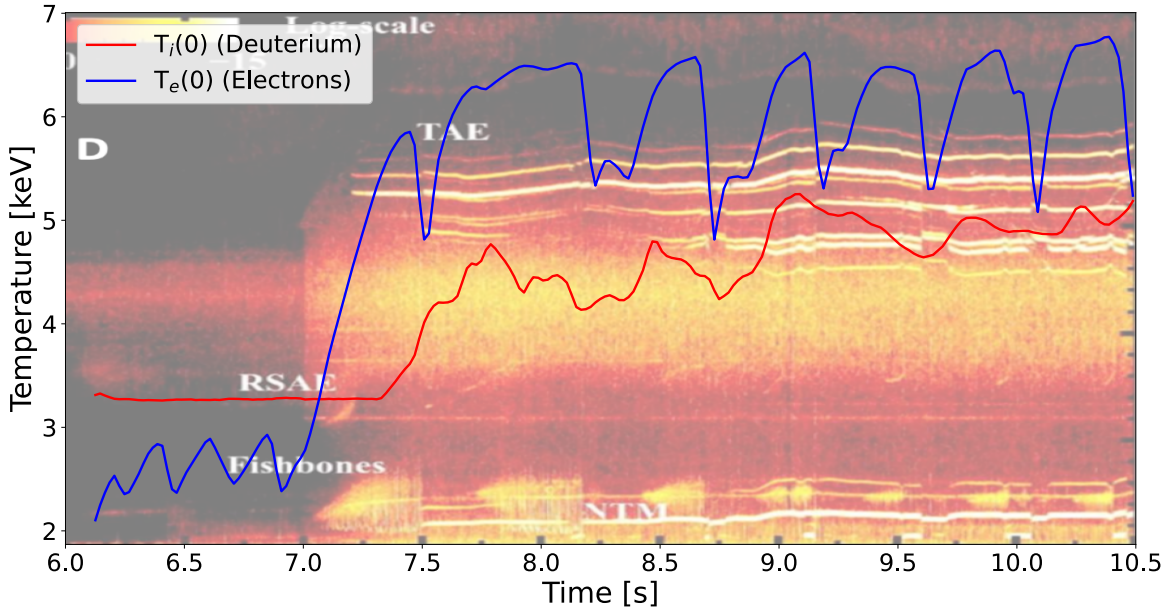

Figure 4.12: Adapted from Figure 1 [61]. Overlaid the core ion (Deuterium, red) and electron (blue) temperatures. No clear relation between T_i peaking and mode activity can be observed. T_i degradation can be observed in phases before the sawtooth crash, indicating that the T_i peaking is not a universal observation in this discharge, but rather a transient process indicating a complx interplay between sawtooth cycle, EP transport (TAE and fishbones) and turbulence.

RSAEs, TAE and fishbones alone is not enough to understand T_i peaking, as it has been discussed in [67].

On the other hand, in the JET D-T scenario, an equivalent discharge in pure deuterium (100871) was performed under similar power and density conditions to allow direct comparison. The results showed an enhanced thermal confinement in D-T plasmas over D, particularly within the plasma core, where the ion temperature gradient increased, reflecting a reduction in heat transport. This distinction was further quantified by calculating ion and electron heat diffusivities (χ_i and χ_e), which showed reduced ion heat transport in the D-T scenario compared to pure deuterium conditions.

The discharge parameters and observed instabilities illustrate the nuanced behavior of energetic particles in a reactor-grade plasma, offering a challenging test case for predictive models. By analyzing this scenario, we can test the capabilities of the EP-WF in a scenario with a high-energy and multi-species fast ion content.

5 Results

In this chapter, we present a comprehensive analysis of the results obtained from various tokamak scenarios and experiments using the Energetic Particle Workflow (EP-WF), providing insights into the behavior of Toroidal Alfvén Eigenmodes (TAEs) across different predictive and experimental discharges, including ASTRA, DINA-JINTRAC, METIS, and JET DT. Each section delves into the specific characteristics and findings of these scenarios, highlighting the capabilities and limitations of the workflow in capturing the complex physics of TAEs. The chapter begins with an analysis of the ASTRA scenario, where a wide array of TAEs is scanned to verify the behavior of various modes characteristics in a time-independent setting. This is followed by the DINA-JINTRAC scenario, which focuses on the ramp-up phase of a simulation, providing a deeper understanding of the radial positioning and frequency evolution of TAEs. Next, the METIS scenario is explored, showcasing the workflow's ability to handle complete, time-dependent information, including energetic particle profiles. This section emphasizes the importance of convergence tests and the impact of alpha particles on TAE stability. The focus of the study then transitions to the JET DT discharge, an actual experimental case, where the workflow is applied to interpretative modeling of DT experiments. This section highlights the challenges and inconsistencies in equilibrium reconstruction and the significance of realistic energetic particle distribution functions. Throughout the chapter, various figures and analyses illustrate the radial locations, frequencies, and growth rates of TAEs, providing a detailed understanding of their behavior under the influence of different EP species. The results demonstrate the workflow's effectiveness in capturing key features of TAE dynamics, while also identifying areas for future improvement, such as incorporating more realistic fast particle distributions and addressing non-linear effects.

5.1 ASTRA - 131025/34

In this time-independent scenario, we perform a scan over a wide array of TAEs ($n = 1 \dots 35$ and $m = n \dots n + 4$) for the given time slice in order to check if all WF elements (including the kinetic multi-species aspect) are behaving as expected. For this case, we include only thermal background particles, i.e. electrons and a 50:50 D-T mix

satisfying quasineutrality at each radial slice.

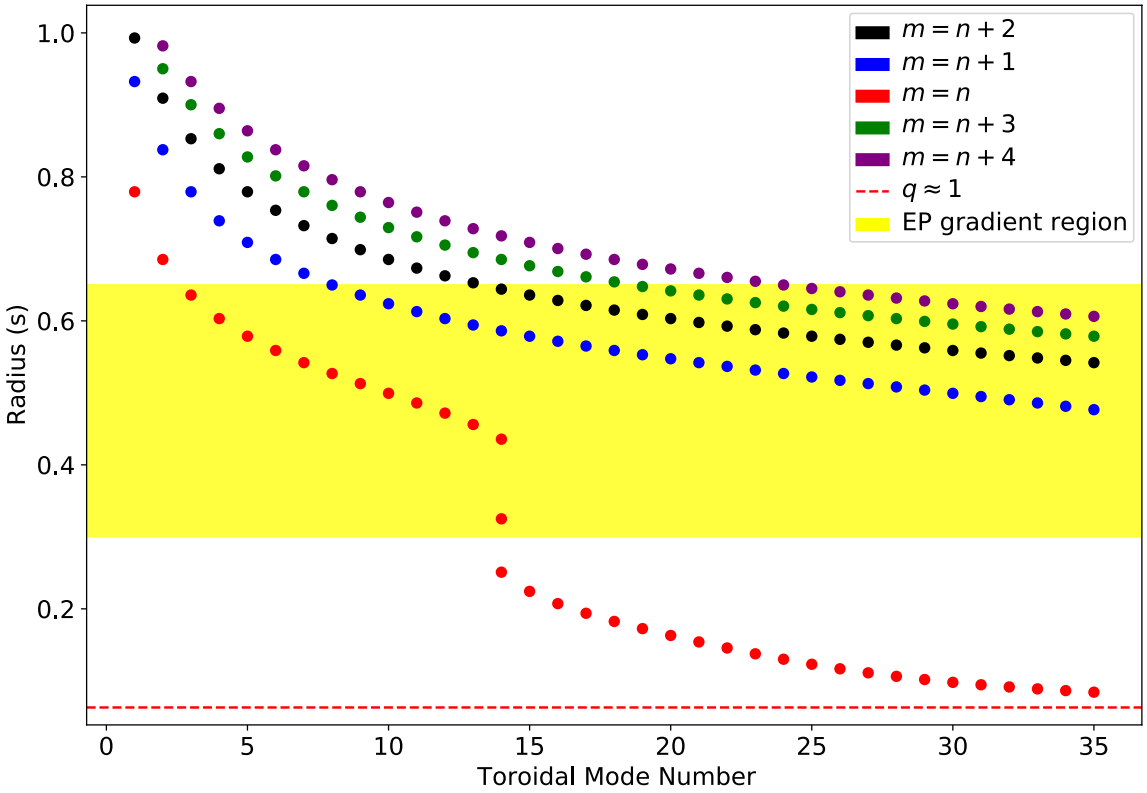

Figure 5.1: Radial location of modes with toroidal mode number (n) between 1 and 35 for $m = n$ to $m = n + 4$. For reference, the $q \approx 1$ position is depicted with the red dotted line. Highlighted in yellow is the region of interest for the TAEs as in this region the maximum of the alpha particle gradient is expected.

In Figure 5.1 the radial location of the modes over the whole radial domain is presented, with the $q \approx 1$ rational surface being marked as a red line. LIGKA model 5 uses as an analytical estimate the TAE condition $q = \frac{m+\frac{1}{2}}{n}$. Also, more sophisticated formulae based on [47] are implemented, taking into account elongation and β corrections (not shown here). However, it turns out that the simplest expression gives a good estimate for the center of the TAE gap (that is needed for the subsequent analysis) in all geometries and mode number ranges investigated so far. Part of the modes can be typically discarded in the following analysis (local and global kinetic analysis) based on their position relative to the EP gradient: the alpha particle gradient is significant only in the region $0.3 \ldots 0.65$, thus the modes that do not fall in this range were excluded since they are expected to be linearly stable. Unfortunately, as explained above, details about EP pressures and densities are not available for this simulation. Based on these

considerations, the radial range of interest can be conveniently defined via the input files (XML data structure, editable directly, or via a GUI), allowing the user to have flexible control over the considered mode spectrum. A further automatisation can be implemented in the future, for example when the workflow will be directly coupled to transport codes, by defining a critical $\beta_{max}(r)$ and restricting the range of interest accordingly.

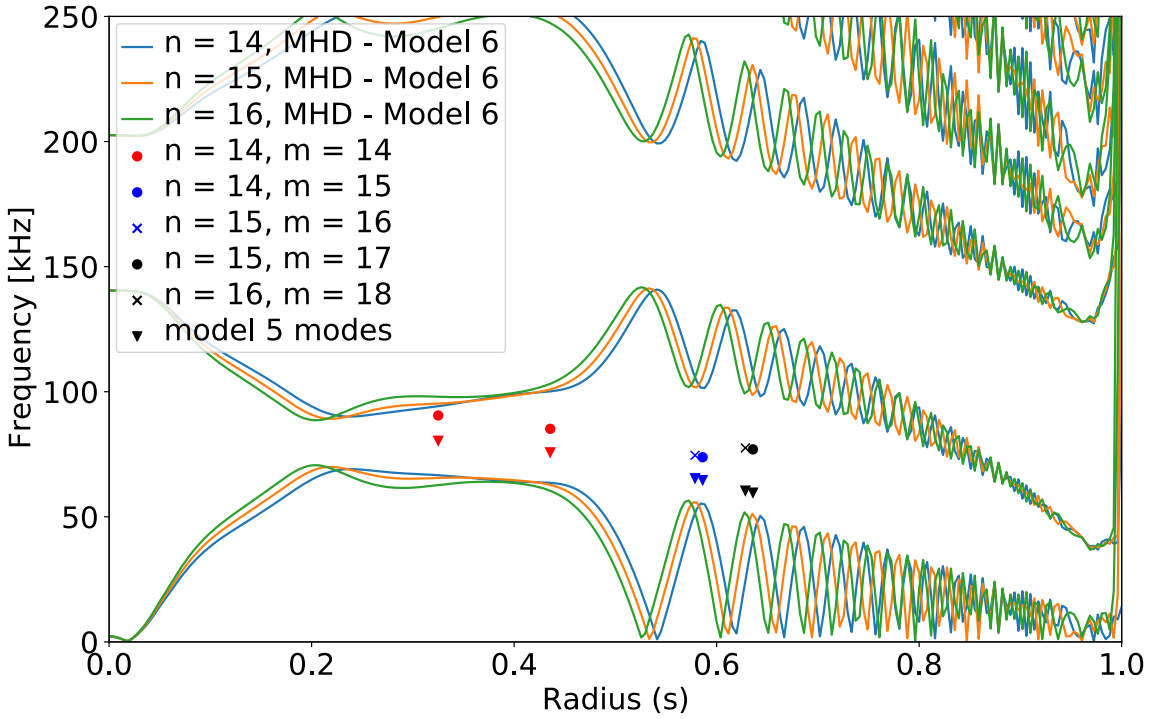

Figure 5.2: Local continuum for $n = [14, 15, 16]$ with selected modes position depicted on the same graph. The modes have the same color scheme as the ones in the above analysis on the radial location. Triangles are the simple analytical estimates, the dots are the global results as obtained with model 1.

For all selected toroidal mode numbers the shear Alfvén wave continuum(SAW) can be calculated (model 6), as shown in figure 5.2 for $n = 14, 15, 16$. All branches of TAEs in the radial range discussed above are added. It can be seen that the simple analytical guesses (model 5) lie typically in the TAE gap, as expected. The two solutions for n=14 are shown (see figure 4.2), separated in frequency by the changes in the local Alfvén velocity. Following this, we calculate the global solutions with Model 1. In Fig.5.3 (round dots) the normalised mode structures (electrostatic potential) for the two modes $n = 14$, $m = (14, 15)$ found at different radial locations are displayed (as explained before). By taking these structures and adding them to the continuum, (see Fig.5.3)

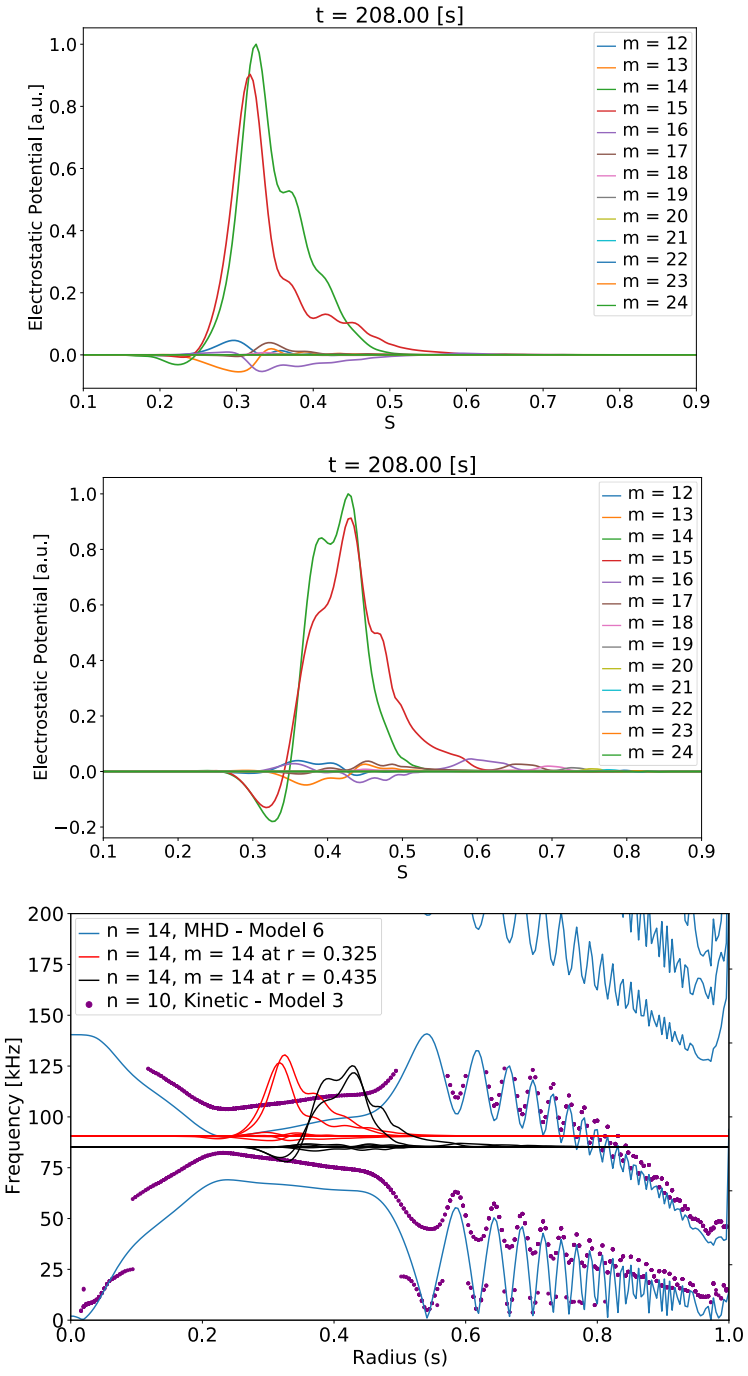

Figure 5.3: Top 2 figures contain the real part of the electrostatic potential of the $n = 14$ $m = (14, 15)$ modes found after restricting our domain. Underneath, is their location on the local continuum (model 6) and kinetic continuum (model 3).

one can see that they intersect the reduced SAW continuum. This is not surprising since the global solutions include various kinetic effects not accounted for in the reduced MHD model, in particular, the diamagnetic upshift of the continua in regions of high plasma pressure [49]. In Fig.5.3 last subfigure, the local kinetic continuum -model 3- is added. For a detailed description of this local solution of the kinetic dispersion function see [43]. From the figure one can see that using the kinetic model consistently in both local and global calculations, the TAEs are, as expected, situated in the kinetic TAE gap, avoiding local continuum damping. It becomes apparent from this discussion, that the kinetic corrections for these ITER scenarios and mode number ranges are significant and cannot be neglected as often done in present-day experiments where both the plasma beta and the excited TAE mode numbers are typically much lower.

This demonstrates that the chosen hierarchy, analytical - local kinetic - global kinetic, is indeed a very powerful and absolutely essential procedure. The workflow handles this considerable complexity consistently and transparently, and facilitates a deep and comprehensive physics understanding of the underlying scenarios.

5.2 DINA-JINTRAC - 134173/106

In this subsection, the previously discussed capabilities of the workflow are used to analyze the ramp-up phase of a DINA-JINTRAC scenario simulation (134173/106).

Similarly to what has been shown in the last section, a run was performed at one time point ($t = 97.93$s), using the analytical model (model 5). For this run, TAEs with $n = 1$ to $n = 35$ with $m = n - 2$ to $m = n + 2$ as main poloidal harmonics were considered. Fig.5.4 shows the radial position of these modes together with the $q \approx 1$ rational surface. As expected, modes with low toroidal mode numbers are shifted away from $q = 1$ towards the core, when the poloidal mode numbers are lower ($m = n - 2$) or towards the edge when $m = n + 2$ according to $q_{TAE} = \frac{m+\frac{1}{2}}{n}$.

Next, a specific TAE with $(n, m) = (25, 24)$ was tracked during the ramp-up phase of 134173/106. This mode was chosen based on the fact that q_{min} is slightly below 1 in most of the time points, meaning that the TAE with $(n, m = n - 1)$ is present throughout the whole ramp-up and flat top phase. Also, previous analyses found that modes between $n = 15 \ldots 30$ are expected to be the most unstable linear TAEs in ITER 15MA scenarios [53, 68, 69].

Fig.5.5 shows the frequency evolution of the same mode. Plotted are the different models used by LIGKA. Starting with the analytical model (blue line), continuing with the local solver, model 4 (orange line) and finally the global solver, model 1 (green line). Performing convergence tests as described above we found that the range of poloidal harmonics [−4,+32] is necessary to study this particular part of the scenario. Features

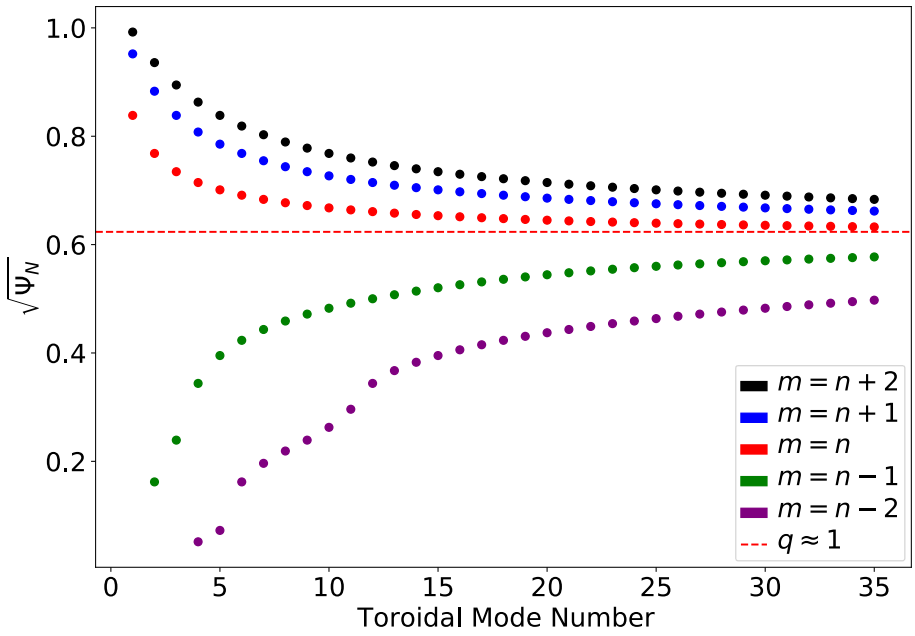

Figure 5.4: Radial location of modes with toroidal mode number (n) between 1 and 35. Poloidal mode numbers are from $m = n - 2$ to $m = n + 2$. $q \approx 1$ location is depicted with a red line for reference. This run is performed only at $t = 97.93$s .

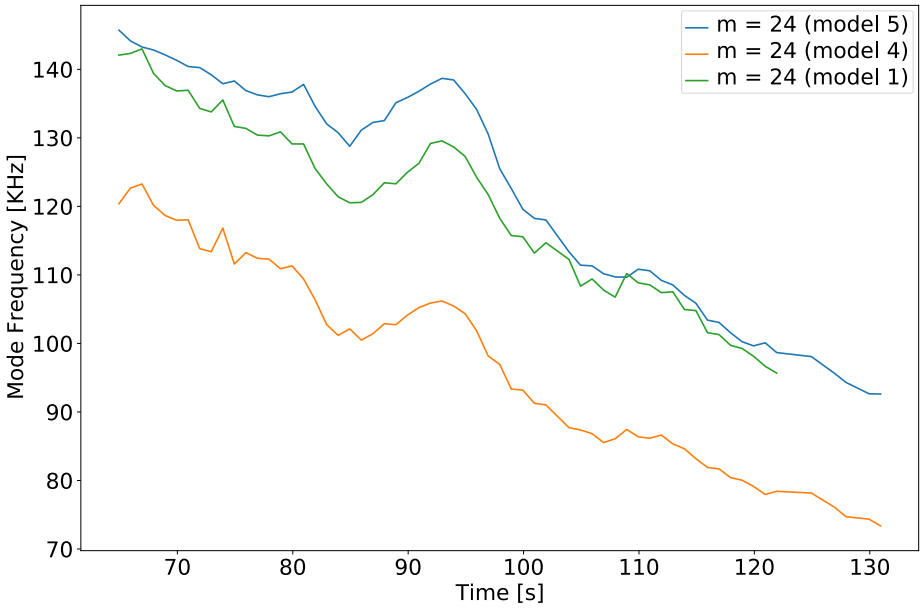

Figure 5.5: Frequency for the $n = 25$, $m = 24$ TAE during the ramp-up phase of 134173/106

from the computations regarding the frequency of the mode can be seen here as well, in addition to the general Alfvén scaling trend: due to the rising density, the frequency decreases due to $f_{TAE} \propto \frac{1}{\sqrt{n}}$. Model 5 results in the highest frequency (middle of the gap), model 4 the closest continuum (downwards, lower frequency) and finally model 1 determines the exact location of the TAE within the gap via a global analysis.

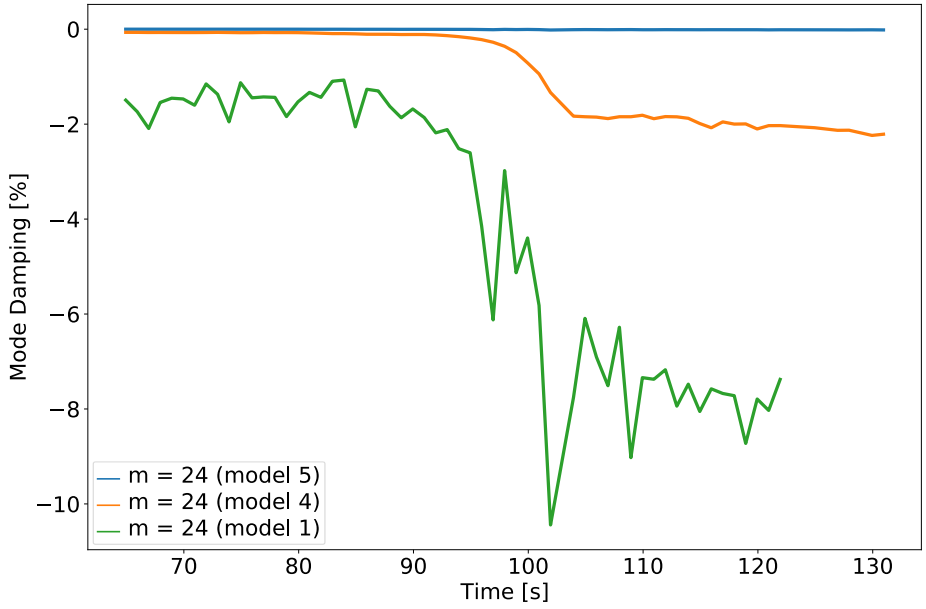

Figure 5.6: Damping rate for $n = 25$, $m = 24$ mode along the ramp-up of the scenario.

Fig.5.6 shows the damping rate of the TAE, during the same period of time (ramp-up). Again, a considerable difference between models can be noticed, with model 1 being the most reliable, clearly showing that the local damping rate underestimates the global one considerably, as explained above. It can be seen that the chosen TAE is strongly damped in the flat top, whereas during the ramp-up phase, the damping rate is much smaller. In this case, especially for the jump in damping around $t = 100$s, non-local continuum damping is the dominant effect, demonstrating the exponential sensitivity to small profile changes. Clearly, this motivates future detailed studies including the drive from the neutral beams and the the alpha particle drive that were not included in this calculation, especially at the end of the ramp-up phase where considerable EP gradients are. Even then, relatively weak damping can be expected.

For completeness, the mode structure is presented in Fig.5.7. One can see that despite the high toroidal mode number, the mode is quite global due to the flat shear around $s = 0.5$. However, as Fig.5.8 shows, the continuum damping is negligible since the mode touches the continuum at s=0.9 where all poloidal harmonics with

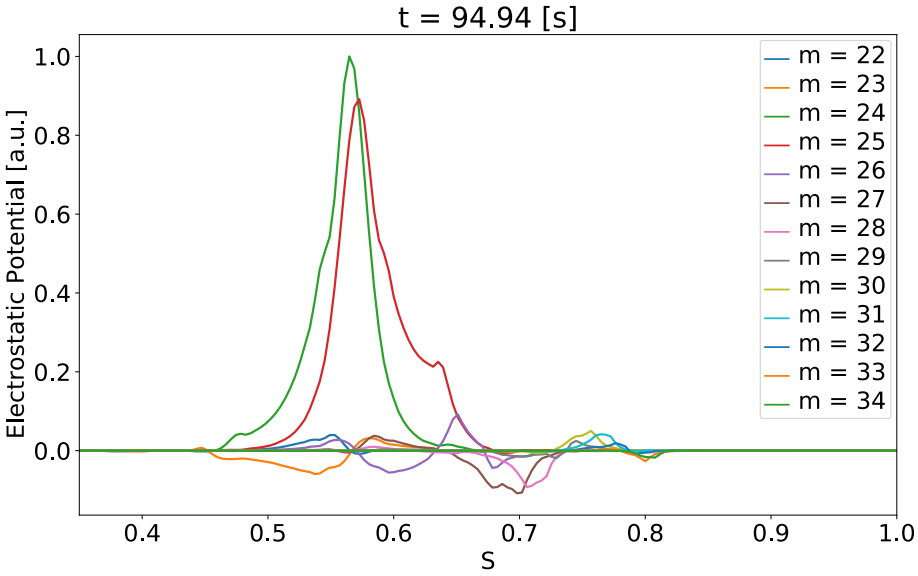

Figure 5.7: Mode structure for $n = 25$, $m = (24, 25)$ mode for $t = 94.94$s

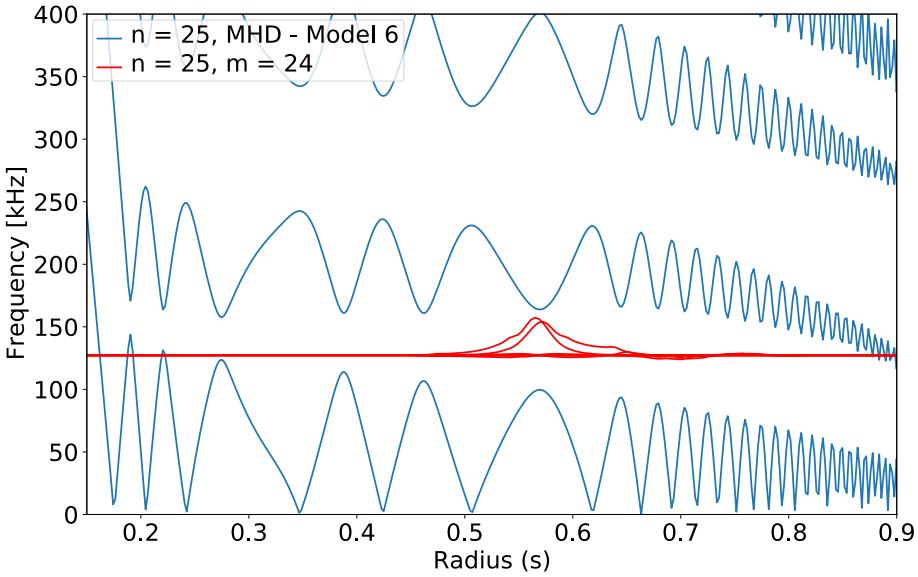

Figure 5.8: SAW continuum with the global TAE $n = 25$, $m = (24, 25)$ mode structure

significant relative amplitudes have decayed. Thus, just other non-local damping effects (Ion/electron/radiative) are contributing via the wide mode structure to the overall mode damping.

5.3 METIS - 130012/02

In order to demonstrate all the capabilities of a complete and automatic tool for linear stability inside a tokamak, we use the METIS-generated scenario, the first case with complete, time-dependent information, including energetic particle profiles, that was made available to me in IMAS. Starting from an overview of the TAE locations and frequencies (via model 5) to a more in-depth analysis via the local (model 4) and then a global solver (model 1/2) was performed. First, alpha particles are excluded to determine the damping rates, and then the effects of alpha particles are added. In addition, a convergence test was performed in order to investigate and optimize the computational resources for the various analysis steps.

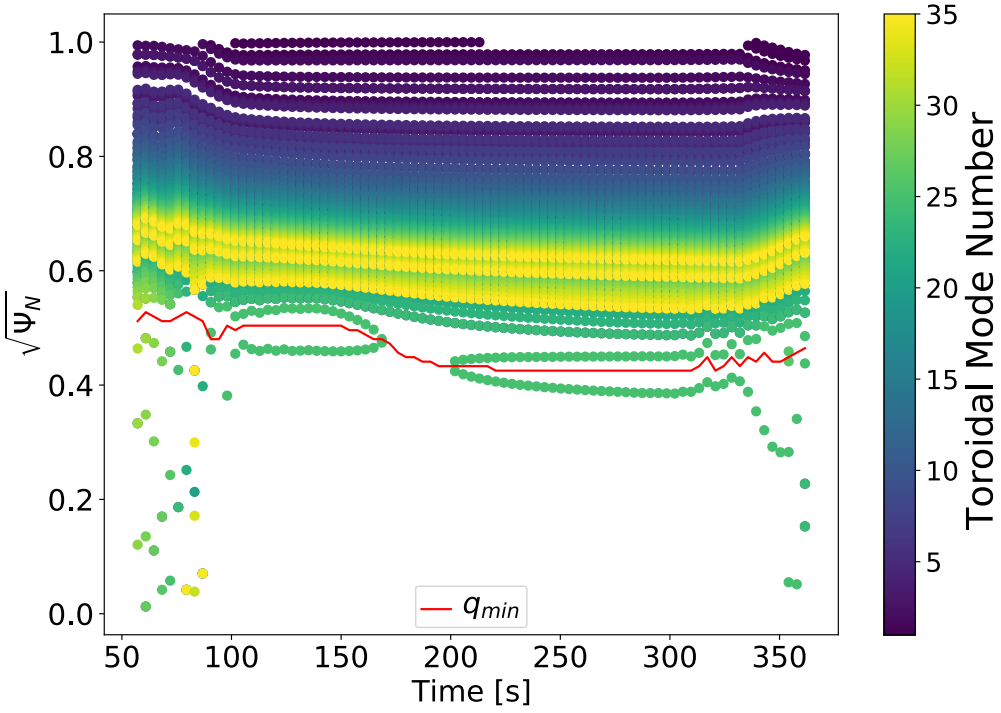

Figure 5.9: Radial location of modes with toroidal mode number (n) between 1 and 35 tracked over the entire scenario.

Due to the ability of model 5 to perform basic analytical AE calculations in a short

amount of time (<1s - mode - time step), a scan over the whole METIS scenario (106-time points) was performed taking $n = 1 \ldots 35$ and $m = n + 1 \ldots m = n + 5$ for a total of 12014 modes, averaging about 137 modes per time point. In Fig.5.9 a plot of all these modes' positions over time is given. Pointed in the graph is also the $q \approx 1$ value for each time point. The slight inversion of the q-profile around $\sqrt{\psi_N} \approx 0.5$ in the flat top part of the scenario (> 90s) leads to two different TAE branches with the same mode numbers. Also, after (> 90s) no TAEs are found in the core ($s < 0.4$). This is a consequence of the extremely small magnetic shear in the core assumed by the METIS-given equilibrium.

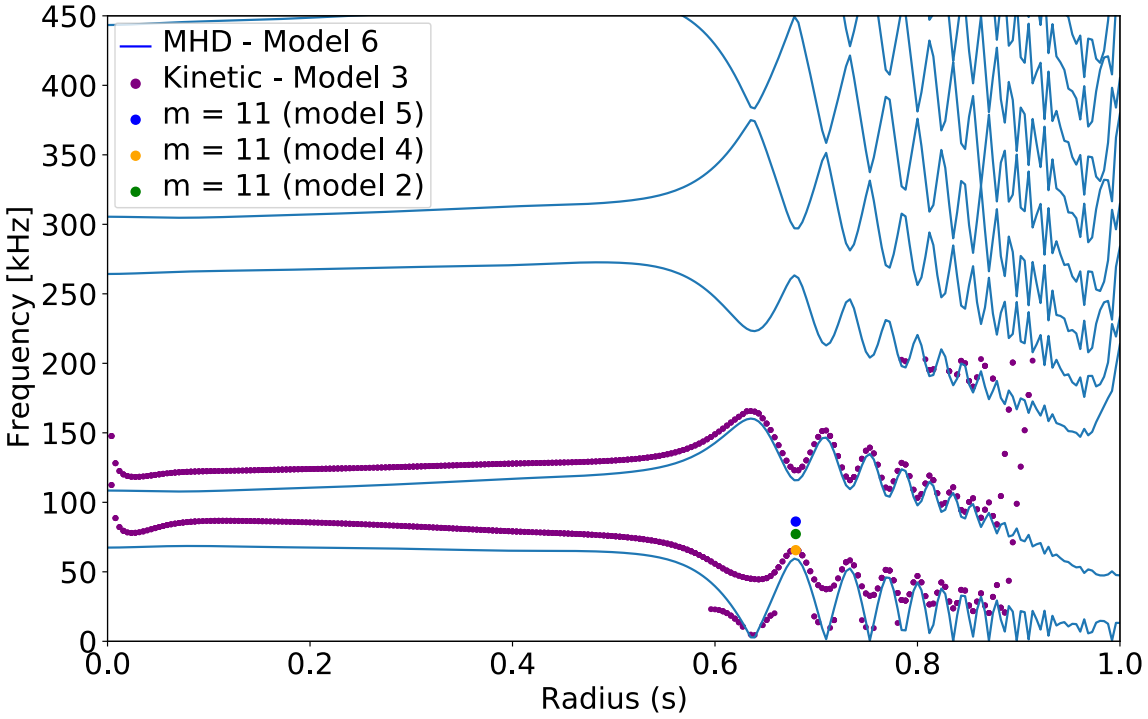

Figure 5.10: Continuum for $n = 10$, $m = 11$, with blue lines the MHD (Model 6) and with orange dots Kinetic (Model 3) at $t = 90$s. The dots indicate the TAE frequencies as calculated by model 5 (analytical), 4 (local kinetic) and 2 (global kinetic).

In Fig.5.10 the reduced SAW continuum and the kinetic continuum for $n = 10$ are plotted. The results for one TAE ($m = 11, 12$) using the model hierarchy are added. As in the previous case, the different models give slightly different TAE frequencies (colored dots in fig 5.10), in line with the discussion above.

Since the SAW continuum in Fig.5.10 shows an almost open TAE gap, it is investigated how many poloidal harmonics are needed for the convergence of this mid-n (n=10)

TAE. This test is also of significant importance for solver validation inside LIGKA and the EP-WF. Several runs were done by looking at the same mode $(n, m) = (10, 11)$ using a different number of poloidal harmonics.

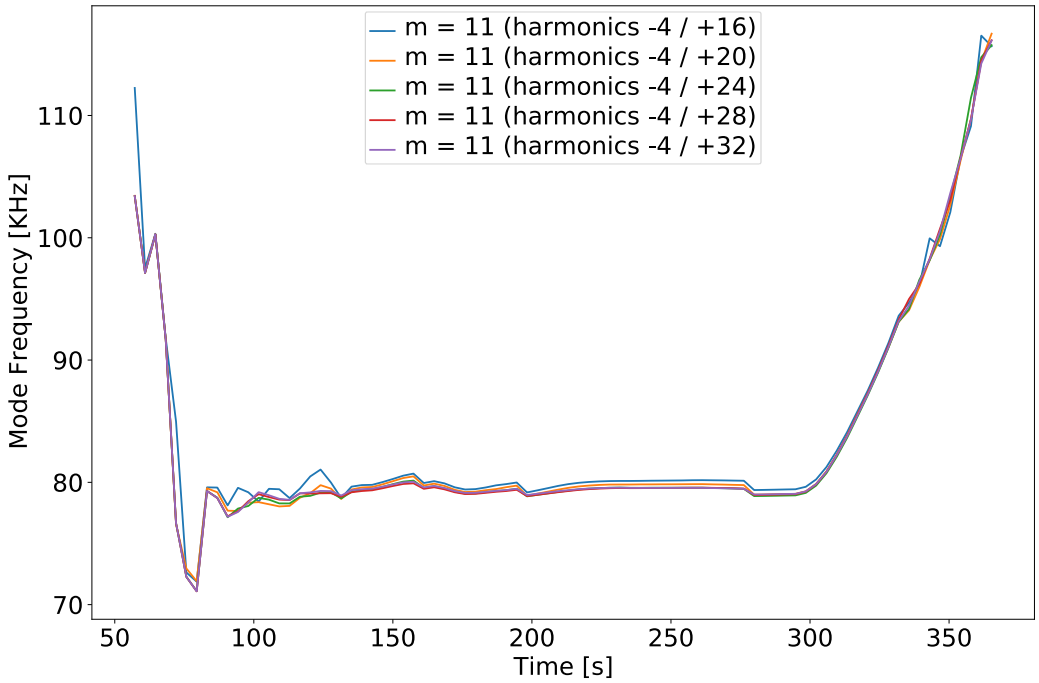

Figure 5.11: Frequency scan for $n = 10$, $m = 11$, for different numbers of poloidal harmonics tracked for the duration of the scenario.

In Fig.5.11 the mode frequencies calculated using different numbers of poloidal harmonics are shown. The frequency differences between the different runs are not significant. During the ramp-up ($50 <= t <= 100$s) and ramp-down ($300 <= t <= 400$s), the variation in frequency is determined by the evolution of the density, temperature and safety profile. Note that the time step size for equilibria and profiles in this scenario is ≈ 3s. For the flat-top phase of the scenario with stable profiles, almost no changes in the TAE frequency are observed.

In Fig.5.12 the damping rate of the same mode is plotted, similarly to Fig.5.11. Fig.5.13 shows the mode structure of this mode for the same number of harmonics. In this case, if the number of poloidal harmonics is varied, significant differences are observed. As it can be seen, the number of poloidal harmonics for convergence depends on the equilibrium, i.e. particularly at the end of the ramp-up phase non-local continuum damping towards the plasma edge requires many poloidal harmonics to be included. This difference is particularly pronounced in the most unstable (profile-wise)

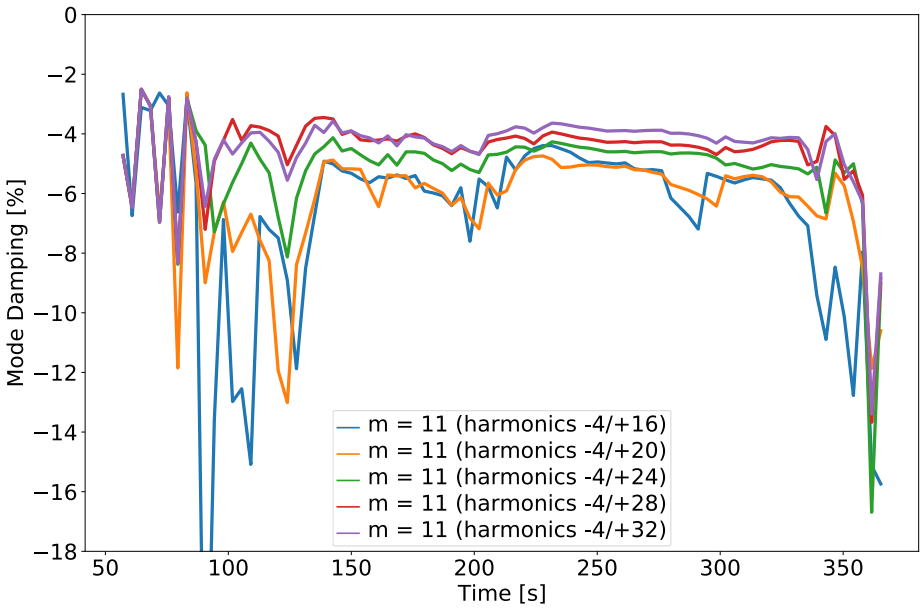

Figure 5.12: Growth rate for $n = 10$, $m = 11$, for different numbers of poloidal harmonics tracked throughout the whole scenario.

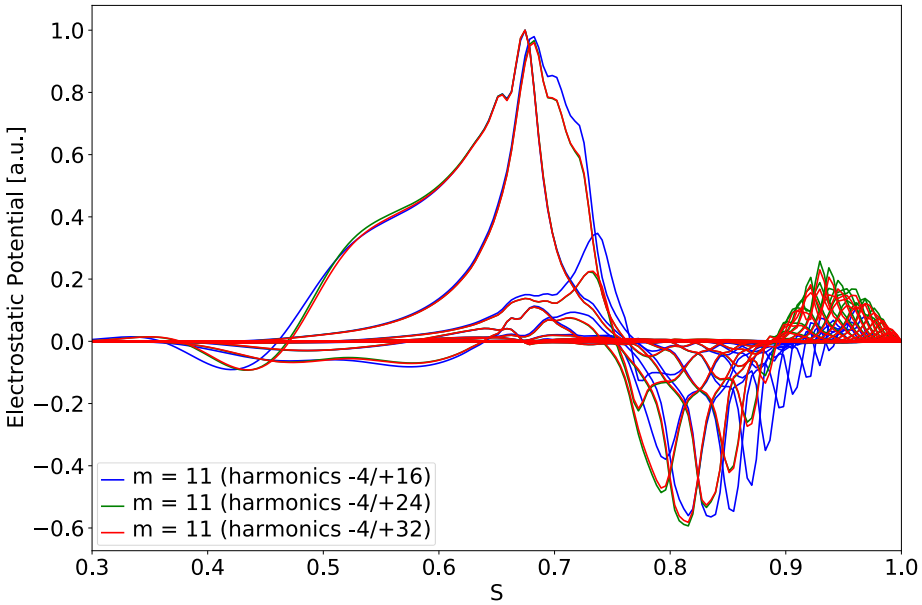

Figure 5.13: Mode structures of $n = 10$, $m = 11$, for different numbers of poloidal harmonics at $t = 90$s.

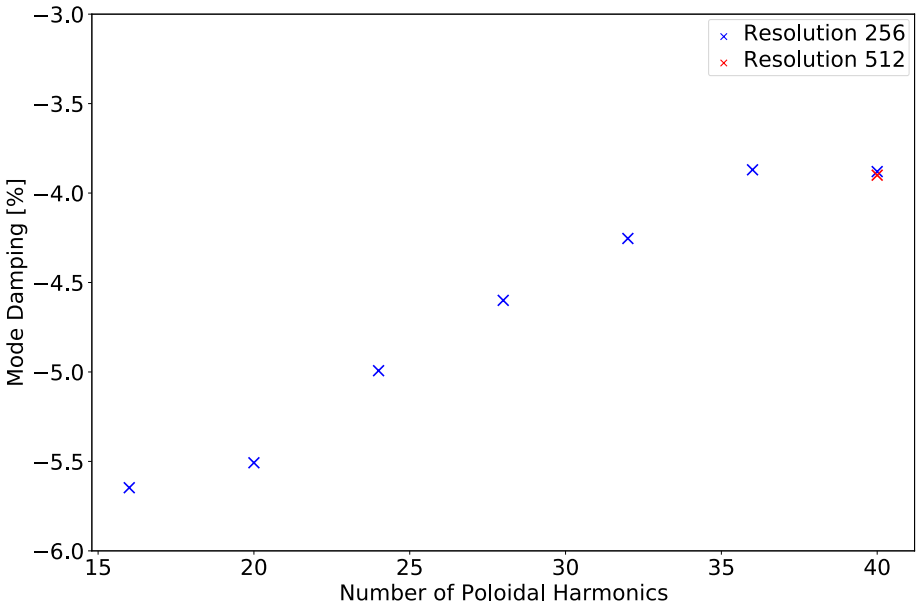

Figure 5.14: Growth rate for $n = 10$, $m = 11$, for different numbers of poloidal harmonics and resolutions, focused on the flat top phase of the scenario. The x-axis shows the number of poloidal harmonics, and the y-axis the growth rate. The different colors indicate the different radial resolutions.

regions of the scenario: ramp-up and ramp-down. As depicted in the graph with blue we use 21 harmonics (from $m = n - 4$ to $m = n + 16$). One can see that as more harmonics are added, the results become more and more weakly damped. In the flat top region of the scenario, the difference is not that significant $\pm 0.5\%$, whereas, in the ramp-up phase, the damping strongly depends on the number of poloidal harmonics ($\approx -25\%$). Adding more harmonics leads eventually to a converged damping rate, especially in the ramp-up phase (90-110s). Obviously, the mode number $n = 10$ was chosen as the most challenging case for this scenario, since the global TAE touches the continuum close to the plasma edge, explaining the slow convergence behavior: as the number of poloidal harmonics is increased, the interaction with the continuum is radially further and further separated from the main TAE location, decreasing the damping rate (see fig.5.12).

The continuum intersection moves to the edge and thus smaller and smaller poloidal harmonics interact with the (not yet resolved) continuum until it is fully resolved ($-4/+28$ and $-4/+32$). In order to demonstrate convergence three extra runs were performed: two with the higher number of harmonics (+36 and +40) and one for a higher radial resolution (512 radial grid points). This can be seen for 1-time point ($t = 250$s) in the flat top region of the scenario (Figure 5.14). Based on this, one can conclude that $-4/+28$ and $-4/+32$ harmonics are enough to achieve convergence for this particularly demanding TAE.

Next, alpha particles coming from the fusion reactions were added, as given by the scenario simulation. For simplicity, an effective hot Maxwellian was chosen, consistent with the EP pressure and density as given by the transport code. In Figures 5.15 and 5.16, the frequencies and damping rates for the same $n = 10$ and $(m = 11, 12)$ TAE for the whole time domain ($t = 45 - 360$s) are shown. Based on the previous analysis, the poloidal harmonics included in this simulation was $-4/+32$ which was found to be the necessary range needed for convergence. Again, the various models are run and compared (dashed lines: no alphas, solid: alphas). The blue vertical line on the graphs indicates the moment when a significant population of alpha particles starts to be present in the plasma due to fusion processes,

As expected, the frequency did not shift by a significant margin (Fig. 5.15) between runs with alphas or without.

Fig.5.16 shows the damping rate for both cases, with and without alpha particles taken into consideration. Using model 4 (local solver - orange line) one can see that there is a small difference between the cases with and without EPs. Moreover, this local model suggests that in the ramp-down, the TAE becomes unstable in the presence of alphas. Using the global solver (model 1/2 - green line) one can see that this is not the case, due to the non-local damping mechanisms. At $t \approx 90$s when alphas are turned on, the damping rates start to differ. However, while the alphas do reduce

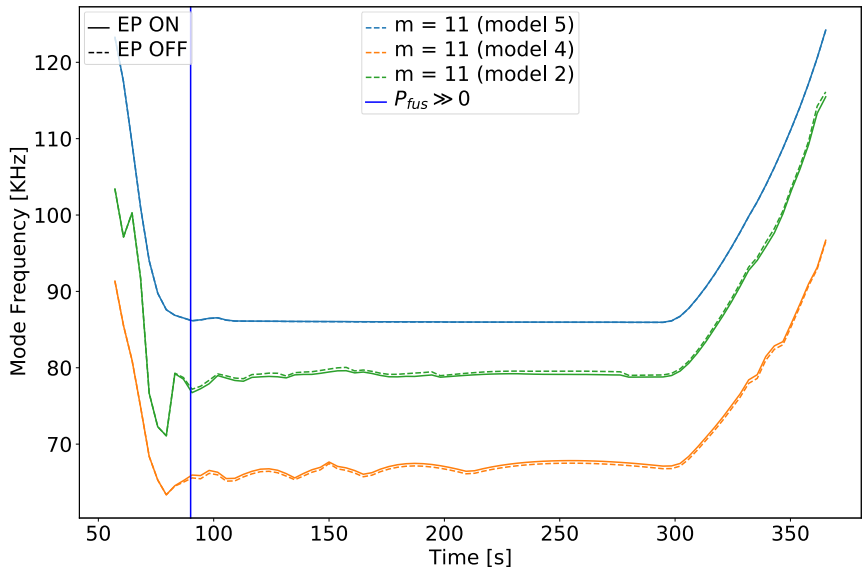

Figure 5.15: Frequency for the $n = 10$, $m = 11$ mode as function of time. Results with (solid) and without (dashed) alpha particles are shown.

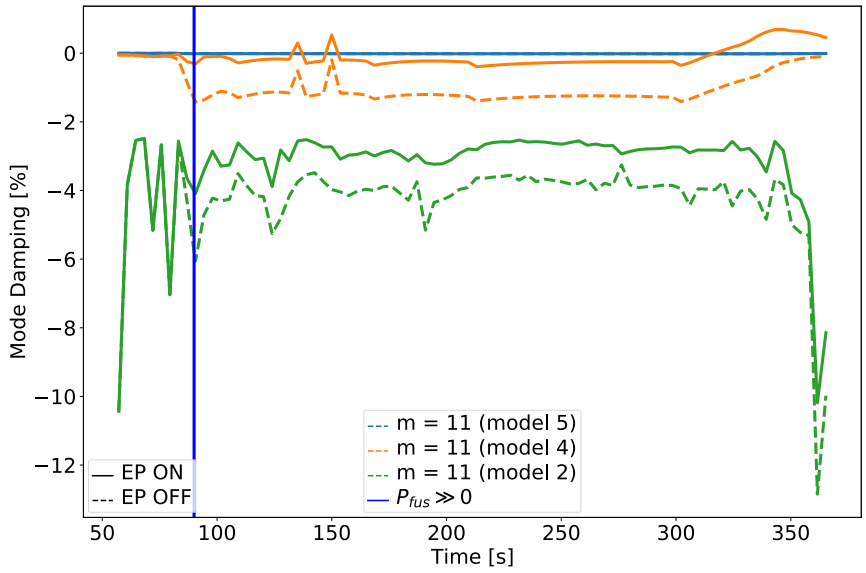

Figure 5.16: Damping rate for the $n = 10$, $m = 11$ mode as a function of time along the whole scenario. Results with (solid) and without (dashed) alpha particles are shown.

damping, the TAE does not become unstable throughout the whole scenario. The same is true for other n's (tested for $n = 10...30$) showing that this extremely (unrealistically) flat q-profile results in a decoupling of TAE locations and steep EP gradient regions, leading to a stable TAE spectrum. Small equilibrium deviations can change this. If for example a sawtooth cycle with a periodic q-profile evolution around $q = 1$ is assumed or assuming different models for density peaking. Using the established workflow sensitivity scans based on slightly differing assumptions in the scenario modeling process can be systematically investigated in the future. As shown in this subchapter, some needs for future ITER studies are:

1. wide toroidal mode number range
2. potentially many poloidal harmonics
3. good sawtooth model

This can be done by continuously integrating and expanding the Energetic Particle Workflow with new codes in order to better capture new needed physics.

5.4 JET - 99896/05

Whereas so far we have been looking at predictive ITER scenarios (the first ones becoming available in IMAS in 2020 when this work started), we now focus on an actual experimental case, based on an experiment executed in 2022 made available to us late 2024. As will be shown, the modelling is not fully satisfying, however the application of the workflow very nicely helps to identify inconsistencies and shortcomings in the interpretative modelling, in particular concerning equilibrium reconstruction (q profile) and the importance of realistic EP distribution functions.

Given the complexity of the JET experimental data, a unique opportunity to validate the workflow and obtain valuable insights into the widely noticed [70] DT experiment is given. In the past, complex scenarios or experiments were typically analysed by taking a single time-point and making a comparison with the experiment based on that only. Trends can be predicted with more confidence than absolute values, this being one of the main strengths of the EP Stability workflow. Moreover, in order to validate the reconstruction of the equilibria and the profiles over several time-slices, a comprehensive analysis is needed that allows an iterative improvement of the original data with the constraints shown by the workflow results.

Several objectives were set for this subchapter:

- Performing a time-dependent analysis on experimental DT data using IMAS-integrated EP-Stability workflow.

- Validation of the model hierarchy by using the complete set of models and submodels available in the workflow.
- Get valuable insights into the dataset given by the transport code, identifying potential problems and proposing solutions.
- Identify with certainty the effects that need to be studied further, whether a comprehensive linear analysis is sufficient or if a more detailed study is needed, including the non-linear effects.

Several issues with the JET data were known beforehand:

- The $q = 1$ surface is not is not accurately given by the provided equilibria. As cycling sawtooth crashes with a more or less constant $q = 1$ surface have been identified by various diagnostics. Thus, a 1 to 1 mapping between our simulation and the experimental data cannot be expected.
- There are no NBI distribution functions available in the IDS format. For the runs equivalent Maxwellians were used. The density and the pressure as known from the interpretative modelling were used to determine the effective temperature of the EP species.
- The fast hydrogen perpendicular pressure component has known and reported problems i.e. it is not consistently included in the equilibrium reconstruction process (JET data report 19.02.2024).

As before, a broad scan over the scenario was performed using the analytical local model (model 5), tracking the modes with $n = 1$ to $n = 30$ and $m = n - 1$ to $m = n + 3$. The results are shown in Fig.5.17. Approximately 32000 TAEs (odd and even) were tracked over the entire shot taking around 45 minutes to compute (including equilibrium calculations by CHEASE/HELENA). Presently there is no inhert parallelisation across different time points inside the workflow, this can be achieved by running multiple instances of the workflow at the sametime (see subsection 5.7). Leveraging the computational efficiency of the program, an overview of the TAE frequencies and locations (Fig.5.19) can be obtained in a short amount of time. This result can be used to identify the modes of interest for the experiment. In Fig.5.18 where the magnetic perturbations are shown as detected by the Mirnov coils, we can see that there are modes that have roughly constant frequencies, with a small variation in time which corresponds to the data obtained by running the EP-Stability workflow. After 11s, the Alfvén frequency increases (due to density decrease) and the TAE frequency increases. From $k_\perp \rho_{banana_{EP}} \approx 1$ in JET, $n = 2 \ldots 6$ are expected to be the most

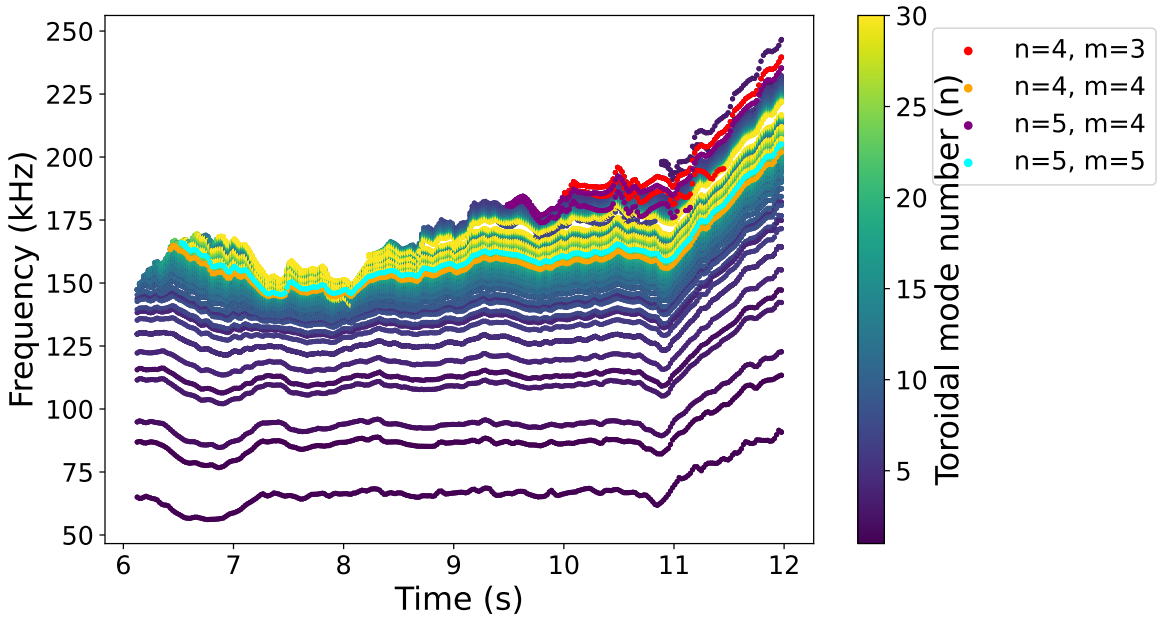

Figure 5.17: Frequencies of modes with toroidal mode number (n) between 1 and 30 tracked over the entire shot. The marked modes are (n,m)=(4,3),(4,4),(5,4),(5,5).

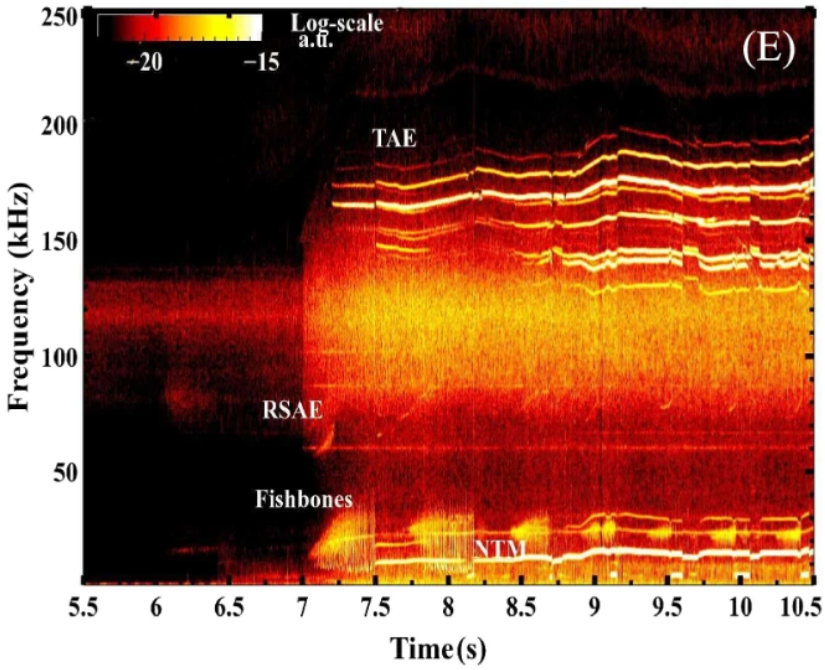

Figure 5.18: (Adapted from Figure 1 [61])Time evolution of magnetic perturbations detected by the Mirnov coils.

unstable modes. We then have to overlay the EP gradient with the gap structure in order to see where unstable modes are expected (in the coming section). In the figures, TAEs $(n, m) = (4, 3), (4, 4), (5, 4), (5, 5)$ are marked. This is a good example of how the workflow can be used to identify the modes of interest for the experiment. The result shows that while the modes $(4, 4)$ and $(5, 5)$ are present throughout the discharge, modes $(4, 3)$ and $(5, 4)$ are only present in the second part of the discharge. After a detailed analysis of the modes, it was found that the modes with $(n, m) = (n, n - 1)$ are not permanently present in the shot. The next step is to see if the modes that are of interest, are not only present but are also found in the region of the highest energetic particle density and pressure gradient.

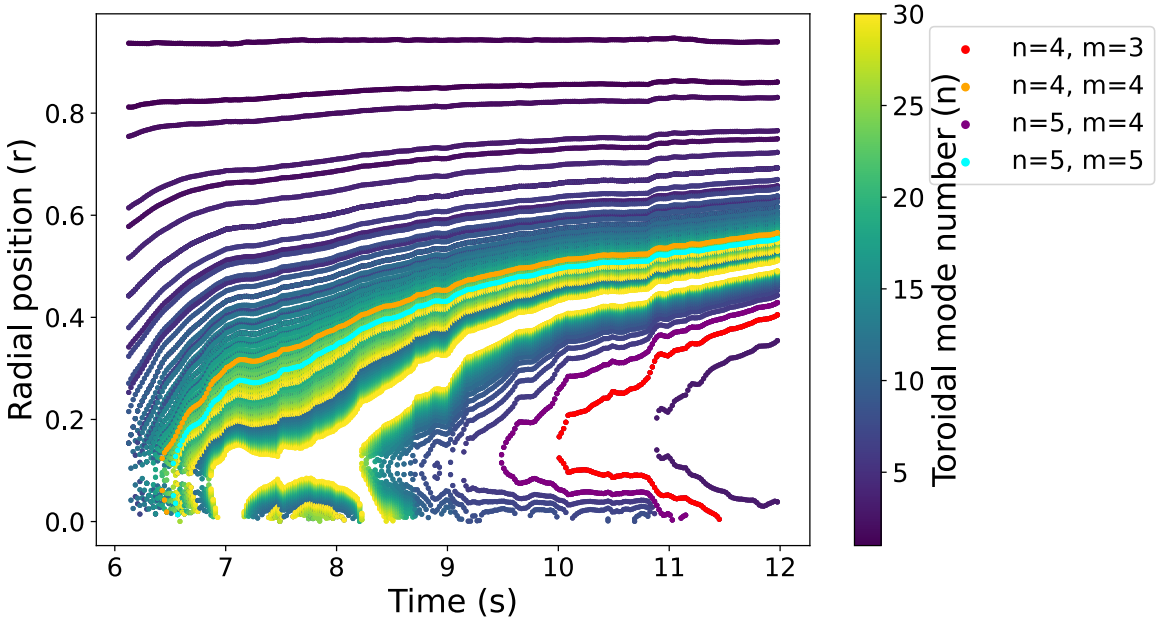

Figure 5.19: Radial location ($r = \sqrt{\text{rho\_pol\_norm}}$) of modes with toroidal mode number (n) between 1 and 30 tracked over the entire shot. The marked modes are (n,m)=(4,3),(4,4),(5,4),(5,5).

In Figure 5.19 the modes are marked with the same colors as in Figure 5.18. The first detail present in the figure is the $q = 1$ surface (white gap) which as the discharge evolves, moves from the core, towards the middle of the plasma. Different branches of the same modes are visible near the core ($(n, m) = (4, 3)$-red and $(n, m) = (5, 4)$-purple), where q-profile is non-monotonic, as seen in the magnetic spectrogram of the JET experiment. The analytical model determines the middle of the gap as the location of the TAE. Radial location of $(n, m) = (4, 4)$(yellow) and $(n, m) = (5, 5)$(light blue) and all other TAEs move radially outwards, away from the steep EP gradient region,

which contradicts the stronger mode activity in the second phase of the discharge as seen in the experiment.

For a more detailed analysis of the modes, the continuum (MHD and Kinetic with and without EPs) was plotted for the toroidal mode number $n = 5$ at $t = 8$s and $t = 9.1$s. The results are shown in Figure 5.21. The mode frequency as given by the refined global solver (model 2) is also marked by triangles for both odd and even modes, with and without EPs. The total density and pressure added for all present fast species, together with their gradients are present. By comparing the two MHD spectra (model 6 - light blue line) for 2 different time-steps in it can be seen that the gap position is not constant but rather changes with time radially outwards, as mentioned before. By employing the kinetic spectrum (model 3) which takes into account the kinetic effects of thermal particles (with blue dots) and the thermal and fast particles (red dots) the gap $(n, m) = (n, n-1)$ first it opens, then it closes as the discharge evolves due to the EPs' density and pressure gradient. Thus, the modes that are present throughout the simulation (of the form $(n, m) = (n, n)$) are not the modes located in the innermost gap. This is due to the inner gaps not always being present, especially when knowing about the wrong movement of $q = 1$ surface radially outwards. The closest modes to the steepest EP gradient region is $(n, m) = (n, n)$ which is located at the edge of the steepest EP gradient region ($r \approx 0.45$). Plotted in the figure are the modes $(n, m) = (5, 5)$ and later in Figure 5.22 the modes $(n, m) = (4, 4)$ together with $(n, m) = (5, 5)$.

A similar behaviour is observed for the modes with $n = 4$ at $t = 8$s and $t = 9.1$s. The difference between the $n = 4$ and $n = 5$ modes is approximately 5 kHz due to the different radial location and thus different Alfvén velocity and q-profile. Because shear increases, the the gap difference is shrinking, in consequence, difference between the locations of the modes is also shrinking.

Before we start looking at the effects of the different EP species on the modes, we first look at the orbit width of the fast species present in the plasma. The result can be seen in Figure 5.20. The orbit width is calculated at the position of the mode $(n, m) = (5, 5)$ tracked at each time-step, to correctly approximate the orbit width of the fast species and their influence on the modes themselves. The formula used to calculate the orbit width is given by:

$$\Delta_b \approx \frac{q_{TAE}\rho_l}{2\sqrt{\epsilon}} \tag{5.1}$$

where q_{TAE} the q-profile value at the TAE position, ρ_l the Larmor radius of the fast species ions $\rho_l = \frac{m_i v_\perp}{eB_{TAE}}$ with $v_\perp$ the velocity of the fast species perpendicular to the magnetic field ($v_\perp = \sqrt{\frac{2E_\perp}{m_i}}$) and $B = B_0(1 - \frac{r_{TAE}}{R})$ the magnetic field at the TAE position. ϵ is the local inverse aspect ratio given by $\epsilon = \frac{r_{TAE}}{R}$. For $E_\perp$ the effective

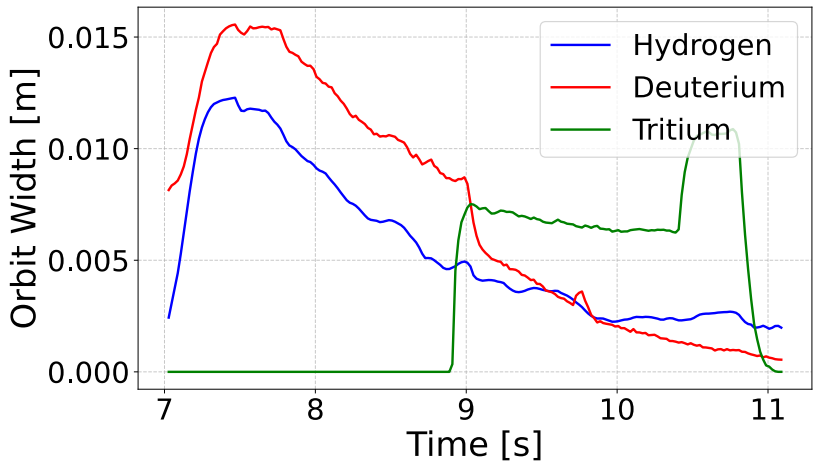

Figure 5.20: Time evolution of the orbit width for Hydrogen, Deuterium and Tritium. This has been calculated at the position of the mode $(n, m) = (5, 5)$.

temperature was used. Because of this, a drop in the orbit width of the fast species is present as modes move radially outwards (i.e. T becomes smaller). The orbit width for the Hydrogen and Deuterium is of particular interest as they are the main drivers of the modes. The Tritium, as will be seen later, does not drive the modes unstable. Looking at the figure one can see that the orbit widths decrease as the discharge evolves, this is due to the change in position of the modes, they move from the region with high fast particle density/pressure gradients, to the region with smaller gradients. This in turn is due to the shift in the q-profile, specifically $q = 1$ surface. As mentioned before, in Figure 5.19 the $q = 1$ surface has a visible shift towards the center of the plasma, away from the core, where one would expect the drive to be the strongest. A bump in the orbit width of the Tritium can be seen between 10.5 and 11s, this corresponds to the starting of the second tritium NBI beam, leading to a high effective T and thus larger ρ_l.

The modes of interest are identified as $(n, m) = (n, n)$. We start by looking at the frequency and growth rate of the modes without energetic particles. For clarity we start with the even mode $(n, m) = (5, 5)$ and the results are shown in Figure 5.23 for frequency and Figure 5.24 for growth rate. The same color scheme is kept for both figures:

- blue: analytical middle of the TAE gap (model 5)
- orange: local kinetic model: top of kinetic continuum (model 4)
- green: global kinetic solution; as expected between the top of the continuum and the middle of the TAE gap (model 1)

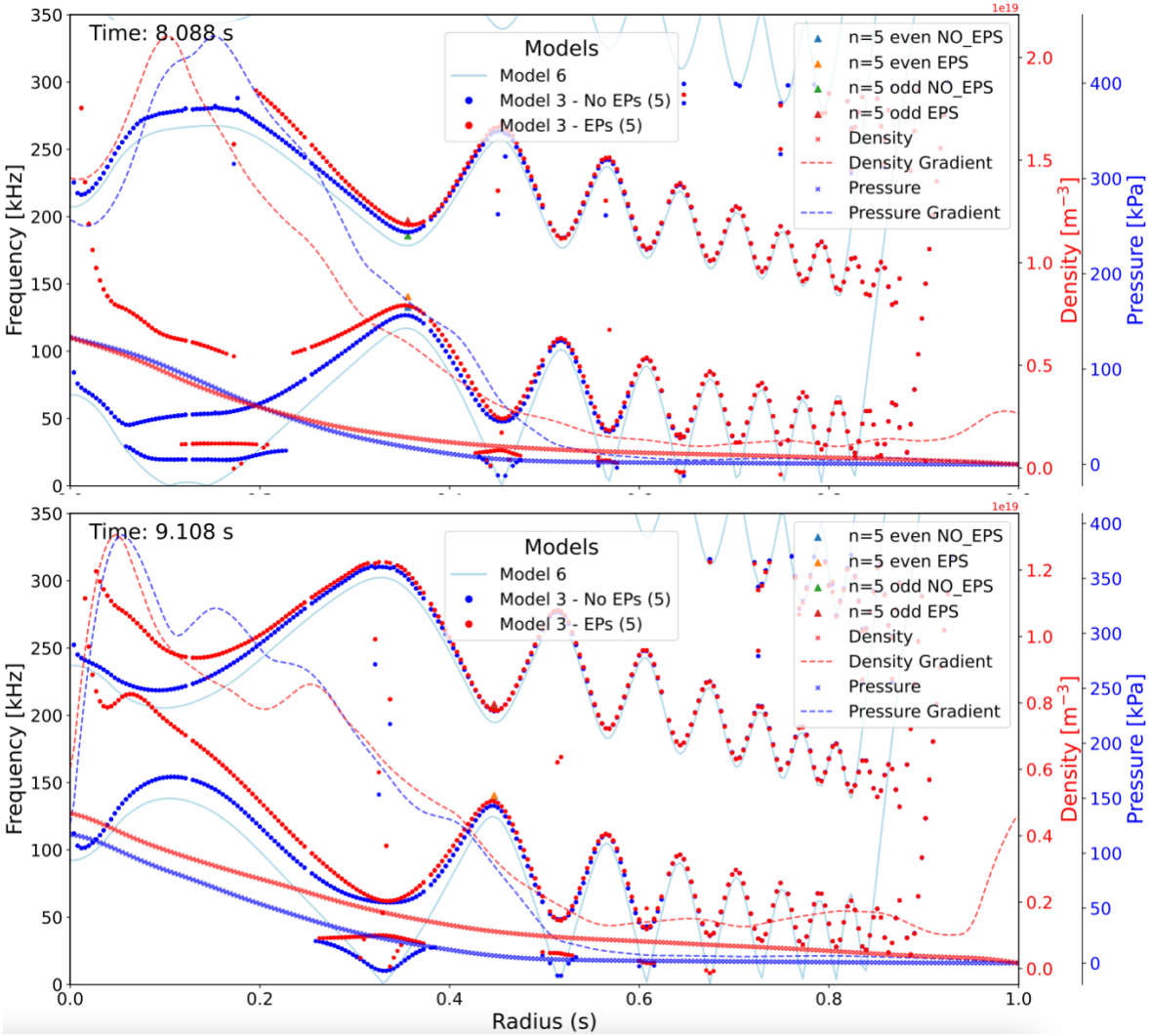

Figure 5.21: Continuum given by MHD - model 6 and kinetic - model 3 for $(n, m) = (5, 5)$ at $t = 8$ and $t = 9.1$s. Mode frequency is also marked by triangles for both odd and even modes, with and without EPs. The total density and pressure added for all present fast species, together with their gradients are present.

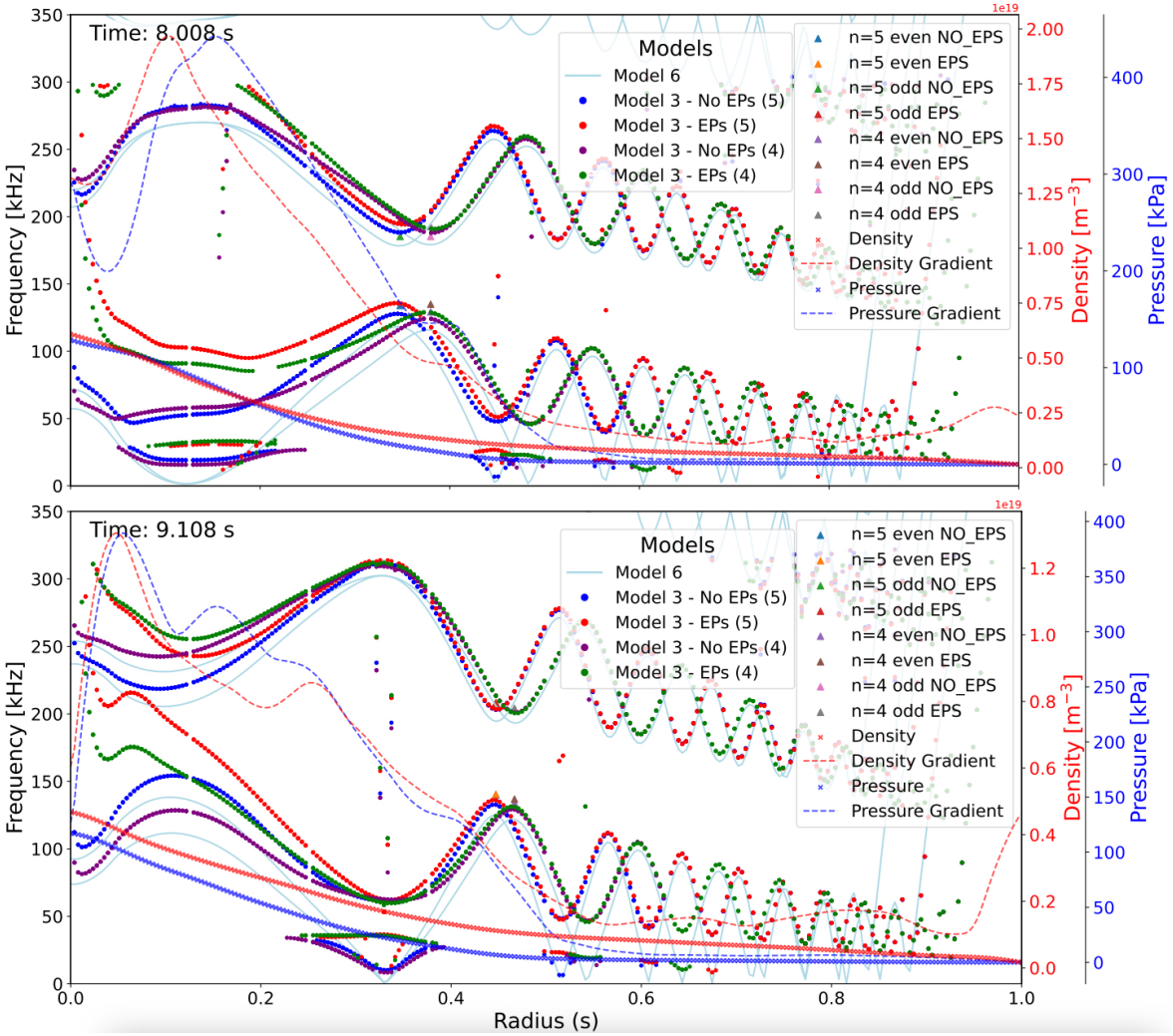

Figure 5.22: Continuum given by MHD - model 6 and kinetic - model 3 for $(n, m) = (5, 5)$ and $(n, m) = (4, 4)$ at $t = 8.008$s (top) and $t = 9.108$s (bottom). Mode frequency is also marked by triangles for both odd and even modes, with and without EPs. The total density and pressure added for all present fast species, together with their gradients are present.

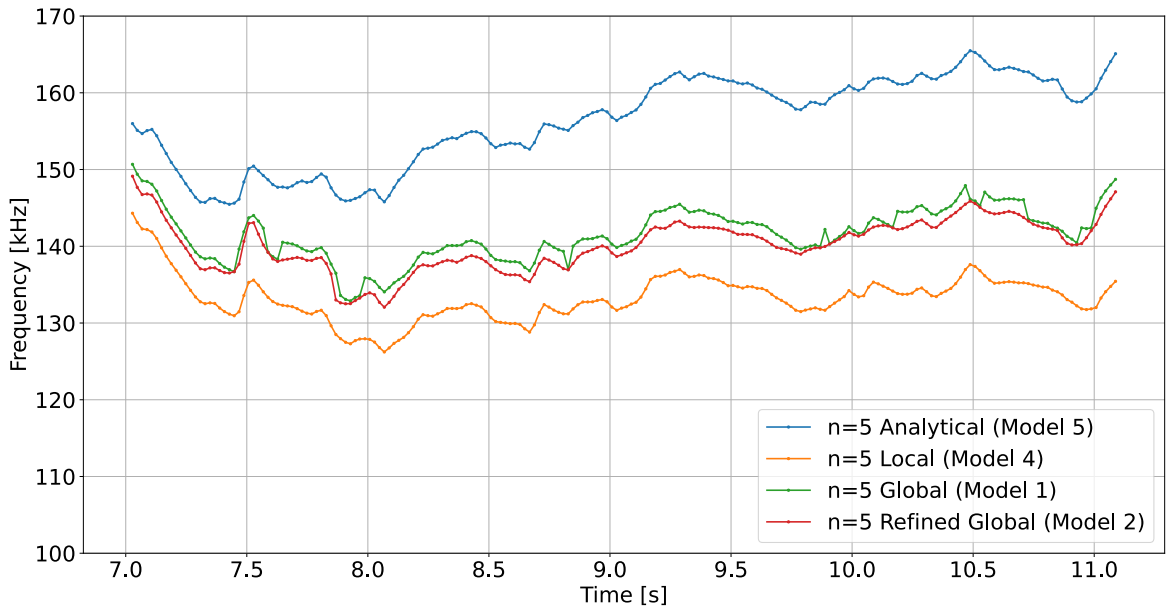

Figure 5.23: Time evolution of mode frequency for $(n, m) = (5, 5)$ in the JET discharge for different computational models.

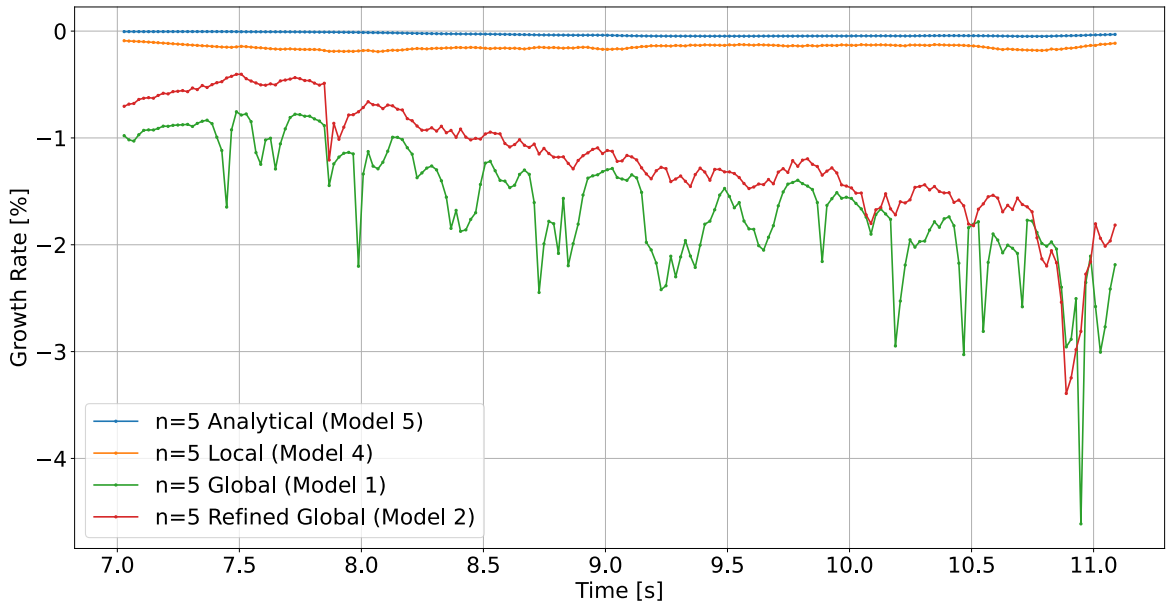

Figure 5.24: Time evolution of mode growth rate for $(n, m) = (5, 5)$ in the JET discharge for different computational models.

- red: refined global kinetic solution (model 2)

Landau and Radiative damping are captured by the analytical model, but not accurately in this case, demonstrating that non-local damping effects are dominating the damping. That means that the local kinetic model (model 4), while more accurate than model 5, cannot describe these non-local damping mechanisms. Therefore, the global kinetic model is needed to capture all relevant damping mechanisms. Global (model 1) and refined global (model 2) are run in sequence following the "overview" (model 1) and refinement (model 2) logic discussed in chapter 3.2.1. Without taking EPs into account we can see, and expect, that the mode is stable. This analysis was also performed for $(n, m) = (2, 2), (3, 3), (4, 4), (6, 6)$ odd and even modes, and the results were similar. From this point forward, all the runs are performed using the refined global solver using the '5-4-1-2' setting in the workflow for the final and most accurate model 2 result. In the next sections we will look at the effects of the different EP species on the even and odd TAEs. Before that, several effects are present in the results that follow which are worth mentioning:

1. Mode frequency/growthrate sudden changes due to profile changes, in particular sawtooth crashes, which are present throughout the discharge. These effects can be directly compared with the experimental data.

2. LIGKA model enforces quasi-neutrality and thus, when taking EPs into account, the densities of thermal species is partly replace by the fast density of the specific ion. However, in several instances (Hydrogen and Helium) this is not possible due to small thermal population, and such the 'default' setting for the code is to reduce the Tritium thermal density instead. This leads to modification in densities which in turn leads to a modification in the mode frequency. Whenever this effect is present it will be mentioned.

3. Numerical problems with the solver that finds Energetic Particle Modes (EPMs) or modes in other gaps. These modes may not always be wrong, but do not belong to the same branch leading to sudden 'spikes' that do not correspond to the experimental data. They can be quickly identified by looking at the global mode structure. This can fixed by manual runs at specific time points (with adjusted settings of the solver) or by adjusting the global settings and rerunning the whole discharge. We chose not to remove all of these inconsistent modes, as we want to demonstrate to what extent the standard settings of the workflow are able to recover the correct solutions.

5.4.1 EPs' effects on the $(n, m) = (5, 5)$ even TAE

Now one by one we will look at the effects of the different EP species (D,H,T and He^4) on the $(n, m) = (5, 5)$ even TAE.

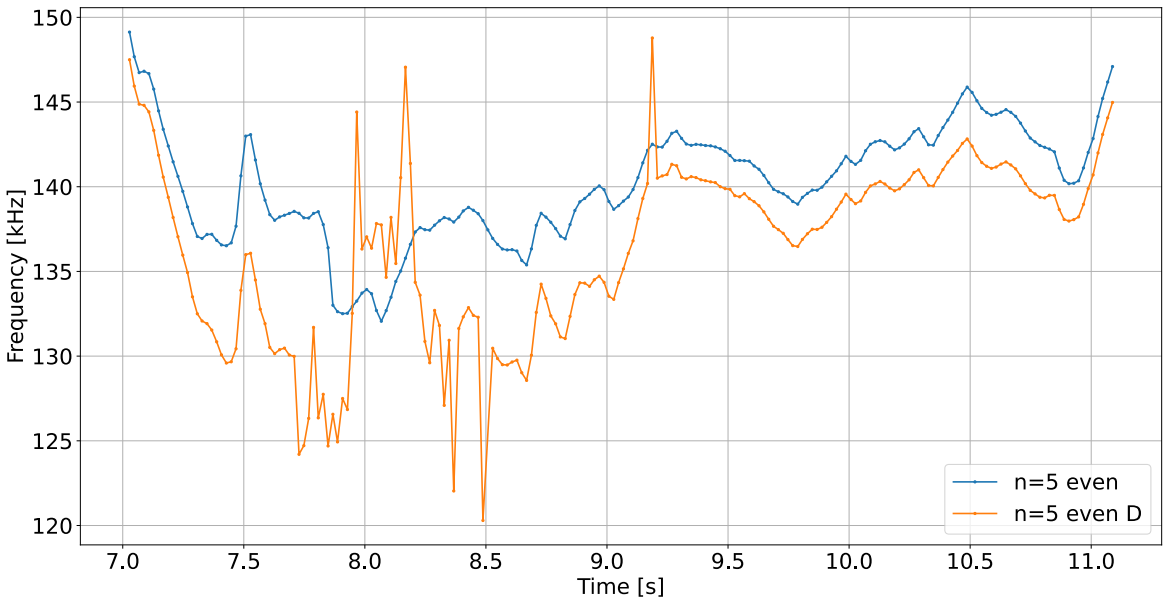

Figure 5.25: Time evolution of $(n, m) = (5, 5)$ frequency without EPs (blue) and with EPs - D only (orange) in the JET discharge.

Starting with the Deuterium, in Figures 5.25 and 5.26 the frequency and growth rate are shown by comparing the previous results without EPs (blue) with the one where only Deuterium is taken into account as an EP species (orange) (all the thermal species remain in the calculation). When looking at the frequency of the mode, a constant down shift in frequency throughout the discharge can be seen when taking EPs into account, as expected [71, 72]. Energetic particles contribute via a kinetic term to the dispersion relation that alters both the real and imaginary parts of the mode frequency. The free energy associated with the energetic particle pressure drives the mode unstable, and in doing so, the resonant interaction tends to lower the phase velocity of the wave [73]. This shift is larger in the first half of the shot, as the Deuterium beam is switched off afterwards (> 9s), leading to a lower energetic particle density and pressure gradient. This can be seen in the growth rate graph, where the mode is unstable as the deuterium beam is switched on, and stable after a while as the deuterium beam is switched off.

Particularities in the graphs can be seen for frequency between $7.9 - 8.3$s, where there is a sudden shift in frequency, due to the sawtooth crash present at that exact time, see Figure 4.12 (the sawtooth crash at $7.9 - 8.3$s). The shift in frequency can also

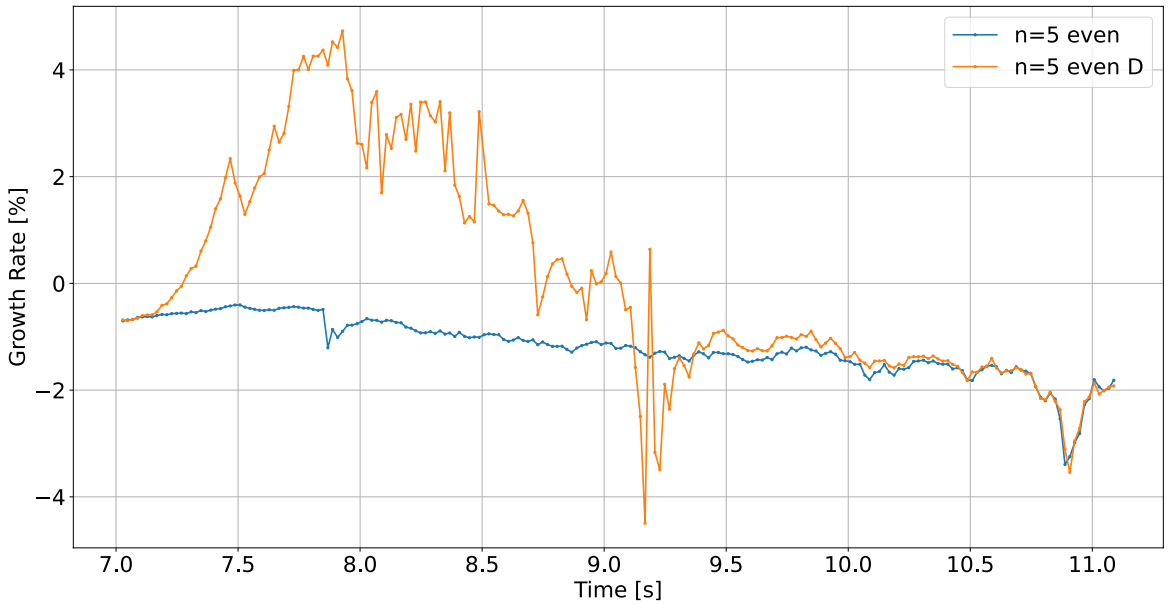

Figure 5.26: Time evolution of $(n, m) = (5, 5)$ growth rate without EPs (blue) and with EPs - D only (orange) in the JET discharge.

be noticed in the magnetic measurements directly from the experiment (Figure 5.18). Concerning the damping (figure 5.26), the growth rate has sudden shifts in the region of $9.1 - 9.3$s, due to the ICRF heating drop suddenly at that time (figure 4.8). This effect can be seen more clearly in the frequency, which jumps to approximately 148 kHz at 9.19s. This corresponds to the sawtooth crash in the experiment (Figure 4.12), and again corresponds to the magnetic measurements from the experiment (Figure 5.18).

A similar analysis was performed for the Hydrogen, the results are shown in Figure 5.27 and 5.28. While a shift in the frequency is present, the effect is not as large as the one present for the Deuterium. This is due to the quasi-neutrality assumption present in the LIGKA model (explained before). The particularity in this case is that the density of the fast Hydrogen is larger than the background Hydrogen because of this, part of the background Tritium is replaced by fast Hydrogen. This leads to a decrease in density and thus a higher v_A, which in turn leads to a higher frequency of the mode. In the first part of the discharge (<9s) this leads to a lower difference between the frequency with and without EPs, compared to the Deuterium case. This is also due to the drive being higher for Hydrogen in the first part of the discharge. This effect is more pronounced in the second part of the discharge after the Tritium beam is switched on, leading to a higher frequency of the mode when fast Hydrogen is taken into account compared to the Deuterium and no EPs case.

From the growth rate, it can be seen that while the mode is stable without EPs, it

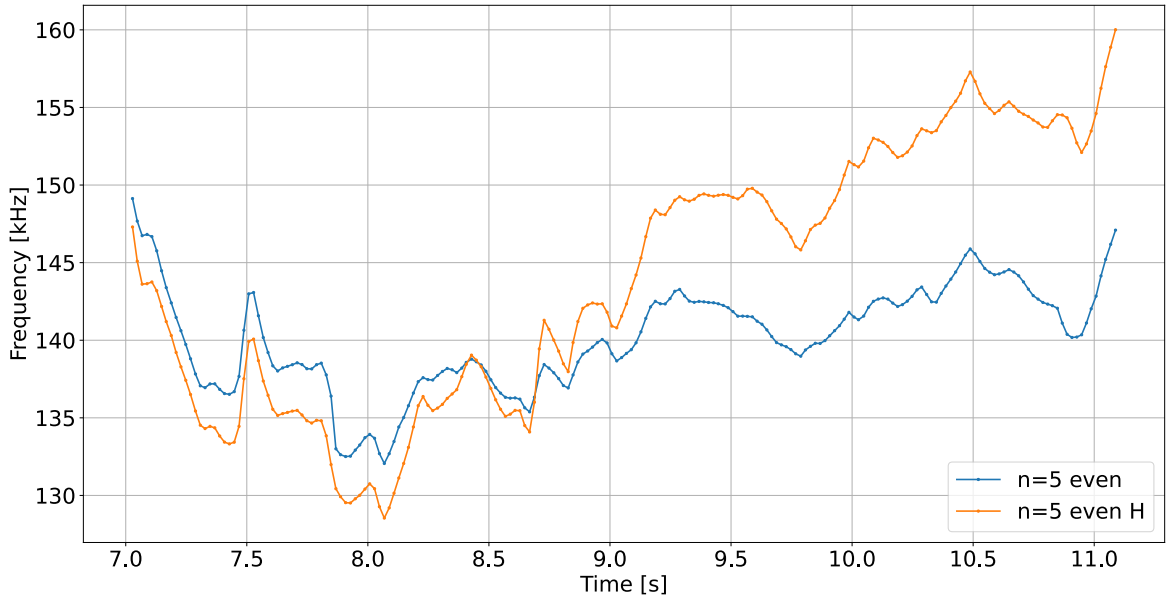

Figure 5.27: Time evolution of $(n, m) = (5, 5)$ frequency without EPs (blue) and with EPs - H only (orange) in the JET discharge.

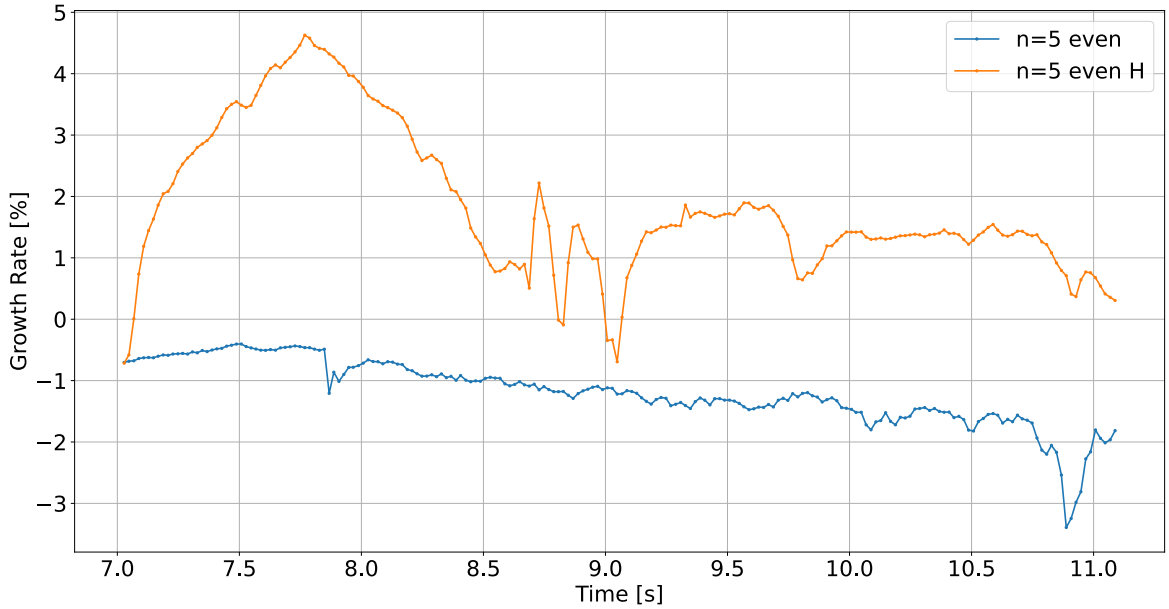

Figure 5.28: Time evolution of $(n, m) = (5, 5)$ growth rate without EPs (blue) and with EPs - H only (orange) in the JET discharge.

becomes unstable when Hydrogen is present. The growth rate is peaking at around 7.8s, at 4.5%. Peculiarities in the growth rate for the Hydrogen case can be seen in the region of $8.5 - 9.1$s, where the growth rate has sudden shifts. This is due to the ICRF drop right after 9s (lowered growth rate) and the Deuterium beam being ramped up two times in that interval, leading to a higher density of Deuterium and thus a lower drive for the mode in the case of Hydrogen EPs (see Figure 4.8).

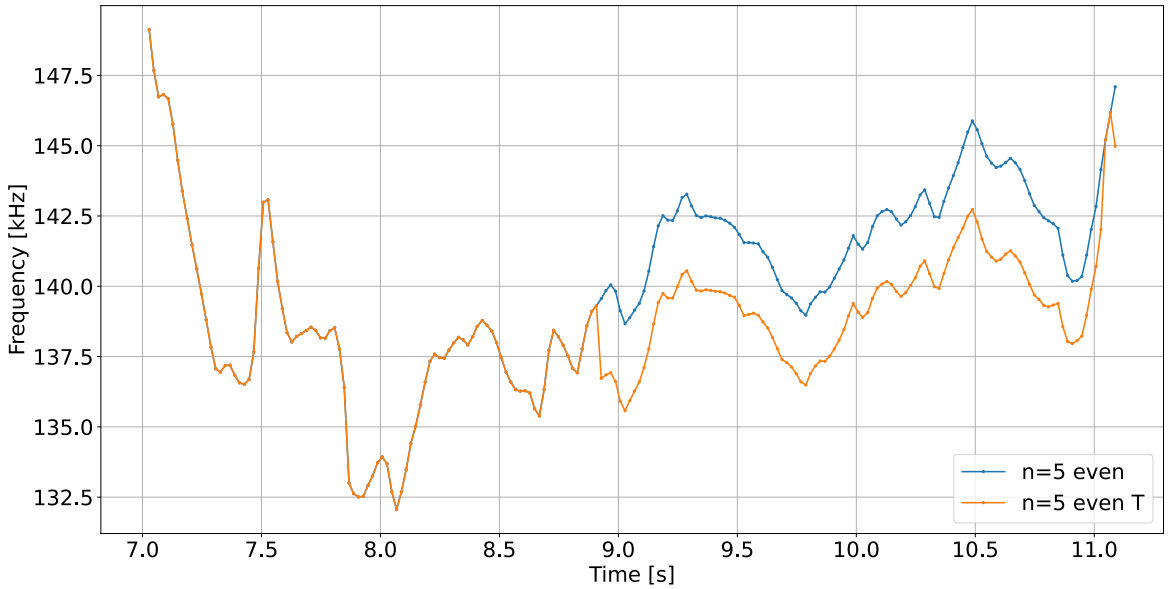

Figure 5.29: Time evolution of $(n, m) = (5, 5)$ frequency without EPs (blue) and with EPs - T only (orange) in the JET discharge.

For Tritium, the results are shown in Figure 5.29 and 5.30. The frequency of the mode is affected by the presence of Tritium, starting via NBI after 9s. The frequency as expected is slightly lower than the one without EPs. The growth rate is also affected by the presence of Tritium, but the effect is small compared with that of Deuterium. Under the current form of analysis (Maxwellian distribution, FOW effects are included in the LIGKA model, but in the passing particle limit i.e. EP species as mainly trapped particles drive the mode, FOW are underestimated effects explained in the next subchapter) Tritium does not drive the mode unstable, on the contrary, it seems to have a stabilizing effect. This aligns with the experience that at JET NBI beams are typically damping TAEs [74] and ICRH is needed to drive TAEs unstable. Lower drive for Tritium is also due to the radially outwards movement of the mode, away from EP drive by the time the Tritium beam is switched on (>9s).

The frequency of the mode when alpha particles are included is downshifted due to the quasineutrality condition imposed by LIGKA. In this case, because the helium

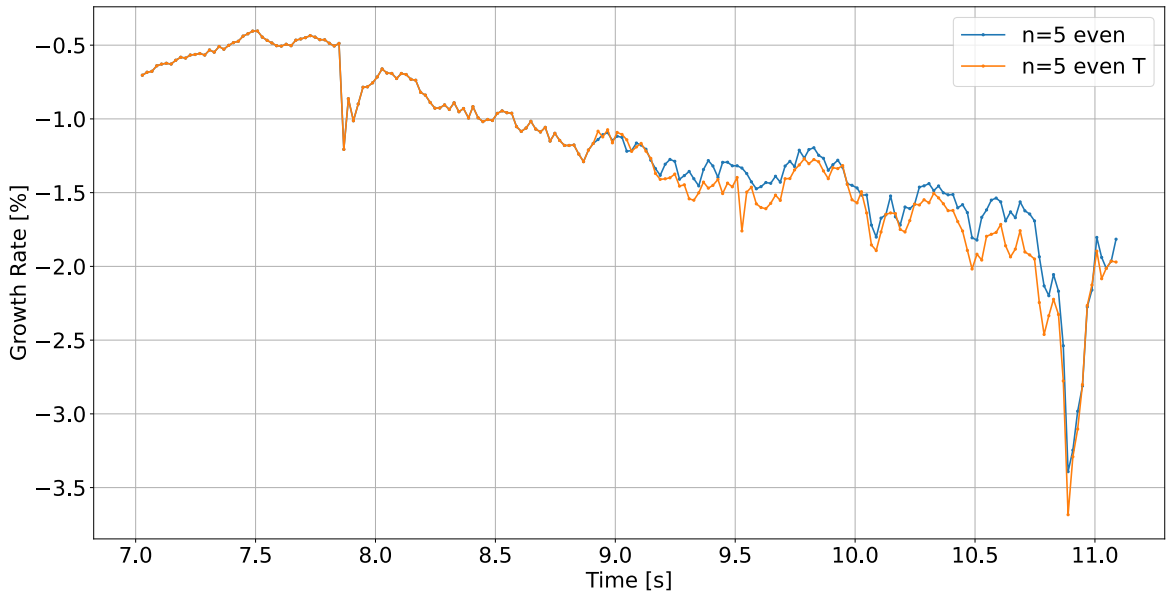

Figure 5.30: Time evolution of $(n, m) = (5, 5)$ growth rate without EPs (blue) and with EPs - T only (orange) in the JET discharge.

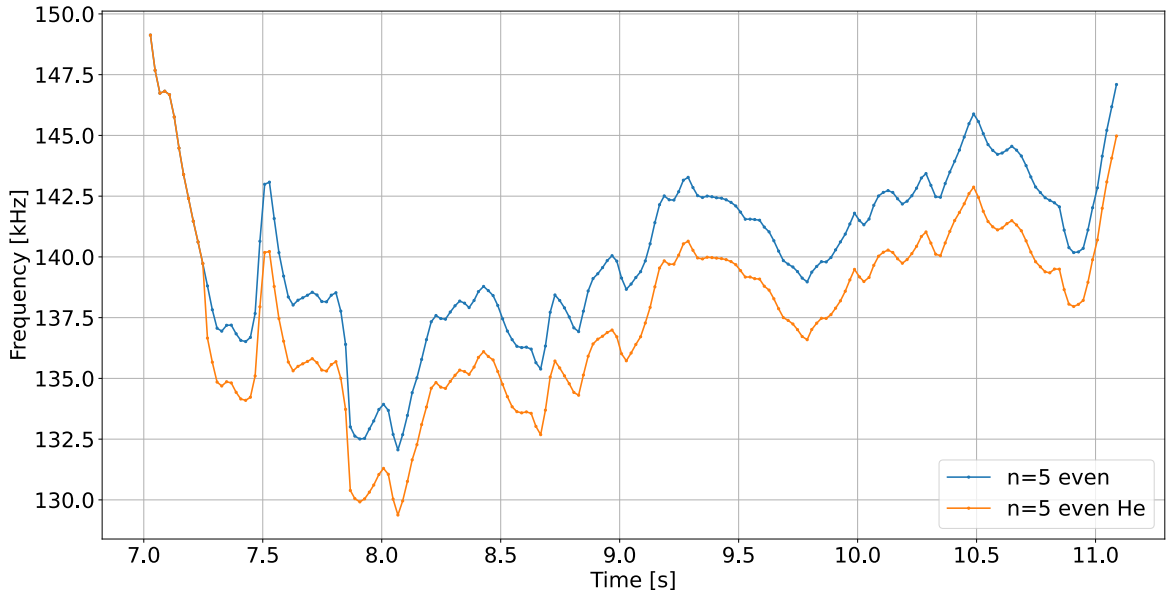

Figure 5.31: Time evolution of $(n, m) = (5, 5)$ frequency without EPs (blue) and with EPs - He only (orange) in the JET discharge.

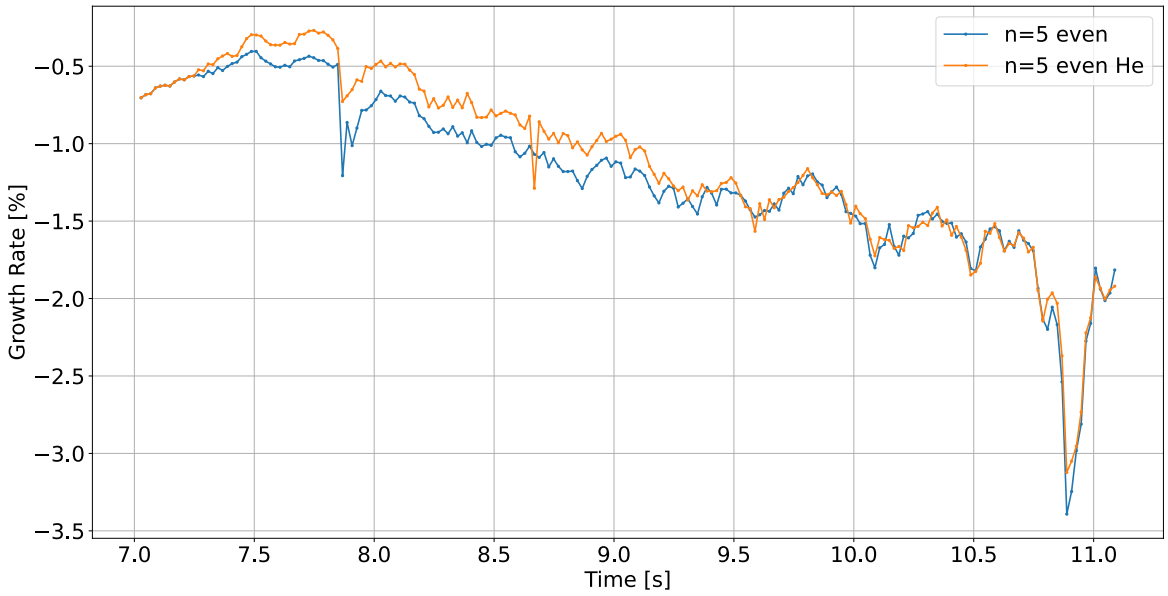

Figure 5.32: Time evolution of $(n, m) = (5, 5)$ growth rate without EPs (blue) and with EPs - He only (orange) in the JET discharge.

ash had a very small density, part of the thermal Tritium was replaced by the fast Helium. This, as before leads to a higher density, thus a lower v_A and in consequence a lower frequency of the mode. Due to low density and pressure of the fast Helium ions (10x lower P_{fus} see 4.8), the effect on the $(n, m) = (5, 5)$ mode is not large enough to destabilise TAEs. This effect is the most pronounced in the interval of approximately $7.5 - 9.5$s, after which the contribution from the Helium ions is negligible (P_{fus} is starting to decrease) as the mode is moving radially outwards from the EP drive.

Now that the individual effects of the different fast species on the mode have been studied, we can look at the total effect of all the species present in the plasma. The results are shown in Figure 5.33 and 5.34 for the $(n, m) = (5, 5)$ even mode. Here we take two approaches: first we run the workflow with all fast species present, and then we use the previously obtained results for each EP species to add up to the total contribution.

One can see that, as expected, the mode frequency in the first part of the discharge is lower than the one without EPs. An exception is the $7.9 - 8.3$s, interval which can be seen in the experiment also and could be due to the sawtooth crash present in that interval. However, the peak ($t = 7.9$s) is a numerical problem that is expected when $\gamma > 10\%$, as then the antenna oscillator model starts to become unreliable using the standard settings. Manual settings can remove this issue. Also, it is expected if the trapped particle finite orbit width would be included (section 5.5) this problem

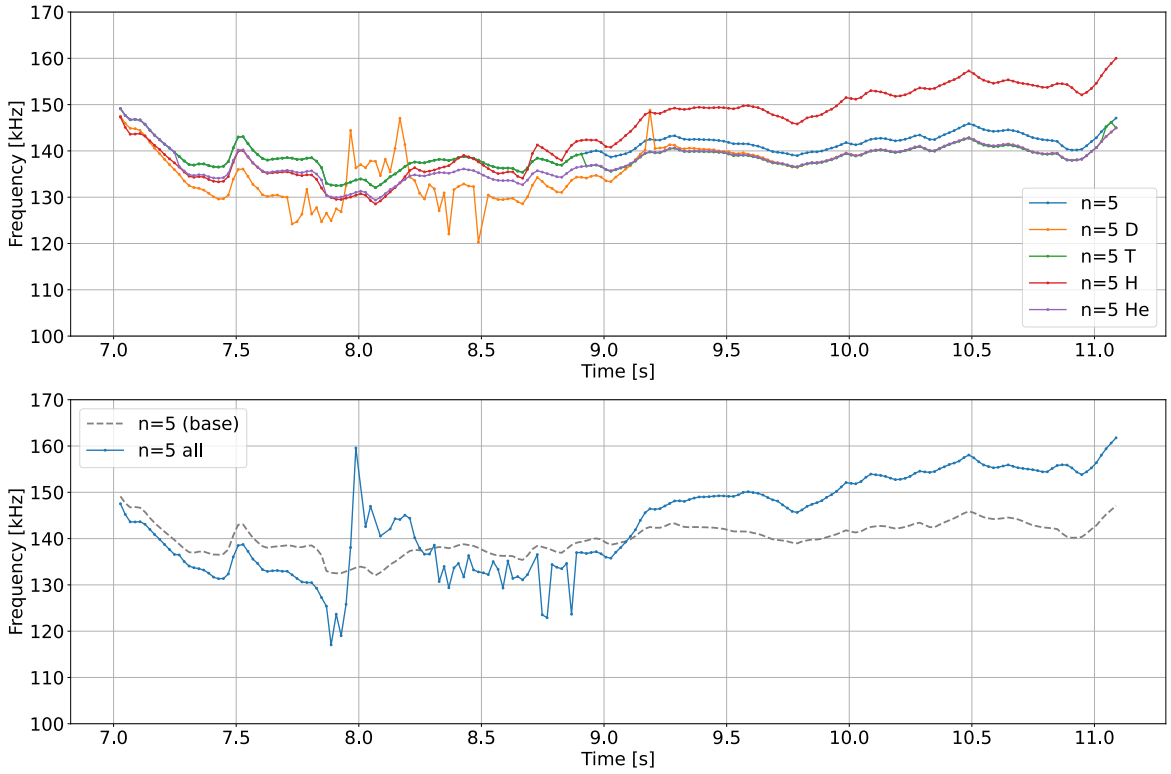

Figure 5.33: Time evolution of $(n, m) = (5, 5)$ frequency (top) for each fast species present in the plasma showing the contribution of each species to the mode frequency: blue line is without EPs (base), and the rest denote each species. The bottom plot shows the mode frequency with all species present (blue) and the base (grey dotted line) with no EPs present.

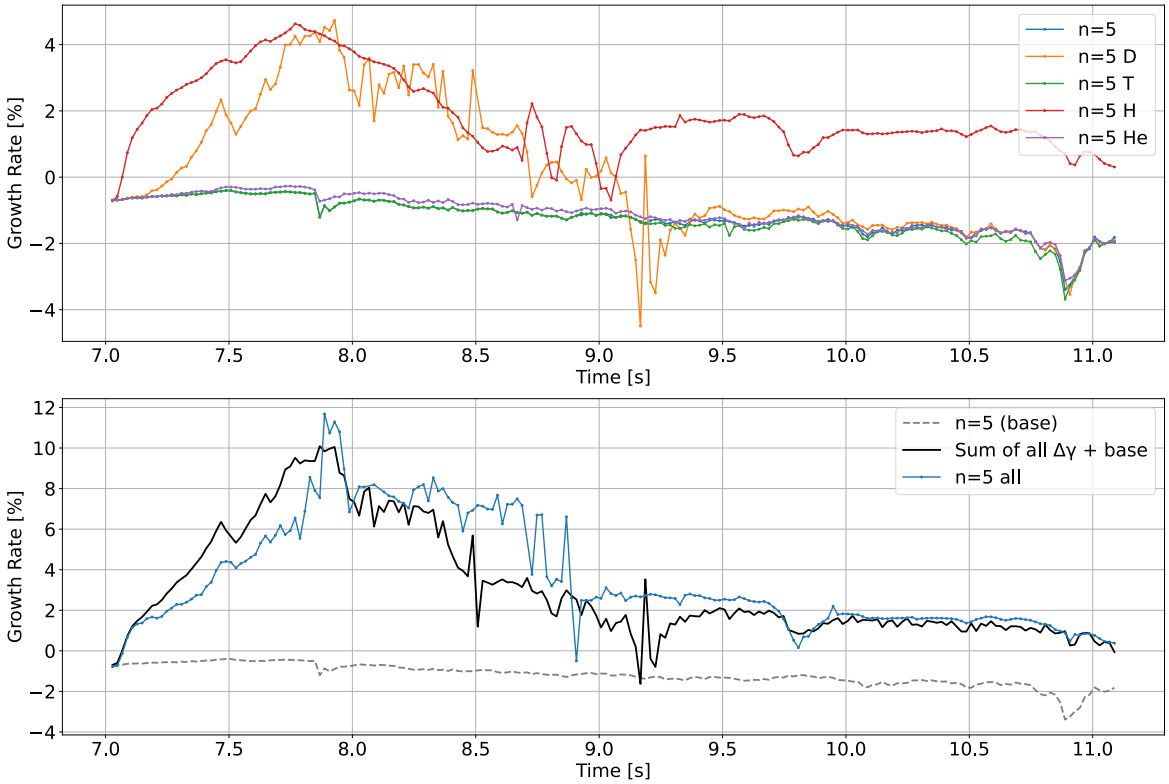

Figure 5.34: Time evolution of $(n, m) = (5, 5)$ growth rate (top) for each fast species present in the plasma demonstrating the contribution of each species to the mode growth rate: blue line is without EPs (base), and the rest denote each species. The bottom plot shows the mode growth rate with all species present (blue) and the sum of all the contributions (black) added to the base(grey dotted line).

would not persist. Afterwards, the mode frequency is higher than the one without EPs, this, as explained before, comes from the quasi-neutrality assumption present in the model. Concerning the growth rate, the mode is strongly driven by the fast species present in the plasma, with Deuterium and Hydrogen having the largest contributions. The strongest drive is present earlier into the discharge due to several factors such as: location of modes closer to the core ($q = 1$ surface moves radially outwards) where high fast particle density/pressure is present, P_{NBI} heating peaking (see Figure 4.8) at the beginning of the discharge ($7.7 - 7.9$s) which injects the fast Deuterium ions, and the ICRF heating which accelerates the Hydrogen and Deuterium fast ions.

For a linear model, we expect that the sum of growth rates of individual runs with different EP species add up to growth rate of the run with all species present. However, non-perturbative effects and shifts of v_A for maintaining quasineutrality lead to small differences at some time points. As the damping and drive depend on the frequency of the TAE, we cannot expect exact additivity. Clear deviations (up to factor 2) can be observed in fig 5.34 showing that the simultaneous presence of all EP species can lead to substantial non-perturbative effects.

5.4.2 EPs' effects on $(n, m) = (4, 4), (6, 6)$ even TAE

The same overall analysis was performed also for the $(n, m) = (4, 4)$ and $(6, 6)$. In the $n = 4$ case, the results are in the Figure 5.35 for frequency and Figure 5.36 for growth rate. As before, the upper part of the graphs illustrates the individual contributions from each fast species present in the plasma, while the lower part shows the sum of these contributions along with a separate run incorporating all four EPs. The overall behavior remains consistent with the previous case, with the notable distinction that the frequency is generally lower compared to the $n = 5$ case, as expected (TAE frequency lower for $r_n = 4 > r_n = 5$). One minor difference is that the frequency shift (when frequency with EPs becomes larger than without) happens earlier (8.7s compared to 9s). This further supports the reasoning behind this effect. A shift can be seen in fig. 5.22, the mode $(n, m) = (4, 4)$ is located slightly radially outwards compared to the previously analysed $(n, m) = (5, 5)$ mode. The contributions remain the same as, in big part, the drive comes from Deuterium and Hydrogen.

In the $n = 6$ case, the results are in the Figure 5.37 for frequency and Figure 5.38 for growth rate. In the same way as before, the top of the graphs represent the individual contributions from each fast species present in the plasma, while the bottom the sum of individual contributions and a separate run including all 4 EP species. In this case the exact same overall behaviour is observed, as in the previous case, with the mention that the frequency is overall increased compared to the $n = 5$ case, which is expected.

One minor difference is that the frequency shift (with EPs larger than without)

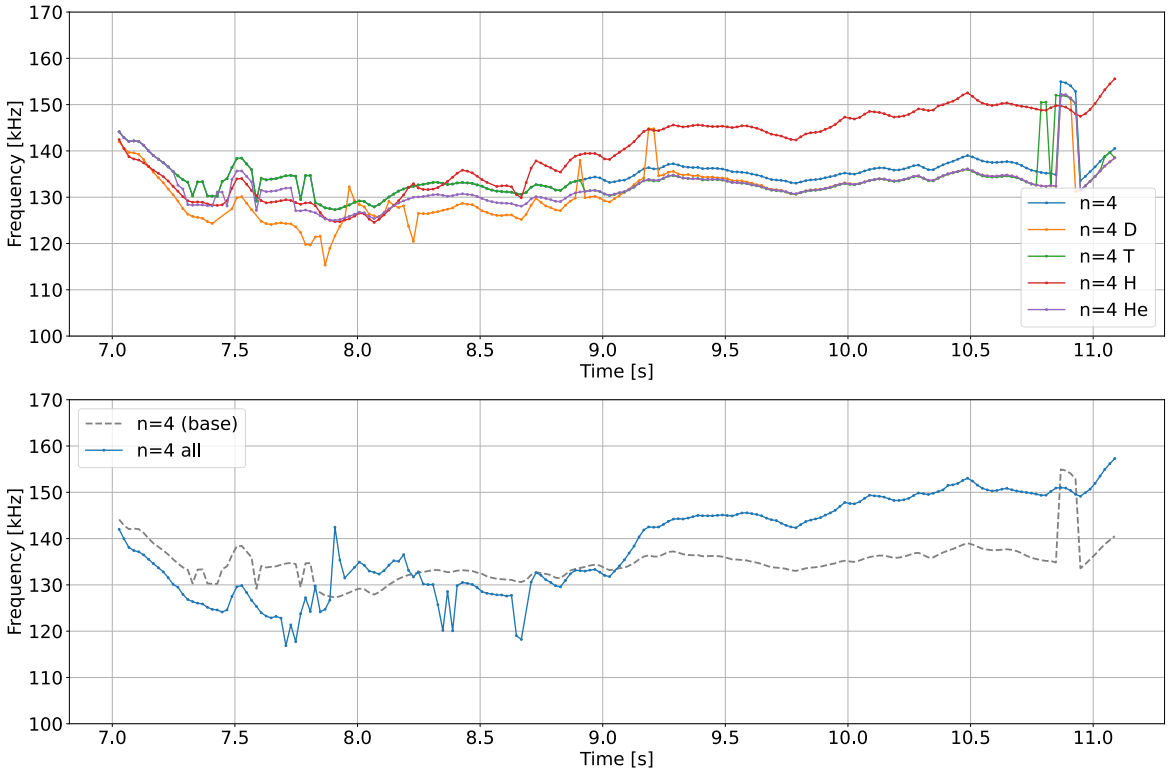

Figure 5.35: Time evolution of $(n, m) = (4, 4)$ frequency (top) for each fast species present in the plasma showing the contribution of each species to the mode frequency: blue line is without EPs (base), and the rest denote each species. The bottom plot shows the mode frequency with all species present (blue) and the base (grey dotted line) with no EPs present.

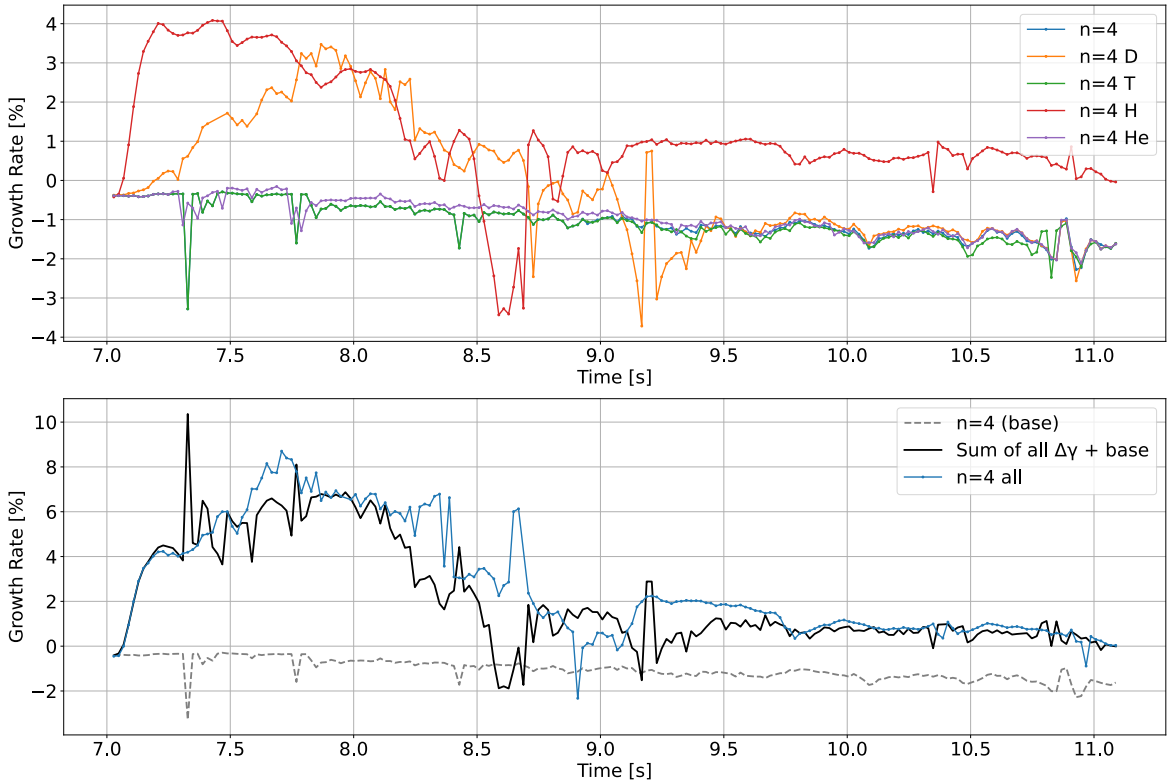

Figure 5.36: Time evolution of $(n, m) = (4, 4)$ growth rate (top) for each fast species present in the plasma showing the contribution of each species to the mode growth rate: blue line is without EPs (base), and the rest denote each species. The bottom plot shows the mode growth rate with all species present (blue) and the sum of all the contributions (black) added to the base (grey dotted line).

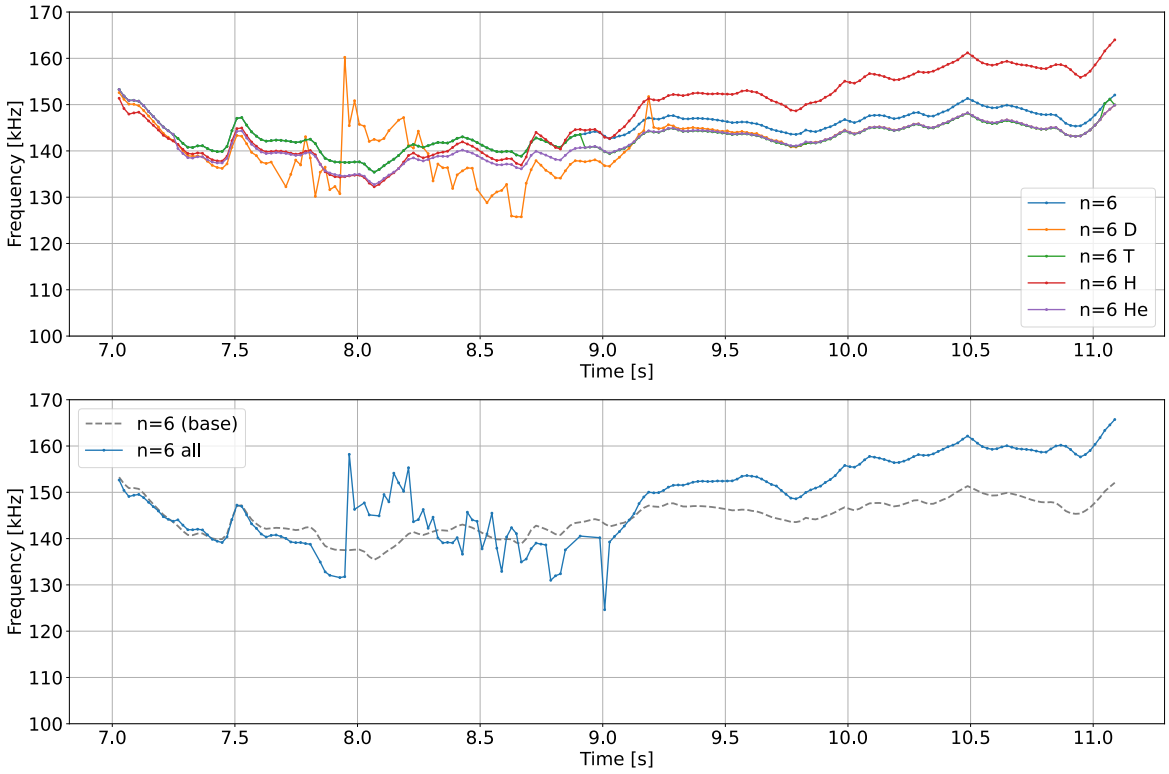

Figure 5.37: Time evolution of $(n, m) = (6, 6)$ frequency (top) for each fast species present in the plasma showing the contribution of each species to the mode frequency: blue line is without EPs (base), and the rest denote each species. The bottom plot shows the mode frequency with all species present (blue) and the base (grey dotted line) with no EPs present.

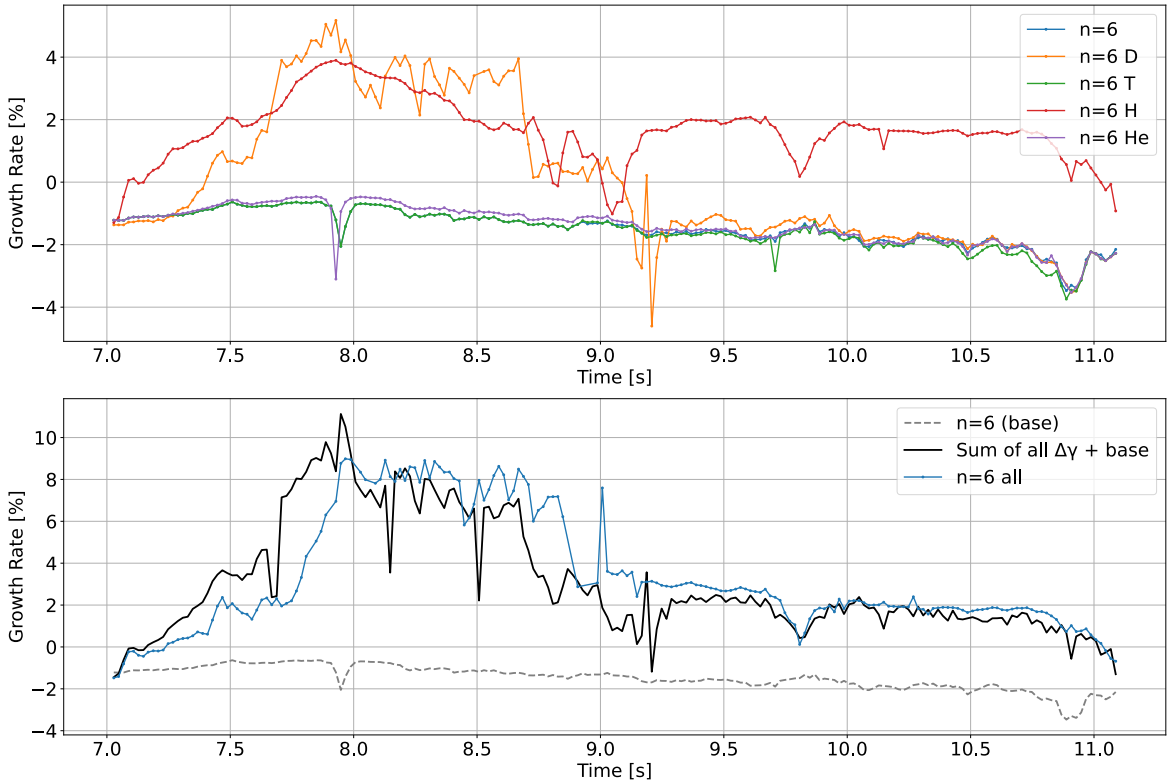

Figure 5.38: Time evolution of $(n, m) = (6, 6)$ growth rate (top) for each fast species present in the plasma showing the contribution of each species to the mode growth rate: blue line is without EPs (base), and the rest denote each species. The bottom plot shows the mode growth rate with all species present (blue) and the sum of all the contributions (black) added to the base (grey dotted line).

happens later (>9.1s compared to 9s). This result is different, because, at least intuitively, one would expect the shift to happen even later (comparable to the difference between $n = 4$ and $n = 5$). By extrapolating the results for $n = 4, 5$ in fig. 5.22, the mode $(n, m) = (6, 6)$ is located slightly radially inwards compared to the previously analysed $(n, m) = (5, 5)$ mode. This indicates that fast particles provide stronger drive for this mode, leading to a greater frequency offset, meaning the frequency shift occurs later. The growth rate of this mode is generally higher in the $t > 9$s region,while following the same overall trend as in the $n = 5$ case. However, unlike the previously analysed scenario, the peak growth rate between $t = 7.7 - 8$s is lower than that observed for the $n = 5$ case. The primary contributions remain largely unchanged, with the dominant drive originating from Deuterium and Hydrogen.

5.4.3 EPs' effects on odd TAE

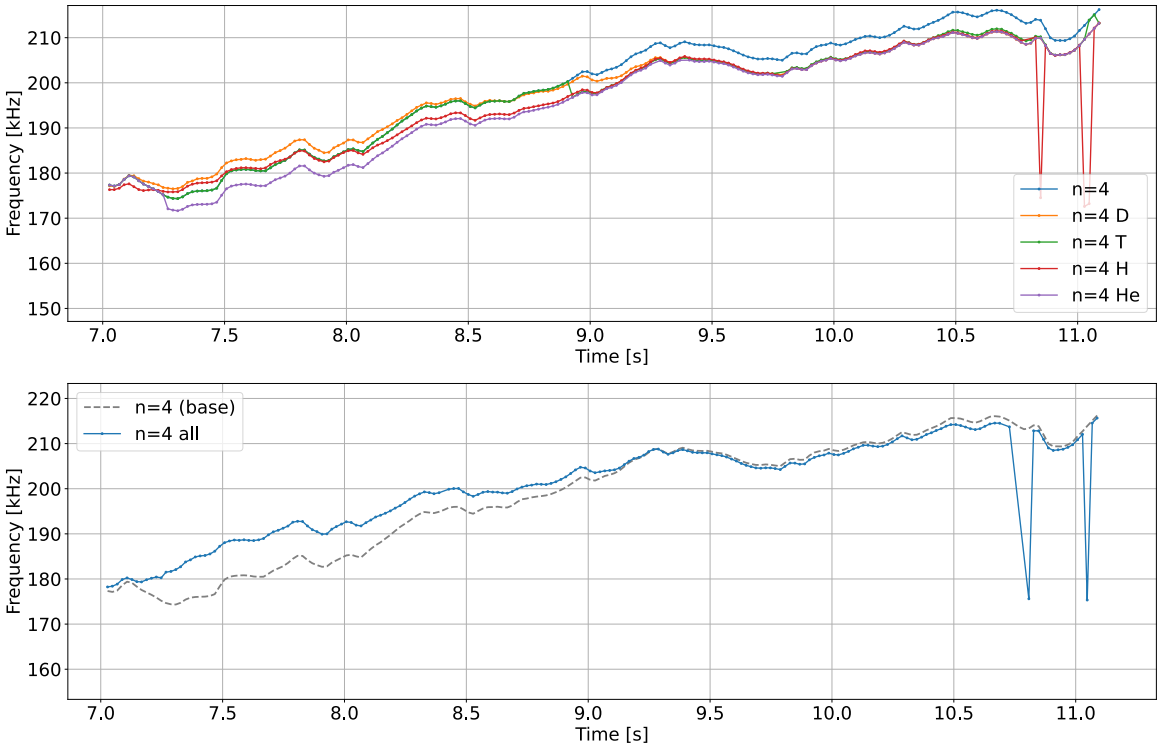

Figure 5.39: Time evolution of $(n, m) = (4, 4)$ odd mode frequency (top) for each fast species present in the plasma showing the contribution of each species to the mode frequency: blue line is without EPs (base), and the rest denote each species. The bottom plot shows the mode frequency with all species present (blue) and the base (grey dotted line) with no EPs present. Spikes in the frequency are explained in the text.

While the thesis focuses on the even TAE modes, the odd ones were also looked at in the JET experimental data as we wanted to test if their frequency would match the experimentally observed ones (as assumed in [61] using FAR3D). The mode numbers are the same as before, with modes $(n, m) = (4, 4), (5, 5)$. They stay close to the top of the continuum gap (Figures 5.21, 5.22) and thus have a higher frequency than the even modes.

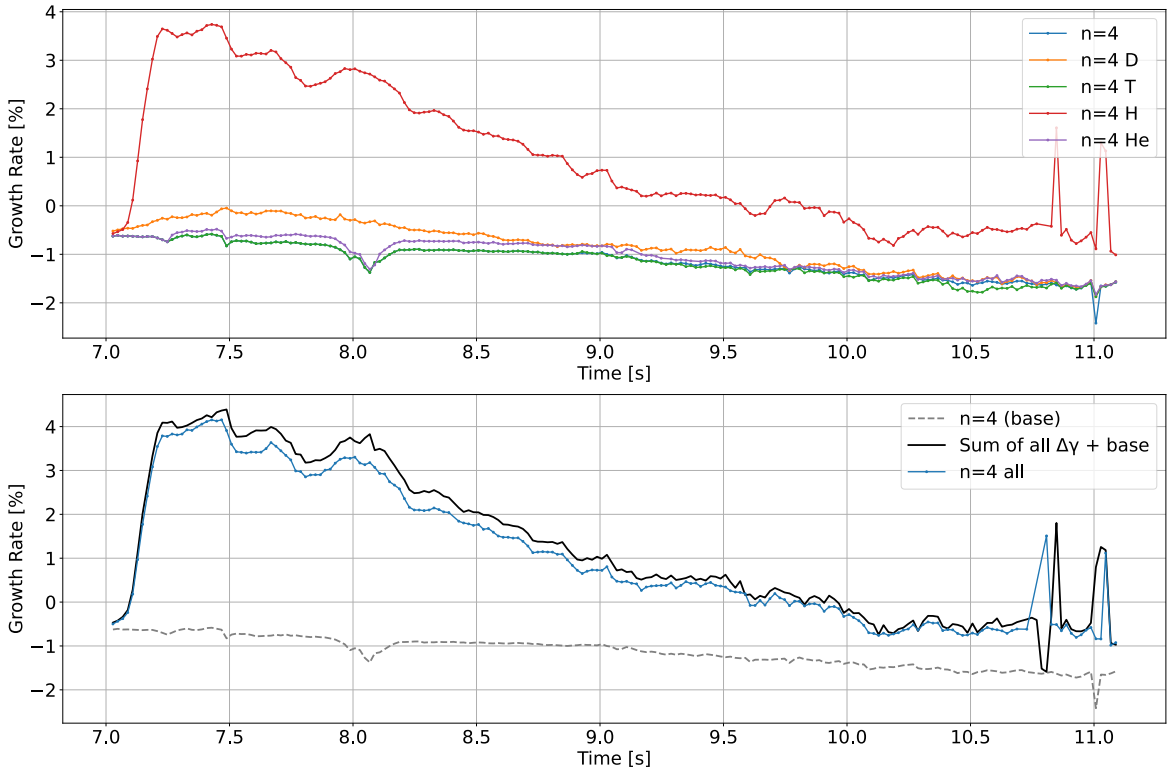

Figure 5.40: Time evolution of $(n, m) = (4, 4)$ odd mode growth rate (top) for each fast species present in the plasma showing the contribution of each species to the mode growth rate: blue line is without EPs (base), and the rest denote each species. The bottom plot shows the mode growth rate with all species present (blue) and the sum of all the contributions (black) added to the base (grey dotted line). Spikes in the growth rate are explained in the text.

Looking at the $(n, m) = (4, 4)$ odd mode, the results are shown in Figure 5.39 and 5.40. As anticipated, the mode frequency is higher than that of the even mode, while both TAEs are located at the same radial position. A distinctive feature of the frequency behavior is that the shift observed in the even mode also occurs here, but in reverse order. Initially, the mode frequency is higher with EPs compared to the no-EP case, but later it drops below it. This behavior is expected, as fast particles provide stronger drive

before $t = 9$s, but as the mode shifts radially outward, the drive weakens. Unlike the even mode, where the continuum frequency was lower than the mode frequency, causing EPs to push the mode downward, here, the opposite occurs because the continuum frequency is higher than the mode frequency itself (see Fig. 5.22)

A peculiarity of the frequency is the unexpected drops in frequency at 11.028s. This is due to the automatic solver detecting a different mode, not belonging to the same mode branch, i.e. the even mode. This is visible by comparing the mode structures of the expected and detected modes in Figure 5.41 and 5.42. The first one at 10.987s is the expected mode structure specific to odd TAEs. The second one at 11.028s is the even mode detected by the solver and at a different radial location compared to the expected odd mode. This is an effect of the automatic settings of the solver, and not a physical effect. A reasonable balance for 300 time points, with two outliers being acceptable for now, though improvements are planned for the future.

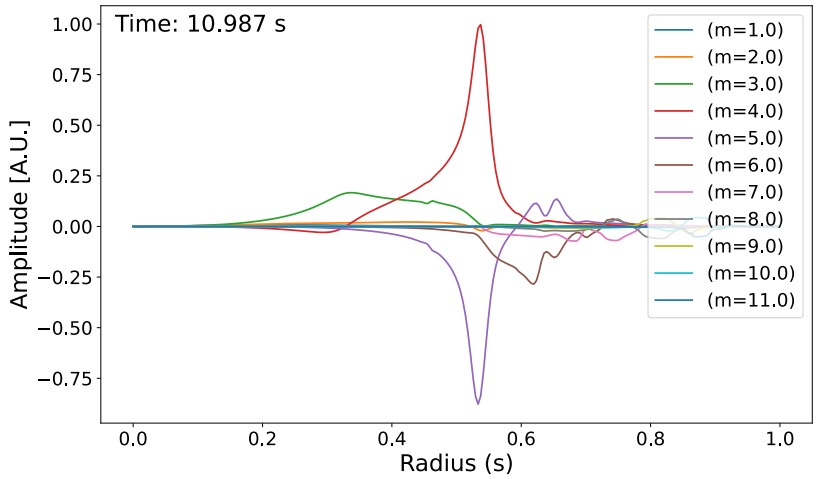

Figure 5.41: Expected mode structure of $(n, m) = (4, 4)$ odd mode at $t = 10.987$s. Different harmonics are depicted in different colors.

Regarding the growth rate, the mode remains unstable during the initial phase of the discharge (up to 9.6s), driven solely by the fast Hydrogen ions. Overall, its growth rate is lower than that of the even mode. The observed drops in growth rate are attributed to the same issue discussed earlier.

For the $(n, m) = (5, 5)$ odd mode, the results are shown in Figure 5.43 and 5.44. All the same analysis as before applies for this mode. This includes, the higher frequency of the mode, the frequency shift happening later but in the same way as explained for $n = 4$ case, and the drive coming only from the Hydrogen fast ions, rendering the mode unstable (in the first part of the discharge (until 10s due to the closer position to the core than the $n = 4$ mode))

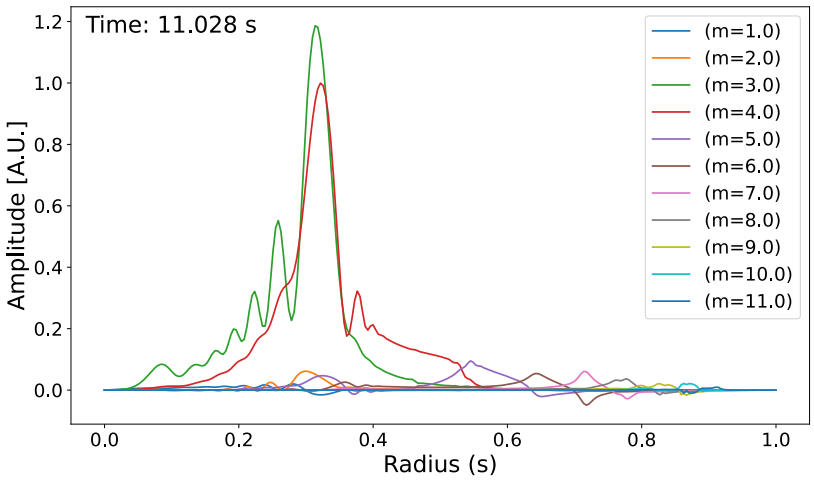

Figure 5.42: Detected mode structure of $(n, m) = (4, 4)$ odd mode at $t = 11.028$s where the sudden drop in frequency can be seen. Different harmonics are depicted in different colors.

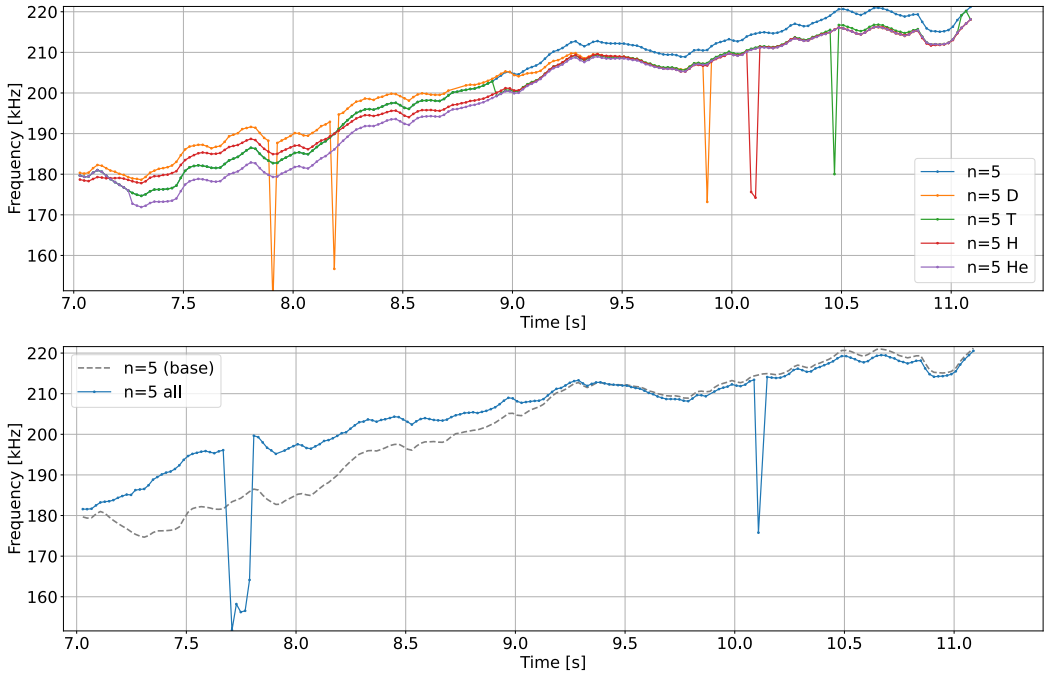

Figure 5.43: Time evolution of $(n, m) = (5, 5)$ odd mode frequency (top) for each fast species present in the plasma showing the contribution of each species to the mode frequency: blue line is without EPs (base), and the rest denote each species. The bottom plot shows the mode frequency with all species present (blue) and the base (grey dotted line) with no EPs present.

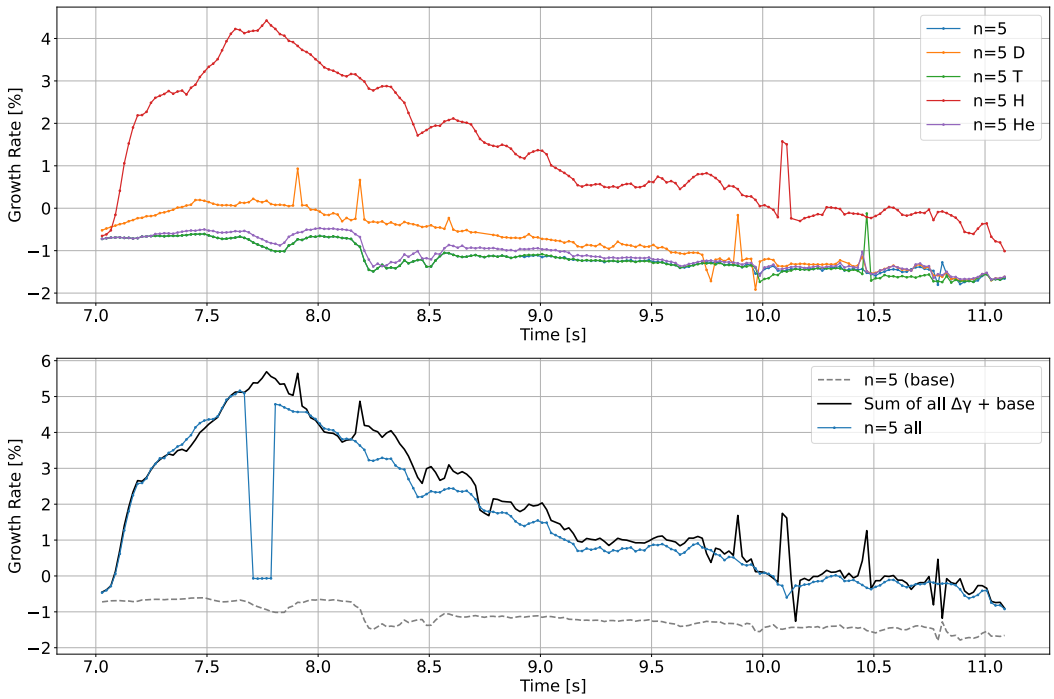

Figure 5.44: Time evolution of $(n, m) = (5, 5)$ odd mode growth rate (top) for each fast species present in the plasma showing the contribution of each species to the mode growth rate: blue line is without EPs (base), and the rest denote each species. The bottom plot shows the mode growth rate with all species present (blue) and the sum of all the contributions (black) added to the base (grey dotted line).

During the discharge we notice that when all EPs are present, there is a sudden drop in growth rate to ≈ 0 at $t = 7.7 - 7.8$s. This, contrary to before it is not due to the detection of another mode, but rather due to the solver being unable to properly resolve the mode structure at that time step. This is an effect of the automatic settings of the solver (that detects a mode of the EPM continuum and can be avoided by shifting the integration contour further in the complex plane), and not a physical effect. This too is avoidable by continuously tuning the solver methods/settings. A non converged mode structure is visible in Figure 5.45. Also in this case, refined numerical settings will be able to resolve this error.

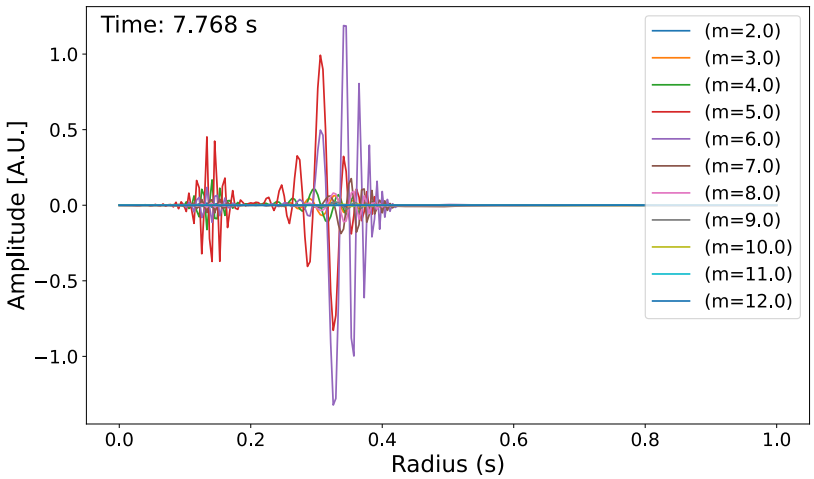

Figure 5.45: Non converged mode structure of $(n, m) = (5, 5)$ odd mode at $t = 7.768$s where the sudden drop in growth rate to 0 can be seen. Different harmonics are depicted in different colors.

5.5 Comparison with experiment and future work

In order to validate the workflow results, a comparison with the experimental data is carried out in this chapter. The experimental data consists of magnetic measurements from Mirnov coils, which detect the magnetic perturbations caused by the TAE modes. The frequency of these modes can be seen in Figure 5.18.

In a tokamak the plasma is not stationary, it rotates (mainly toroidally with smaller poloidal component). The intrinsic eigenfrequency of a mode is calculated in the plasma's rest frame. However, diagnostics measure the frequency in the lab frame. Because of the plasma rotation, the mode's frequency is Doppler-shifted by an amount proportional to the rotation frequency (typically, an addition of $n\Omega_\varphi$ for a mode with toroidal mode number n). In other words, one needs to apply (or subtract) the rotation frequency to convert between the plasma frame and the lab frame. This correction is essential not only for matching theoretical predictions to experimental data but also because the rotation can affect the stability and damping properties of the mode through modifications of the wave-particle resonance conditions. A rotation of 5 kHz is applied to the workflow results (priv. communication R. Coelho, JET team). The results are shown in Figure 5.46. In the figure the even modes are shown in green, blue and purple for $(n, m) = (4, 4), (6, 6), (5, 5)$ respectively, both before and after the rotation has been applied.

When comparing the experimental data with the workflow results, several key observations can be made:

- The frequency range of the detected modes (140-170 kHz) matches well with the computed TAE frequencies for n=4,5,6
- The frequency evolution trend throughout the discharge is correctly captured, including:
  - The initial frequency peaks in the early phase (7.5s, 8s)
  - The relatively constant frequency during the main heating phase (8-9s)
  - The gradual increase in frequency in the later phase (>9s)
- The sudden frequency shifts observed during sawtooth crashes (e.g. at $7.9 - 8.3$s) are reproduced by the simulations

However, some discrepancies between simulation and experiment are noted with the absolute frequency values showing deviations of $5 - 10$ kHz in certain phases.

These differences can be attributed to several factors that motivate future improvements:

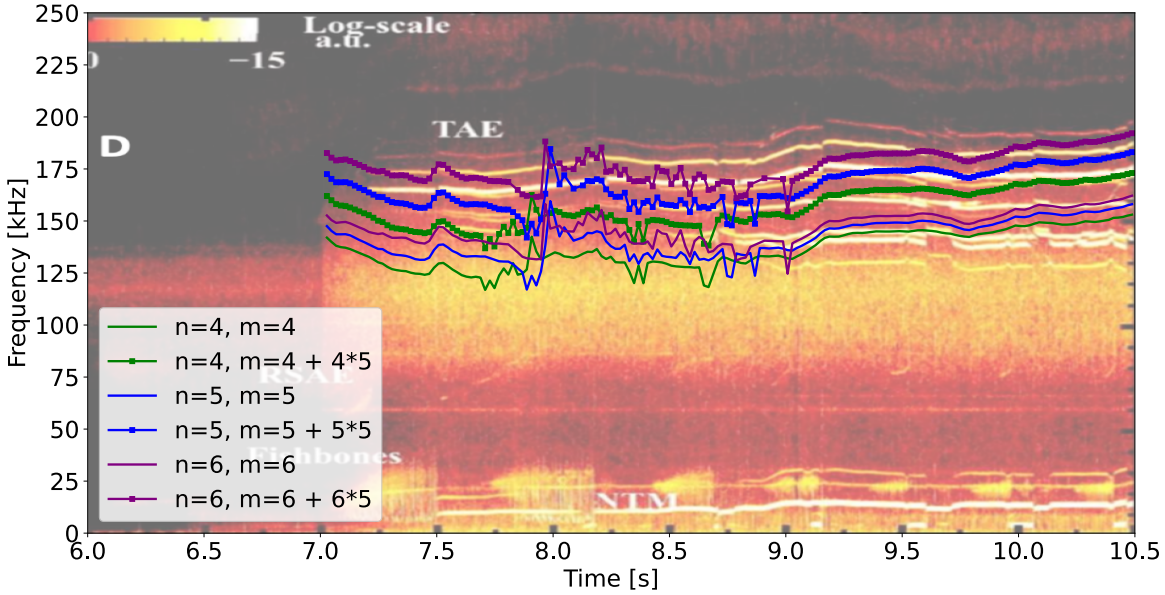

Figure 5.46: Adapted from Figure 1 [61].Time evolution of different modes in JET as detected by the experiment. Overplotted is the frequency of the modes computed by the workflow. $(n, m) = (4, 4), (6, 6), (5, 5)$ even modesare shown green, blue and purple respectively. A rotation of 5 kHz is applied to the workflow results.

1. Uncertainties in the equilibrium reconstruction, the q-profile evolution particularly, around the $q = 1$ surface, introduces uncertainties in the mode locations

2. The use of equivalent Maxwellian distributions for the fast particles, rather than realistic NBI distributions

3. Simplified treatment of the mode-particle resonances with FOW being included in LIGKA, using analytical fast circulating approximation; whereas in JET the drive is mainly due to trapped ICRH accelerated ions

4. Lack of non-linear saturation mechanisms in the current linear analysis

Future work will address these limitations through:

- Improved equilibrium reconstruction techniques using MHD marker information throughout the entire dataset

- Using numerical calculation of kinetic resonance integrals, rather than analytical approximations in fast circulating limit, especially because most relevant EPs are trapped particles (ICRF).

- Using realistic fast particle distributions
- Once these improvements are carried out, the remaining differences may be attributed to effects not captured by the workflow, such as non-linear effects. This information is very valuable, because then time slices where these effects are most pronounced can be chosen for non-linear analyses (ORB5 [75], MEGA [76], GENE [77], FAR3D [17]). Integration with ATEP (quasi-linear analysis) with more realistic fast particle distributions will be carried out.

Despite these limitations, the workflow demonstrates its capability to capture the main features of the experimental observations and provides valuable insights into the underlying physics of TAE modes in JET DT plasmas. Several steps have already been taken to pave the road towards the improvements discussed above. Future iterations with the JET team to improve the underlying interpretative transport run will very likely lead to a quite satisfying match throughout the whole discharge.

In the fast WF version of LIGKA, a passing-particles approximation is used to compute the kinetic response and the finite orbit width (FOW) effects. This approximation is generally appropriate for background particles and for beam-driven modes in cases such as AUG and ITER, where the response is dominated by passing particles. However, in the JET DT scenario the drive is primarily provided by trapped hydrogen ions. Consequently, significant differences in the kinetic response are expected, and an accurate treatment of the distribution function becomes crucial. In this context, it is important to examine the sensitivity of FOW effects by scaling the parameter $k_\perp \rho_{EP}$ in the FOW terms. Figures 5.47 and 5.48 show the sensitivity of the mode frequency, damping rate and mode structure to the FOW parameter $k_\perp \rho_{EP}$ for the $(n, m) = (5, 5)$ even mode at $t = 7.98$s. Results reveal a high sensitivity to FOW effects. Small changes in the parameter $k_\perp \rho_{EP}$ lead to significant variations in the linear mode properties. In particular, when the drive is provided by trapped hydrogen ions (as in the JET DT case), their influence becomes dominant, affecting both the growth rates and the real frequencies of the modes. The real frequency behavior shows a characteristic trend, initially decreasing (downshift) and then increasing (upshift) which is consistent with the ITPA FOW scan results and theoretical predictions [78]. In the case of even modes one expects lower growth rates, and thus the mode is expected to be less unstable. That means that the large growth rates challenging the numerical settings of the solver (see section above, around 8s) are expected to disappear. The drop in growth rate would mean that the odd modes would become stable in the case of JET DT experiment leading to an agreement with the experimental observations (no odd modes visible in the magnetic spectrum).

In addition, as demonstrated in [79], trapped electrons in regions with flat magnetic shear can contribute to the damping of kinetic Alfvén waves (KAWs). Trapped particles

are presently not included in the workflow. Incorporating these effects is expected to modify the linear damping slightly, typically of the order of 0.5%.

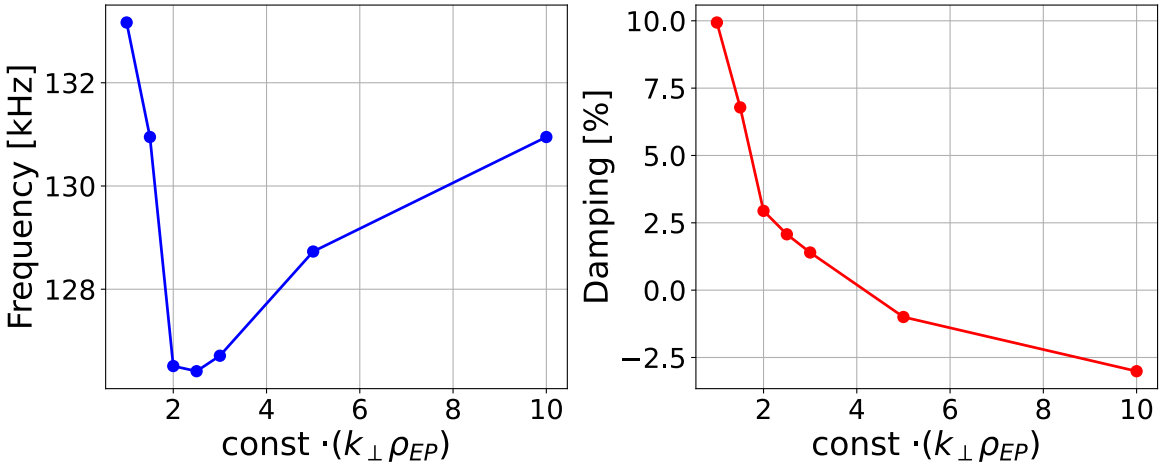

Figure 5.47: At $t = 7.98$s. Left: Sensitivity of the mode frequency to the FOW parameter $k_{\perp}\rho_{EP}$ for the $(n, m) = (5, 5)$ even mode. Right: Sensitivity of the mode damping rate to the FOW parameter $k_{\perp}\rho_{EP}$ for the $(n, m) = (5, 5)$ even mode.

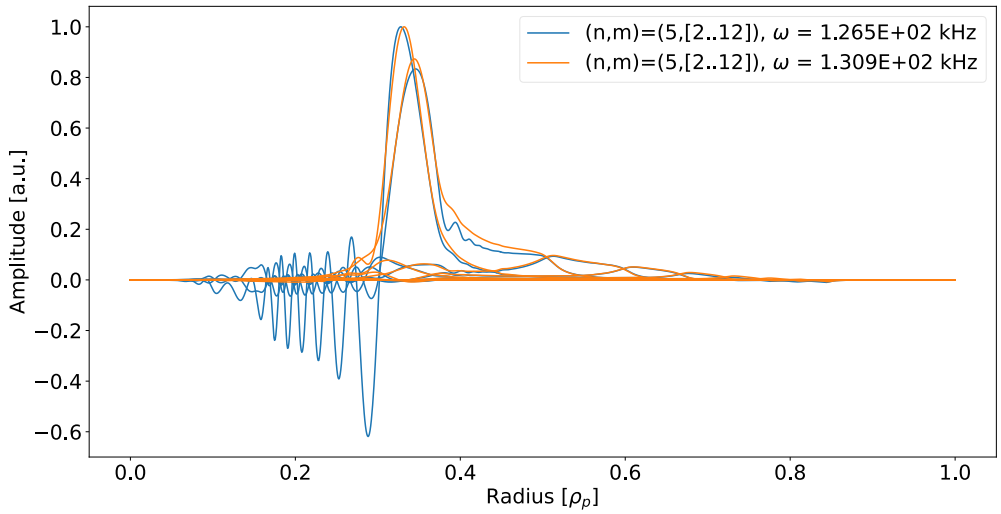

Figure 5.48: At $t = 7.98$s. Blue: Mode structure of the $(n, m) = (5, 5)$ even mode by increasing the effecitve FOW parameter by factor of $const = 1.4$. Orange: Mode structure of the $(n, m) = (5, 5)$ even mode by increasing the effecitve FOW parameter by factor of $const = 3$.

5.6 Integration with ATEP

Linear results are quite encouraging compared to the experiments, thus, quasi-linear models are expected to give meaningful results concerning the EP transport. The Advanced Transport Model for Energetic Particles (ATEP) provides a sophisticated phase-space resolved approach to modeling energetic particle (EP) transport, grounded in first-principles gyrokinetic theory. Unlike traditional diffusion-based models, ATEP evolves EP fluxes self-consistently in the constants-of-motion (CoM) space, making it particularly suited for capturing meso-scale EP dynamics. It computes phase-space fluxes using wave-EP interaction models and orbit-averaged transport coefficients. Using HAGIS, it integrates gyrokinetic response functions to capture EP redistribution from resonant interactions, providing a detailed view of EP evolution in energy and pitch-angle space beyond simple radial diffusion models. It models the evolution of Phase-Space Zonal Structures (PSZS), which emerge from EP self-organization via wave-particle interactions. The PSZS evolution follows an advection-diffusion equation, incorporating nonlinear mode saturation and zonal flows to predict how resonant and non-resonant mechanisms influence EP confinement over time.

The results of the workflow were directly connected to calculate the EP transport: Mode structures and linear growth rates were used to calculate the EP fluxes in phase space, using the HAGIS code (see chapter 3). In figures 5.49 and 5.50 the EP fluxes (dP_z/dt) for $n = 4 + 5$ modes for 660 keV Hydrogen ions and 80 keV beam Deuterium ions are shown. The fluxes are calculated at $t = 8.508$s. On the figures marked are the different states that ions are in, mainly trapped, counter-passing and co-passing.

One can see that regions of outward (blue) and inward (red) transport exist, more or less mapping resonance lines in CoM space. It can be seen that the structure can be very different for circulating and trapped particles, due to their very large orbit width in JET. For modelling the related EP transport, the detailed distribution functions would be needed, which, however, were not yet provided by the JET team.

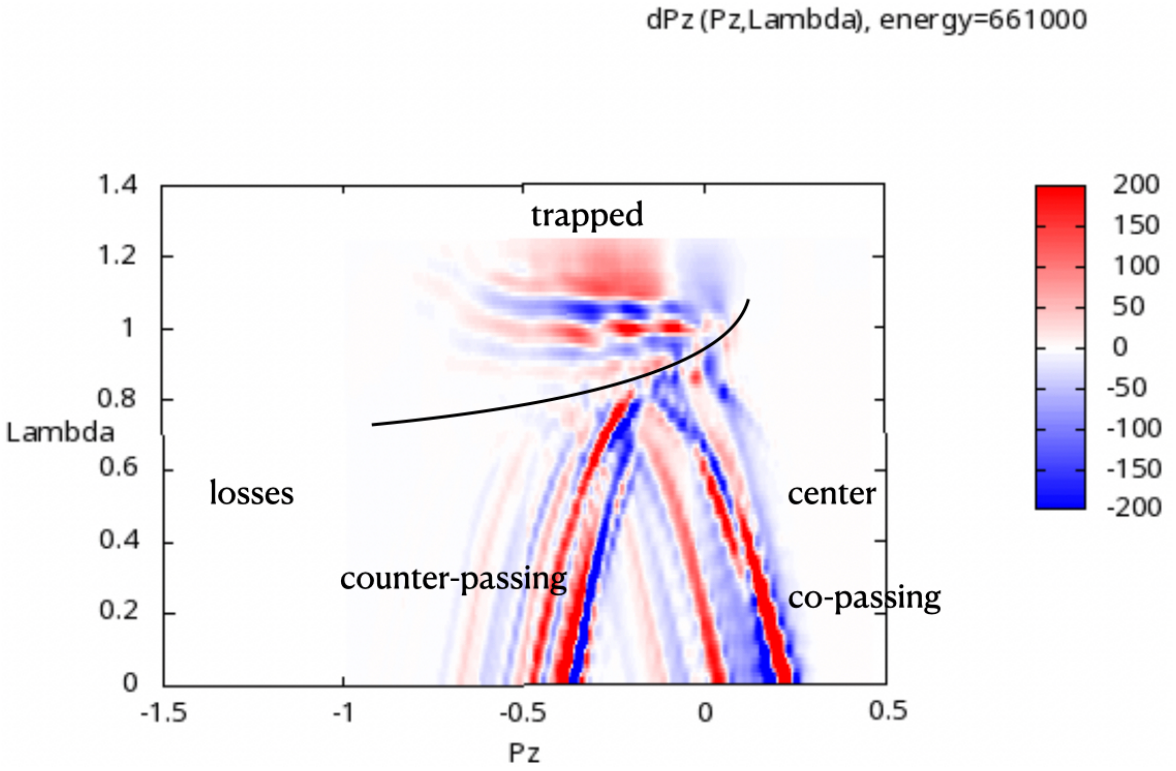

Figure 5.49: At $t = 8.508$s. Calculation of EP fluxes (dP_z/dt) for $n = 4 + 5$ modes for 660 keV Hydrogen ions.

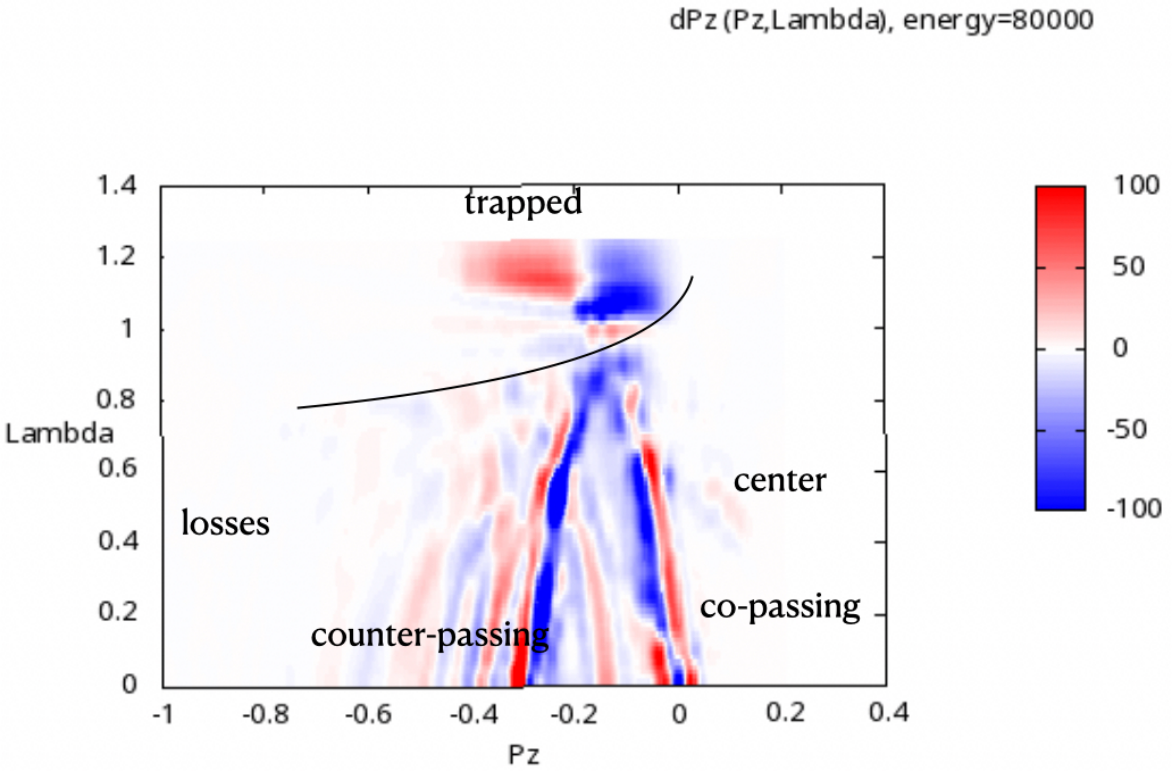

Figure 5.50: At $t = 8.508$s. Calculation of EP fluxe (dP_z/dt) for $n = 4 + 5$ modes for 80 keV beam Deuterium ions.

5.7 Reproducibility of the results

The codes used to generate the results in this paper are controlled via a release process. The codes are also available as modules on the ITER Linux cluster ("SDCC").

In this thesis, the following versions of the codes were used, with the Data Dictionary (DD) version 3.42.0 and Access Layer (AL) version 5.3.0:

1. HELENA: 2.1.0
2. LIGKA: 2.1.0
3. CHEASE: 14.4.1
4. EP-WF: 2.0.0

As an overview, in the table below, detailed information about the computational resources and runtimes of the test cases discussed in this thesis is presented. Note that these run times can be significantly reduced by parallelizing over multiple time slices simultaneously, rather than processing them sequentially (workflow has capability to launch multiple instances of itself in parallel).

Case	Run Scope	Timeslices	Modes	Procs	Total Time	Time/Time-slice	Time/Mode
ASTRA	local + global scan	1	175	local = 1, global = 8	09:18:06	09:18:06	00:04:00
ASTRA	local - continuum	1	3	1	00:25:04	00:25:24	00:08:33
METIS	local scan	106	12014	1	01:00:24	00:00:34	<1s
METIS	local + global (-4/+16)	106	1	local = 1, global = 8	04:36:41	00:02:36	-
METIS	local + global (-4/+20)	106	1	local = 1, global = 8	06:20:02	00:03:35	-
METIS	local + global (-4/+28)	106	1	local = 1, global = 8	10:31:06	00:05:56	-
METIS	local + global (-4/+32)	106	1	local = 1, global = 8	13:00:35	00:07:23	-
JET	local scan	294	>32000	1	00:59:40	00:00:12	<1s
JET	continuum MHD	156	1	1	00:58:30	00:00:25	-
JET	continuum kinetic	156	1	8	1-02:32:44	00:10:12	-
JET	local + global	156	1	8	10:46:13	00:04:8	-

Table 5.1: Run times for different cases presented in this thesis. The computational resources are also shown in terms of processes being used for each run. The total run time for the equilibrium code at each timeslice is also included.

6 Conclusions

This thesis set out to develop an automated, time-dependent workflow within the IMAS framework that integrates advanced equilibrium solvers, gyrokinetic stability codes, and energetic particle transport models to address the challenge of predicting Alfvén Eigenmode (AE) behavior in fusion plasmas. Several challenges had to be overcome in order to achieve this: combining different code standards, evolving standards for IDSs and code wrappers (FC2K, iwrap), new data standard that was not available for most experiments, similarly for the transport codes. Through the innovative coupling of tools such as CHEASE, HELENA, LIGKA, and the fast-particle transport module ATEP, this study has not only enhanced our understanding of AE stability in various phases on future fusion devices, but also provided a robust platform for reconciling simulation results with experimental observations.

It is known that the growth and damping rates of AEs are exponentially sensitive to the profiles. The EP-Stability workflow for the first time can address this difficulty by analysing sets of time slices using consistent equilibria and profiles. This gives us a consistent and reliable uncertainty quantification. Interpretative modelling can be improved by including the results of the WF analysis and thus allow us to separate linear and non-linear effects. The detailed analysis of scenarios based on ASTRA, DINA-JINTRAC, METIS, and JET DT experimental data shows that the automated EP-Stability workflow is capable of capturing the complex dynamics of energetic particle interactions. This capability is crucial for predicting performance in future devices such as ITER and DEMO, where ensuring the proper confinement of energetic particles is paramount for achieving sustained fusion.

Beyond its new physics insights and technical accomplishments, this work has also made a strong contribution to the methodological framework of fusion research. By adhering to FAIR data practices, the workflow ensures that simulation results are not only reproducible but also interoperable with other tools and experimental databases. This structured approach enables collaborative research and paves the way for future developments where more sophisticated models including non-linear effects (ATEP), detailed orbit dynamics, and the analysis of additional eigenmodes like RSAEs and BAEs, can be seamlessly integrated. This has been done to some extent, not reported here (AUG, JT-60SA, VNS).

The challenges encountered during this work, such as balancing computational

cost with model fidelity and managing the inherent complexity of the gyrokinetic equations,highlight areas for further improvement. Future research may benefit from incorporating advanced numerical techniques, extending the models by integrating more accurate analytical models for trapped particle effects, analytical and ML models for speeding up the more expensive global calculations. These extensions could further refine the predictive capabilities of the workflow and contribute to the optimization of plasma performance and reactor safety. Concrete steps to integrate the workflow in transport codes (JINTRAC, ETS, ASTRA) have been already taken.

In summary, this thesis significantly advances the previous state-of-the-art methods in modeling energetic particle stability in fusion plasmas. It provides a powerful, automated analysis tool that bridges theory and experiment, offering valuable insights into the control of TAE-driven instabilities. By improving our predictive understanding of energetic particle transport, this work contributes to the overarching goal of achieving sustainable fusion energy and underscores the potential for future innovations in integrated plasma modeling.

Bibliography

[1] K. Tomabechi et al. “ITER conceptual design”, *Nuclear Fusion* 31, 6 (1991), pp. 1135–1224.

[2] R. Hazeltine et al. *Plasma Confinement*. Dover books on physics. Dover Publications, 2003. ISBN: 9780486432427.

[3] J. D. Lawson. “Some Criteria for a Power Producing Thermonuclear Reactor”, *Proceedings of the Physical Society. Section B* 70, 1 (1957), pp. 6–10.

[4] F. F. Chen. *Introduction to Plasma Physics and Controlled Fusion*. Springer International Publishing Switzerland 2016. Springer International Publishing, 2016. ISBN: 978-3-319-22308-7.

[5] L. Chen et al. “Physics of Alfvén waves and energetic particles in burning plasmas”, *Reviews of Modern Physics* 88, (2016).

[6] S. Pinches. “Nonlinear interaction of fast particles with Alfvén waves in tokamaks”, (2020).

[7] A. B. Mıkhaılovskii. “Thermonuclear "drift" instabilities”, *Journal of Experimental and Theoretical Physics* 41, (1975), pp. 890–894.

[8] C. Z. Cheng et al. “Low-n shear Alfvén spectra in axisymmetric toroidal plasmas”, *The Physics of Fluids* 29, 11 (1986), pp. 3695–3701.

[9] P. Lauber et al. “LIGKA: A linear gyrokinetic code for the description of background kinetic and fast particle effects on the MHD stability in tokamaks”, *Journal of Computational Physics* 226, (2007), pp. 447–465.

[10] P. Lauber. “Super-thermal particles in hot plasmas—Kinetic models, numerical solution strategies, and comparison to tokamak experiments”, *Physics Reports* 533, 2 (2013), pp. 33–68.

[11] L. Chen et al. “Physics of Alfvén waves and energetic particles in burning plasmas”, *Rev. Mod. Phys.* 88, (2016), p. 015008.

[12] P. Lang et al. “Investigation of pellet-triggered MHD events in ASDEX Upgrade and JET”, *Nuclear Fusion* 48, 9 (2008), p. 095007.

[13] E. Lanti et al. “ORB5: a global electromagnetic gyrokinetic code using the PIC approach in toroidal geometry”, *Computer Physics Communications* 251, (2020).

[14] A. Mishchenko et al. “Pullback scheme implementation in ORB5”, *Computer Physics Communications* 238, (2019).

[15] Z. Lin et al. “Turbulent Transport Reduction by Zonal Flows: Massively Parallel Simulations”, *Science* 281, 5384 (1998), pp. 1835–1837.

[16] T. Görler et al. “The global version of the gyrokinetic turbulence code GENE”, *Journal of Computational Physics* 230, 18 (2011), pp. 7053–7071. ISSN: 0021-9991.

[17] D. A. Spong et al. “Nonlinear evolution of the toroidal Alfvén instability using a gyrofluid model*”, *Physics of Plasmas* 1, 5 (1994), pp. 1503–1510.

[18] A. Di Siena et al. “Global gyrokinetic simulations of ASDEX Upgrade up to the transport timescale with GENE–Tango”, *Nuclear Fusion* 62, 10 (2022), p. 106025.

[19] R. Waltz et al. “Development and validation of a critical gradient energetic particle driven Alfven eigenmode transport model for DIII-D tilted neutral beam experiments”, *Nuclear Fusion* 55, 12 (2015), p. 123012.

[20] M. Podestà et al. “Computation of Alfvèn eigenmode stability and saturation through a reduced fast ion transport model in the TRANSP tokamak transport code”, *Plasma Physics and Controlled Fusion* 59, 9 (2017), p. 095008.

[21] N. Gorelenkov et al. “Resonance broadened quasi-linear (RBQ) model for fast ion distribution relaxation due to Alfvénic eigenmodes”, *Nuclear Fusion* 58, 8 (2018), p. 082016.

[22] M. V. Falessi et al. “Transport theory of phase space zonal structures”, *Physics of Plasmas* 26, 2 (2019), p. 022305.

[23] F. Imbeaux et al. “Design and first applications of the ITER integrated modelling & analysis suite”, *Nuclear Fusion* 55, 12 (2015), p. 123006.

[24] G. Falchetto et al. “The European Integrated Tokamak Modelling (ITM) effort: achievements and first physics results”, *Nuclear Fusion* 54, 4 (2014), p. 043018.

[25] H. Lütjens et al. “The CHEASE code for toroidal MHD equilibria”, *Computer Physics Communications* 97, (1996). ISSN: 0010-4655.

[26] G. Huijsmans et al. “Isoparametric Bicubic Hermite Elements for Solution of the Grad-Shafranov Equation”, *International Journal of Modern Physics C - IJMPC* 2, (1991), pp. 371–376.

[27] P. Lauber et al. “LIGKA: A linear gyrokinetic code for the description of background kinetic and fast particle effects on the MHD stability in tokamaks”, *Journal of Computational Physics* 226, 1 (2007).

[28] V.-A. Popa. "Workflow-based energetic particle stability analysis of projected ITER plasmas." M.Sc. thesis. Technische Universität München, 2021.

[29] P. Lauber et al. "ATEP: an advanced transport model for energetic particles", *Nuclear Fusion* 64, 9 (2024), p. 096010.

[30] P. Strand et al. "A FAIR based approach to data sharing in Europe", *Plasma Physics and Controlled Fusion* 64, 10 (2022), p. 104001.

[31] G. Pereverzev et al. "ASTRA automated system for transport analysis in a tokamak", *Max-Planck IPP Report* 5, 98 (1991).

[32] J. Artaud et al. "Metis: a fast integrated tokamak modelling tool for scenario design", *Nuclear Fusion* 58, 10 (2018), p. 105001.

[33] M. Schneider et al. "Simulation of heating and current drive sources for scenarios of the ITER research plan", *Nuclear Fusion* 61, 12 (2021), p. 126058.

[34] R. Khayrutdinov et al. "Studies of Plasma Equilibrium and Transport in a Tokamak Fusion Device with the Inverse-Variable Technique", *Journal of Computational Physics* 109, 2 (1993), pp. 193–201. ISSN: 0021-9991.

[35] M. ROMANELLI et al. "JINTRAC: A System of Codes for Integrated Simulation of Tokamak Scenarios", *Plasma and Fusion Research* 9, (2014), pp. 3403023–3403023.

[36] M. Vallar et al. "Excitation of toroidal Alfvén eigenmodes with counter-current NBI in the TCV tokamak", *Nuclear Fusion* 63, 4 (2023), p. 046003.

[37] H. Järleblad. "Orbit-space sensitivity of fast-ion diagnostics." eng. 2022.

[38] L. D. Landau. "On the vibration of the electron plasma", *Journal of Physics (U.S.S.R.)* 10, 25 (1946).

[39] F. Doveil et al. "Experimental Observation of Nonlinear Synchronization due to a Single Wave", *Phys. Rev. Lett.* 94, (2005), p. 085003.

[40] W. W. Heidbrink. "Basic physics of Alfvén instabilities driven by energetic particles in toroidally confined plasmas", *Physics of Plasmas* 15, 5 (2008).

[41] A. A. Vlasov. "On Vibration Properties of Electron Gas", *Journal of Experimental and Theoretical Physics* 3, (1938), p. 291.

[42] A. Mishchenko et al. "Mitigation of the cancellation problem in the gyrokinetic particle-in-cell simulations of global electromagnetic modes", *Physics of Plasmas* 24, 8 (2017).

[43] A. Bierwage et al. "Gyrokinetic analysis of low-n shear Alfvén and ion sound wave spectra in a high-beta tokamak plasma", *Nuclear Fusion* 57, 11 (2017).

[44] F. Zonca et al. "Kinetic theory of low-frequency Alfvén modes in tokamaks", *Plasma Physics and Controlled Fusion* 38, 11 (1996).

[45] J. Citrin et al. "Overview of tokamak turbulence stabilization by fast ions", *Plasma Physics and Controlled Fusion* 65, 3 (2023), p. 033001.

[46] O. P. Fesenyuk et al. "Frequencies of the geodesic acoustic mode and Alfvén gap modes in high-q2β plasmas with non-circular cross section", *Physics of Plasmas* 20, 12 (2013), p. 122503. ISSN: 1070-664X.

[47] O. P. Fesenyuk et al. "Geodesic acoustic mode frequency and the structure of Alfvén continuum in toroidal plasmas with high q2β", *Plasma Physics and Controlled Fusion* 54, 8 (2012), p. 085014.

[48] J. Candy. "Electron Landau damping of toroidal Alfvén eigenmodes", *Plasma Physics and Controlled Fusion* 38, 6 (1996).

[49] P. Lauber et al. "Kinetic Alfvén eigenmodes at ASDEX Upgrade", *Plasma Physics and Controlled Fusion* 51, 12 (2009).

[50] F. Zonca et al. "Existence of discrete modes in an unstable shear Alfvén continuous spectrum", *Plasma Physics and Controlled Fusion* 40, 12 (1998).

[51] P. Lauber et al. "Analytical finite-Lamor-radius and finite-orbit-width model for the LIGKA code and its application to KGAM and shear Alfvén physics", *Journal of Physics: Conference Series* 1125, (2018).

[52] R. Fischer et al. "Bayesian modelling of fusion diagnostics", *Plasma Physics and Controlled Fusion* 45, 7 (2003), p. 1095.

[53] S. D. Pinches et al. "Energetic ions in ITER plasmas", *Physics of Plasmas* 22, 2 (2015).

[54] P. Amestoy et al. "Multifrontal parallel distributed symmetric and unsymmetric solvers", *Computer Methods in Applied Mechanics and Engineering* 184, 2 (2000), pp. 501–520. ISSN: 0045-7825.

[55] S. D. Pinches et al. "The HAGIS self-consistent nonlinear wave-particle interaction model", *Computer Physics Communications* 111, (1998).

[56] E. Poli et al. "Reduction of the Ion Drive and ρ_θ^* Scaling of the Neoclassical Tearing Mode", *Phys. Rev. Lett.* 88, (2002), p. 075001.

[57] A. Bergmann et al. "Guiding center particle simulation of wide-orbit neoclassical transport", *Physics of Plasmas* 8, 12 (2001), pp. 5192–5198. ISSN: 1070-664X.

[58] M. Brüdgam. "Nonlinear Effects of Energetic Particle Driven Modes in Tokamaks." eng. PhD thesis. München: Technische Universität München, 2010.

[59] G. Meng et al. "Energetic particles transport in constants of motion space due to collisions in tokamak plasmas", *Nuclear Fusion* 64, 9 (2024), p. 096009.

[60] M. V. Falessi et al. "On the polarization of shear Alfvén and acoustic continuous spectra in toroidal plasmas", *Journal of Plasma Physics* 86, 5 (2020), p. 845860501.

[61] J. Garcia et al. "Stable Deuterium-Tritium plasmas with improved confinement in the presence of energetic-ion instabilities", *Nature Communications* 15, 1 (2024), p. 7846.

[62] A. Polevoi et al. "ITER Confinement and Stability Modelling", *Journal of Plasma and Fusion Research Series* 5, (2002).

[63] W. A. Houlberg et al. "Bootstrap current and neoclassical transport in tokamaks of arbitrary collisionality and aspect ratio", *Physics of Plasmas* 4, 9 (1997), pp. 3230–3242. ISSN: 1070-664X.

[64] M. Erba et al. "Validation of a new mixed Bohm/gyro-Bohm model for electron and ion heat transport against the ITER, Tore Supra and START database discharges", *Nuclear Fusion* 38, 7 (1998), p. 1013.

[65] R. E. Waltz et al. "A gyro-Landau-fluid transport model", *Physics of Plasmas* 4, 7 (1997), pp. 2482–2496. ISSN: 1070-664X.

[66] F. Köchl et al. "Optimizing the ITER 15 MA DT Baseline Scenario by Exploiting a Self-Consistent Free-Boundary Core-Edge-SOL Workflow in IMAS", IAEA-CN–258 (2018), p. 381.

[67] J. Garcia et al. "Stable Deuterium-Tritium plasmas with improved confinement in the presence of energetic-ion instabilities", *Nature Communications* 15, 1 (2024), p. 7846.

[68] M. Schneller et al. "Nonlinear energetic particle transport in the presence of multiple Alfvénic waves in ITER", *Plasma Physics and Controlled Fusion* 58, 1 (2016).

[69] T. Hayward-Schneider et al. "Global linear and nonlinear gyrokinetic modelling of Alfvén eigenmodes in ITER", *Nuclear Fusion* 61, (2021), p. 036045.

[70] EUROfusion. *European Researchers Achieve Fusion Energy Record.* https://euro-fusion.org/eurofusion-news/european-researchers-achieve-fusion-energy-record/. Press release. Accessed: 2025-02-21. 2022.

[71] G. Y. Fu et al. "Theory of a high-n toroidicity-induced shear Alfvén eigenmode in tokamaks", *Physics of Fluids B: Plasma Physics* 2, 5 (1990), pp. 985–993. ISSN: 0899-8221.

[72] G. Y. Fu. "Existence of core localized toroidicity-induced Alfvén eigenmode", *Physics of Plasmas* 2, 4 (1995).

[73] Y. Nishimura. "Excitation of low-n toroidicity induced Alfvén eigenmodes by energetic particles in global gyrokinetic tokamak plasmas", *Physics of Plasmas* 16, 3 (2009), p. 030702. ISSN: 1070-664X.

[74] S. Sharapov et al. "Stability of alpha particle driven Alfvén eigenmodes in high performance JET DT plasmas", *Nuclear Fusion* 39, 3 (1999).

[75] S. Jolliet et al. "A global collisionless PIC code in magnetic coordinates", *Computer Physics Communications* 177, 5 (2007).

[76] Y. Todo et al. "Magnetohydrodynamic Vlasov simulation of the toroidal Alfvén eigenmode", *Physics of Plasmas* 2, 7 (1995).

[77] F. Jenko et al. "Electron temperature gradient driven turbulence", *Physics of Plasmas* 7, 5 (2000), pp. 1904–1910. ISSN: 1070-664X.

[78] A. Könies et al. "Benchmark of gyrokinetic, kinetic MHD and gyrofluid codes for the linear calculation of fast particle driven TAE dynamics", *Nuclear Fusion* 58, 12 (2018).

[79] P. Lauber et al. "Kinetic Alfvén Waves in Tokamak Plasmas," *Proceedings of the 5th Asia-Pacific Conference on Plasma Physics (AAPPS-DPP 2021)*. Presented at the 5th Asia-Pacific Conference on Plasma Physics, 26 Sept–1 Oct 2021. Remote e-conference, 2021.

Acknowledgments

I would like to express my sincere gratitude to everyone who supported me throughout my PhD journey.

First and foremost, I extend my deepest thanks to my advisor, Priv.-Doz. Dr. Ph. Lauber, whose guidance, insight, unwavering support, and patience were invaluable from the beginning of my Master studies to the completion of this research. His mentorship has not only enriched my academic growth but has also inspired me to pursue excellence in all aspects of my work.

I would also like to acknowledge my colleagues and friends in the EP group of Max Planck Institute for Plasma Physics for creating a collaborative and stimulating environment. Special thanks go to Dr. Thomas Hayward-Schneider for his insightful discussions, technical assistance and permanent support throughout my doctorate.

I am profoundly grateful to my mother and my sister. Their patience, understanding, and constant encouragement have been a source of strength throughout this challenging journey.

Last but not least, I would like to thank my father, who has been my role model and my inspiration throughout my life.

Thank you all for making this achievement possible.